Trinity College Dublin
Coláiste na Tríonóide, Baile Átha Cliath
The University of Dublin

PhD Thesis

On the Design and Analysis of Indoor Millimetre-Wave Cellular Networks under Human Body Blockage

Author:
Fadhil Firyaguna

Supervisors:
Prof. Nicola Marchetti
Dr. Jacek Kibiłda

24th August 2020

Declaration

I declare that this thesis has not been submitted as an exercise for a degree at this or any other university and is entirely my own work.

I agree to deposit this thesis in the University's open access institutional repository or allow the Library to do so on my behalf, subject to Irish Copyright Legislation and Trinity College Library conditions of use and acknowledgement.

I consent to the examiner retaining a copy of the thesis beyond the examining period, should they so wish (EU GDPR May 2018).

Signed:

Fadhil Firyaguna, 24th August 2020

Summary

The wide spectrum available in the millimetre-wave band is key to provide enhanced capacity for the demands of the fifth-generation (5G) of cellular networks. However, the usage of millimetre-wave frequencies introduces a series of challenges to the system design and performance. The millimetre-wave signal does not propagate well from outdoor to indoor environments. Thus independent deployments are required to provide coverage in indoor venues, making indoor deployments an important use case for 5G networks. Moreover, the millimetre-wave propagation is easily obstructed by human bodies, which are ubiquitous in the mobile broadband environment and therefore impose a significant problem for 5G networks. Therefore, the goal of this thesis is to study the impact of human blockage on the design and performance of indoor millimetre-wave networks. We test system parameters such as deployment density, antenna beamwidth and transmission frame, aiming to find design solutions to effectively cope with adverse blockage effects on the millimetre-wave communication channel.

Firstly, we address the problem of human blockage in provisioning coverage in indoor networks. Our work focuses on solutions in the network deployment design to mitigate the blockage effects, using highly-dense ceiling-mounted access points with fixed directional antennas facing downward. Highly-dense network deployments may lead to excessive interference from neighbouring cells, causing deterioration of the system performance. However, the usage of this ceiling-mounted setup may reduce the interference by illuminating selected spots on the ground with the use of fixed directional antennas, confining the signal energy. The effectiveness of this approach on millimetre-wave networks is not clear in the literature as there is a lack of investigation on this type of setup when considering the blockage effects in the signal propagation. Thus, in our first research question, we study the impact of blockage on the performance and design of indoor millimetre-wave networks with access points installed on the ceiling. We develop a body blockage model and derive an analytical expression for the blockage probability, which allows us to evaluate the system for a set of body blockage scenarios. We also develop a simulation framework to test design parameters, such as the deployment density and the antenna beamwidth, to find the best configuration to cope with the human blockage problem. We find that there exists a set of optimal density-beamwidth configurations for each blockage scenario, and there exists a trade-off in this configuration, in which a certain configuration optimises either coverage or spectral efficiency, but not both. The optimal configuration takes different values depending

on the severity of the blockage scenario. Furthermore, we develop an analytical framework to evaluate the expected data rate and test the design of transmission frame parameters given by recent 5G standardisation such as the transmission time interval. We show that there is a trade-off between the probability of blockage and the transmission efficiency when choosing the best transmission time interval for different blockage scenarios. Therefore, the system design configuration should carefully consider the intended scenario since each scenario needs a different configuration in terms of deployment density, antenna beamwidth and transmission interval to achieve the best system performance.

Secondly, we address the problem of human blockage in the efficiency of transmission resource allocation. In this second research question, we investigate how resource allocation can help mitigate the blockage effects on transmission efficiency. Most of the existing efforts on resource allocation techniques aiming to mitigate blockage effects consist in handing-off the communication to another spatial resource (other cell or antenna beam direction). However, the hand-off procedure has an inherent re-connection latency and overhead that may degrade the efficiency of the blockage mitigation. Moreover, another cell or beam might not always be available, and thus other resource allocation techniques that do not depend on other spatial resources should be investigated. We focus our study on the resource allocation provided by scheduling algorithms. First, we analyse how conventional algorithms, such as the Proportional Fair scheduler, behave under blockage events. We show that such algorithms disfavour the allocation for users suffering from blockage, leading to poor data rate performance. Then, we show that to improve the performance of such users, the system needs a proactive scheduling approach aided by blockage prediction mechanisms. Hence, the scheduler can preemptively allocate the transmission resources before a blockage event and release them after that. We conclude that a resource allocation approach that allows for adaptive scheduling intervals can help mitigate blockage, and has to consider the specific blockage scenario and the predicted blockage event to be effective.

Acknowledgements

Firstly, I'd like to thank the Universe, with all complex particle interactions and random events, to finally emerge with this thesis today.

I'd like to thank my parents Firdawati Yannes and Yannes Achmad for raising me despite all difficulties, and my big brother Ikhsan Firyanusa for inspiring me to be creative, allowing me to become a person that is capable of achieving great things in life such as this thesis.

I'd like to thank Prof. Luiz DaSilva for introducing me to CONNECT Centre and for sharing immense knowledge about research, science, teaching, and board game strategies.

I'd like to thank Prof. Nicola Marchetti for the guidance through this journey, advising me with his knowledge and experience, and with his unfailing kindness and patience, which were crucial in many moments of both despair and joy.

I'd like to thank Jacek Kibiłda and Carlo Galiotto for the mentoring and their tremendous effort to help me to improve in many aspects of the research life.

I'd like to thank my student counsellor Sandra Carroll, my occupational therapist Kieran Lewis and my psychiatrist Caoimhe Clarke for their vital support through the difficult times.

I'd like to thank my senior PhD fellows Conor Sexton, Merim Dzaferagic, Parna Sabeti, Boris Galkin, Jernej Hribar, Jonathan van de Belt, Danny Finn, Elma Avdic, Francisco Paisana and Pedro Alvarez for their prompt help in many issues of college life when I was a poor fresh student that had recently arrived in an unknown country.

I'd like to thank Nima Afraz for being there in many moments of our PhD student life, with food, drinks, pain, fears, conquests, jokes, and much more.

I'd like to thank Andrea Bonfante and Ramy Amer for all the long and productive discussions we had about millimetre-wave networks.

Last but not least, I'd like to thank our little, but never-ending, Brazilian community in CONNECT, Marcelo Marotta, Alextian Liberato, Maicon Kist, Joao Santos, Erika Fonseca, Matias Shimuneck, Ana Trevisan, Andre Gomes, Natal Neto, Davi Brilhante and Diego Mafioleti, for alleviating the home-sickness.

Contents

List of Figures

List of Tables

1 Introduction

Introduction

The number of global mobile subscribers surpassed 5.2 billion at the beginning of 2020 and is forecasted to reach 5.8 billion in 2025 [3], leading to an enormous increase in demand for mobile wireless services. Future applications are expected to require increased network capacity, as the upcoming user devices are expected to have enhanced multimedia capabilities such as ultra-high-definition displays, and virtual and augmented reality interfaces. Furthermore, these applications are expected to provide satisfactory experience even in the presence of a large number of concurrent connections, for example, in transportation hubs, stadiums, or other venues that attract many people [4]. Provisioning for such diverse demands requires dramatic improvement in capacity compared to what is available today.

The Radiocommunication Sector of the International Telecommunications Union (ITU-R) envisions that this increased number of mobile subscribers will be served by the Enhanced Mobile Broadband (eMBB) as part of the fifth-generation (5G) of cellular networks [5]. The eMBB will provide mobile services over multigigabit/s rate links, enabled by the high-density deployment of networks that utilise the wide spectrum available in millimetre-wave (mmWave) frequencies in addition to the traditional microwave spectrum (sub-6 GHz). However, the usage of mmWave frequencies in cellular networks imposes a series of challenges to all system aspects, in particular, the system performance and fundamental architectures of both access point (AP) (or base station) as well as the user equipment (UE), as the nature of radio propagation between microwave and mmWave frequencies is different [6].

The propagating mmWave signals suffer from higher path attenuation and lower penetration through materials such as building walls compared to microwave signals. It means that mmWave signals transmitted from outdoor base stations will be confined to streets and other outdoor areas [7]. This creates a situation where an independent tier of mmWave APs should be deployed to ensure coverage to UEs in indoor areas, as we illustrate in Fig. 1.1. Yet, ensuring coverage (and/or data rate) for indoor areas becomes challenging due to human bodies, which may introduce as much as 40 dB of attenuation [8–10], enough to break the AP-UE communication link. Furthermore, blockage events in mmWave can be frequent and intermittent as the movement of human bodies in the network venue can be highly dynamic. The blockage intermittency may affect the utilisation of transmission resources (e.g., time, frequency, space). For instance, pre-allocated transmission can be interrupted by a blockage before being successfully received, and the allocation of the following trans-

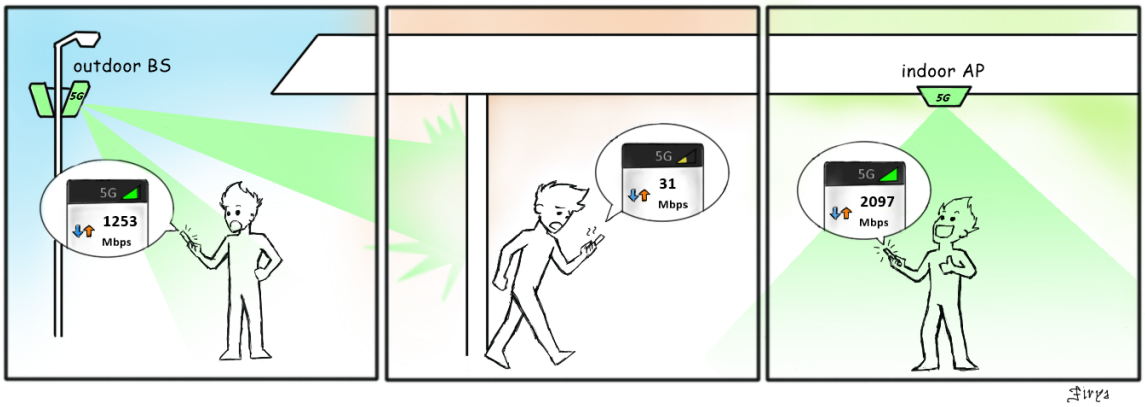

Figure 1.1: Independent tier of indoor mmWave ceiling-mounted AP deployment providing coverage with directional transmission pointing downward. The mmWave signal from outdoor base station (BS) does not propagate through building walls.

missions may be inefficient if the resource schedulers do not react quick enough to an abrupt disruption.

This research aims to characterise a network design which takes into account the above challenges related to potential mmWave signal blockages. We approach this problem by identifying and modelling the blockage effects on the network capacity, and managing the network resources to improve the capacity. We focus our analysis on the impact of blockage in a particular type of indoor deployment where the AP is mounted on the ceiling, as illustrated in Figure 1.1. This scenario is the proposed architecture of the NEMO (Enabling Cellular Networks to Exploit Millimetre-wave Opportunities) Project[1]. This project relies upon research and educational collaboration in the domain of wireless networking between the United States and Ireland, involving three institutions: Virginia Tech (VT), Trinity College Dublin (TCD) and Queen's University Belfast (QUB). The objective of the project is to develop and evaluate architecture concepts, network planning and deployment, resource allocation and sharing models, informed and enriched with dedicated channel measurements and experiments in networks operating in the mmWave bands. This PhD project is funded by NEMO and contributes to the project activities focusing on the capacity analysis of network deployments and the study of resource allocation.

1.1 Scope

In this PhD project, we focus on how mmWave networks can achieve satisfying performance, overcoming the channel unreliability caused by adverse mmWave propagation conditions in an indoor cellular network. Our approach lies on exploring proper ways to manage the resources in the network deployment (the number of APs deployed and beamwidth) and medium access control (MAC) layer (transmission duration and bandwidth) to cope with the unreliable channel. Hence, we want to answer these two main research questions:

[1]Science Foundation Ireland (SFI) grant No. 14/US/I3110

What is the effect of blockage on the performance and the design of indoor mmWave ceiling-mounted AP networks?

Regarding the deployment and beamwidth design, the state-of-the-art studies on capacity analysis of mmWave networks with blockage consider that the directional antenna is always pointing directly to the receiver [10–14], possibly creating significant interference on neighbouring links, especially in highly dense network deployments. Then, to answer this Research Question, we analyse the impact of network densification in an indoor deployment where APs are mounted on the ceiling with directional antennas facing downwards in Chapter 3, and we analyse the effects of different blockage scenarios on the capacity and deployment parameters design in Chapter 4.

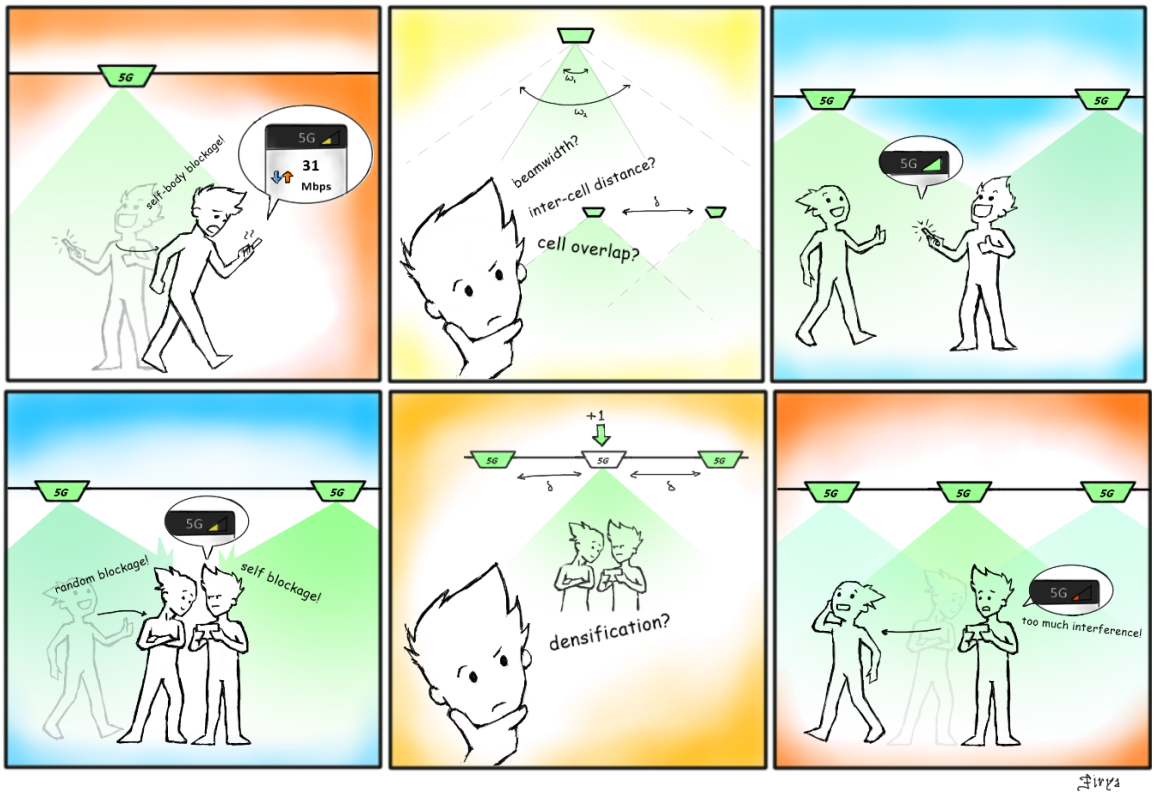

Figure 1.2: The effect of blockage in indoor mmWave ceiling-mounted AP networks.

How can resource allocation in MAC layer help mitigate the body blockage effects?

The literature on resource allocation techniques for mmWave cellular networks has not been addressing the blockage effects on the system performance, as it is focused on improving the network latency using flexible transmission schemes [15, 16]. On the other hand, the works studying the mitigation of blockage effects mainly exploit the spatial macro-diversity to circumvent the blockage (e.g. using reflections [17, 18], relays [19, 20], moving APs [21], or multi-connectivity [22, 23]). This leaves a gap in the research of blockage mitigation techniques which can be filled by studying the resource allocation at the MAC layer. Then, to answer the Research Question, we propose the application of flexible transmission intervals in Chapter 5 and in Chapter 6, we study a blockage-aware scheduling algorithm aided with prediction mechanisms to cope with dynamic blockages.

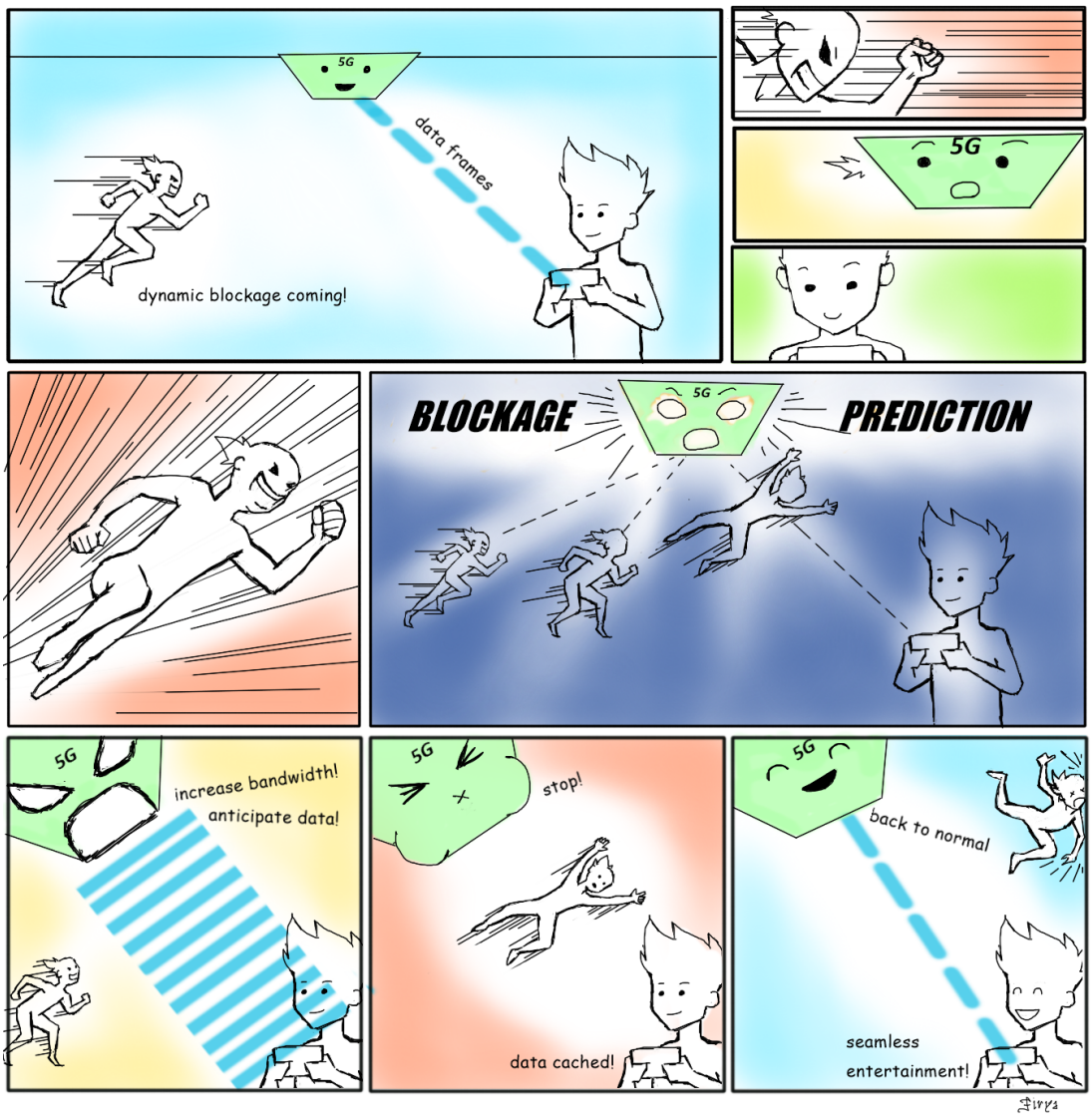

Figure 1.3: Resource allocation helping mitigate blockage effects.

1.2 Outline

In this thesis, we first provide background information on mmWave channel modelling, blockage modelling, mitigation and prediction, as well as the related work. Then, we present our technical contributions in four chapters. In each technical chapter, we motivate the specific problem, formulate the corresponding system model, discuss the results and highlight the lessons learnt. Finally, we provide a summary of the main take-away messages and discuss the implications of our research in terms of possible future works. The information in each chapter is summarised as follows:

Chapter 2 — Background

In the Background chapter, we briefly discuss the key technologies of 5G networks, and the characteristics of the mmWave spectrum and its implications on the system. Then, we review the literature on mmWave channel, blockage modelling, blockage mitigation techniques and blockage prediction methods.

Chapter 3 — Capacity Analysis of Indoor mmWave Networks

In Chapter 3, we study dense deployments of mmWave access points mounted on the ceiling, and illuminating selected spots on the ground. Our study is based on numerical evaluations of the resulting signal-to-interference-plus-noise ratio (SINR) of a link under self-body blockage. We evaluate our system taking into account the design of antenna beamwidth and access point density. Our results may serve as a set of recommendations for network designers on how to configure system parameters of an indoor deployment.

Chapter 4 — Performance Analysis of Indoor mmWave Networks under Human Blockage

In Chapter 4, we study the impact of human body blockage on the performance of the deployments introduced in Chapter 3. Our study includes the effect of the presence of multiple random bodies on the probability of blockage. We show that body blockage manifests itself in degraded link performance and affects the choice of operational network configuration. This network configuration will be closely tied to the probability of the body blockage, leading to a necessity for network designers to carefully consider their intended application and scenario.

Chapter 5 — Application of Flexible Numerology to Blockage Mitigation

In Chapter 5, we propose that the 5G new radio (NR) flexible numerology and slot aggregation be applied to mitigate adverse blockage effects. We validate our proposed solution by

analysing the expected data rate of a mmWave system, under a range of blockage scenarios. We show that different blockage scenarios may require different numerologies to produce the best performance. Our results carry relevant insights for the design of blockage-aware scheduling mechanisms for 5G.

Chapter 6 — Blockage-Aware and Preemptive Resource Allocation

In Chapter 6, we study the implications of dynamic blockage on resource scheduling algorithms. We analyse the performance of traditional schedulers, and we show that users transitioning from line-of-sight (LOS) to blocked state have inefficient allocation. Then, we discuss the necessity for a modification of these schedulers to consider blockage predictions into the resource assignment and preemptively allocate the resources before a blockage occurs.

Chapter 7 — Conclusions

In the last chapter, we summarise the answers we found to the thesis Research Questions, and we discuss the overall outcomes and significance of our research. Then, we suggest some topics for future work that can extend the work and results of this thesis. Finally, we discuss new research directions.

1.3 Contributions

In this section, we summarise the research contributions of the thesis.

Chapter 3

In this chapter, we focus on studying the capacity of the network in the indoor ceiling-mounted AP environment, assuming a self-body blockage scenario.

- We develop a simulation framework to study dense deployments of mmWave access points mounted on the ceiling, with directional antennas pointing downwards to illuminate selected spots on the ground.
- We analyse the impact of AP density and transmit/receive antenna beamwidths on the performance of an indoor mmWave cellular network, and we find operational beamwidth-density configurations that maximise system's capacity for ceiling-mounted deployments.

Chapter 4

In this chapter, we extend the analysis to multiple random bodies blockage scenarios, and we analyse the impact of those scenarios on the capacity of indoor ceiling-mounted AP networks, using our simulation framework.

- We develop a model of body blockage that describes the geometry of the ceiling-mounted AP deployment, and we derive an analytical expression for the probability of blockage.
- We find that the trade-off between coverage and area spectral efficiency is conditioned on the body blockage scenario. We show that the "trade" between coverage and area spectral efficiency can be more "expensive" in scenarios with higher blockage probability, e.g. the spectral efficiency shall be even more diminished in these scenarios to achieve a satisfactory level of coverage.
- We find that the beamwidth-density configuration for achieving peak coverage depends on the body blockage scenario. We show that large AP beamwidths can mitigate self-body blockage, high AP densities can benefit from the blockage of other bodies limiting interference, and the UE beamwidth needs to be adjusted to compensate for increased interference, shadowing or path loss in different AP densities.

Chapter 5

In this chapter, we focus on understanding the achievable capacity of a ceiling-mounted AP transmission when using the 5G NR flexible frame structure under human blockage.

- We are the first to study the application of the 5G NR flexible numerology and slot aggregation to mitigate the blockage effects. We analyse the expected data rate of a mmWave system using different configurations of numerology and slot aggregation under a range of blockage scenarios.
- We show that different blockage scenarios may require different numerologies to produce the best performance and that the correct choice of numerology and aggregation may improve this performance.

Chapter 6

In this chapter, we focus on the impact of blockage on scheduling algorithms. Building on top of state-of-the-art blockage prediction mechanisms, we analyse how preemptive resource allocation can be used to mitigate adverse blockage effects.

- We are the first to study the performance of schedulers under blockage scenario in mmWave networks, and we show that there are inefficiencies when using conventional schedulers.

- We show that the conventional Proportional Fair scheduler can improve the performance under blockage scenarios when modifications are made to the scheduler to take into account blockage predictions and estimated future user rates.

1.4 Dissemination

This section lists published and under-review papers written during the PhD project:

- F. Firyaguna, A. Bonfante, J. Kibilda, N. Marchetti, "Performance Evaluation of Scheduling in 5G-mmWave Networks under Human Blockage", submitted to IEEE Systems Journal, 2020.
- F. Firyaguna, J. Kibilda, C. Galiotto, N. Marchetti, "Performance Analysis of Indoor mmWave Networks with Ceiling-Mounted Access Points", published in *IEEE Transactions on Mobile Computing*, DOI: 10.1109/TMC.2020.2972282, Feb., 2020.
- F. Firyaguna, J. Kibilda, N. Marchetti, "Application of Flexible Numerology to Blockage Mitigation", published in *IEEE GLOBECOM 2019*, Hawaii, Dec., 2019.
- J. Kibilda, Y. J. Chun, F. Firyaguna, S. K. Yoo, L. A. DaSilva, S. L. Cotton, "Performance Evaluation of Millimeter-Wave Networks in the Context of Generalized Fading", published in *IEEE GLOBECOM 2018 workshop*, Abu Dhabi, Dec., 2018.
- F. Firyaguna, J. Kibilda, C. Galiotto, N. Marchetti, "Coverage and Spectral Efficiency of Indoor mmWave Networks with Ceiling-Mounted Access Points", published in *IEEE GLOBECOM 2017*, Singapore, Dec., 2017.

Presentations related to the research:

- "Application of Flexible Numerology to Blockage Mitigation", *IEEE GLOBECOM 2019 Mobile Wireless Networks Symposium, Interactive Session*, Hawaii, USA, December 2019.
- "Application of Flexible Numerology to Blockage Mitigation", poster in SATORI project workshop, Dublin, October 2019.
- "Performance Analysis of Indoor mmWave Networks with Ceiling-Mounted Access Points", poster in QUB Workshop: Research Advances in RF through mmWave Radio Communications Technologies, Belfast, UK, October 2018.
- "Coverage and Spectral Efficiency of Indoor mmWave Networks with Ceiling-Mounted APs", *IEEE GLOBECOM 2017 Mobile Wireless Networks Symposium, Millimeter-wave Session*, Singapore, December 2017.
- "Coverage and ASE of Indoor mmWave Networks with Ceiling-Mounted APs", *2nd NEMO Project Meeting*, Dublin, August 2017.

2 Background

Background

2.1 The Fifth-Generation of Mobile Wireless Networks

Every new generation of mobile wireless networks provides the user with faster than ever before data speeds, following the trend of increasing communication demands of the society. For the fifth generation (5G), one of the main targets is still to enhance the network capacity. However, the boost on the user data speed is not the only reason for that. There is also the need to accommodate an increasing number of users, devices and new applications. Indeed the 5G network should provide a foundation for emerging applications such as driverless vehicles, factory automation. In fact, the use cases for 5G networks are not just limited to mobile broadband. The envisioned applications can be categorised in three broad use cases [4]: enhanced mobile broadband (eMBB), ultra-reliable low-latency communication (URLLC) and massive machine type communications (mMTC), and each use case has its own performance requirements.

In this thesis, we study the network design focusing on applications in the eMBB use case, where Gigabit/s data rates on radio access are required. The eMBB use case encompasses the human user access to multi-media content and services. In 5G networks, the users will have their data speed enhanced by improvements on the network performance and user experience. This enhancement is a response to the improvement of multimedia definition/resolution (e.g., very high definition displays, immersive virtual/augmented reality) for entertainment, health, safety etc. Therefore, the system will need to support the increasing amount of data being generated and transmitted through the network. Furthermore, users shall expect a satisfactory end-user experience even in the presence of a large number of concurrent users (as in a transportation hub or in a sports arena), and when users are moving at high speed.

Provisioning such data rate enhancement for the envisioned eMBB will require significant improvements on the performance of many aspects of the network compared to previous network generations. There are three key technological approaches that, combined, allow for achieving Gigabit/s data rates in the radio interface.

- **Enhanced physical layer techniques:** The spectral efficiency can be enhanced by means of e.g., advanced waveforms, modulation and coding and advanced signal processing exploiting the use of multiple antennas. In this thesis, we focus on the use

of multiple antennas to provide directional communication, focusing the signal energy in a small space.

- **Network densification:** The capacity of the network can be increased by means of shrinking the cell area allowing for higher spatial reuse. In this thesis, we study the impact of densification on the performance of 5G networks.
- **Increased bandwidth on millimetre-wave spectrum:** The most important factor to improve data rate is allocating the escalating capacity demand on the huge bandwidths available in the millimetre-wave (mmWave) frequencies. Millimetre waves are considered to be the range of wavelengths from 1 to 10 mm. This corresponds to the frequency range from 30 to 300 GHz in the electromagnetic radio spectrum, which is also called the Extremely High Frequency (EHF) range.

In the following, we discuss in more depth the roles of network densification and the mmWave spectrum in the 5G network. The discussion of enhanced antennas is not the topic of this thesis and we consider a simple and tractable model for the antenna directivity, as it will be described in the technical chapters. Then, we provide a literature review of the main topics addressed in this thesis.

2.2 Network Densification

Network densification has been fundamental for increasing the capacity of conventional mobile networks, as spectrum designated for cellular communications in sub-6 GHz frequencies is relatively scarce. In the mmWave frequencies, where spectrum is in abundance, but adverse propagation conditions limit the signal penetration, network densification may be used to shorten the physical distance between the transmitters and receivers, ramping up the signal level at the receivers' input. Indeed, dense mmWave networks have been shown to be an attractive deployment option for outdoor urban areas [10, 24–26]. In [25] it has been shown that optimal operation of a wide-area mmWave system requires a deployment that is dense enough to ensure line-of-sight conditions from at least a few transmitters. The optimal deployment strategy results from the following trade-off: lower density deployments result in significantly lower performance due to non-line-of-sight (NLOS) operation, while higher density deployments lead to an increase in interference which deteriorates the system's performance.

Nevertheless, to ensure a targeted data rate, an even higher density might be required, and therefore, interference should be mitigated. In state-of-the-art literature, the interference mitigation can be achieved by inter-cell interference coordination (ICIC) techniques, which demand high signalling overhead [27]. One simpler way to reduce the interference is to restrict the signal propagation through the use of directional antennas mounted on the ceiling. Thus, the main-lobe of the directional antenna beam is pointed downwards to confine the signal's power to a limited space. Ceiling-mounted access point (AP) with fixed-beam antennas is also an option for quick and low-cost deployments as recommended

by ITU-R [28], facilitating AP densification in indoor environments. Dense ceiling-mounted deployments were first investigated in [29] for sub-6 GHz frequencies. In that work, Ho et al. have shown that the ceiling-mounted deployment with directional antennas was able to provide gains in throughput four times higher than the deployment with omnidirectional antennas. However, the link performance from a single ceiling-mounted mmWave transmitter can be degraded by human body blockage on the mmWave signal, as shown in [30–32].

2.3 The Millimetre-Wave Spectrum

The millimetre-wave spectrum is key to achieve multi-Gigabit/s data rates. The radio propagation in this spectrum has particular characteristics that have to be considered in the design of a wireless communication system. Besides telecommunications, the millimetre-wave radio frequencies are also applied to meteorological sensing [33], object detection [34] and medical radio-therapy [35].

The propagation in mmWave frequencies is different than in the lower radio frequencies used in previous network generations. The mmWave band has higher atmospheric attenuation due to water vapour and oxygen absorption. The attenuation has a peak at certain frequencies where they coincide with the mechanical resonant of the gas molecules, for instance, there is a peak in the loss at 60 GHz due to the oxygen resonance. The mmWave signal is highly affected by rain. The short wavelengths (1 to 10 mm) are comparable to a raindrop size, which is typically also in the order of millimetres. Hence, the mmWave signals are more vulnerable to blockage by raindrops than signals with longer wavelengths. For example, a monsoon down-pour with a rate of 150 mm/h has a maximum attenuation of 42 dB/km at frequencies over 60 GHz [7].

The short wavelengths also affect the wave propagation mechanisms, such as reflection, scattering and diffraction. Small structures that are comparable in size to the mmWave wavelength cause a rich diffused scattering, where each reflected ray has a different direction [36]. Thus, the reflected power is scattered, causing higher reflection attenuation[1] compared to signals with longer wavelengths. In general, any obstacle with size larger than the wavelength makes the wave to diffract with more difficulty around the obstacle. It also means that mmWave signals cannot propagate well through obstacles such as furniture, walls, and living organisms. In effect, these common objects, that are transparent to signals with longer wavelengths, become blockages to propagating mmWaves. For example, a concrete wall can attenuate the signal by up to 17.8 dB/cm in 40 GHz [36]. This high penetration loss can limit the range of outdoor-to-indoor signals, creating the need for heterogeneous networks with independent deployment to provide coverage in indoor environments. Furthermore, the presence of living beings, such as humans, between the transmitter and the

[1]The received power expected from the ideal reflection is decreased as the power is scattered in other directions.

receiver can drastically attenuate the received signal power. For example, the attenuation caused by a single human body can be as high as 20-40 dB [37].

Because of all these significant changes on propagation compared to lower radio frequencies, and also motivated by the potential use of the wide bandwidth available for enhancing the capacity of 5G networks, there has been a huge effort to characterise the mmWave channel [8, 38–48]. Hence, these characteristics should be applied on new channel models in order to correctly evaluate the performance of a mmWave system.

2.4 Modelling the Millimetre-Wave Channel

The mmWave systems are likely to be deployed in other scenarios than the traditional urban macro/micro environments. Additional scenarios, such as sports arenas, crowded festivals and transportation hubs, need to be considered, and each of them would have its own specific characteristics to be taken into account. Therefore, a new set of assumptions had to be made with respect the large- and small-scale fading effects in order to assess the impact of mmWave channel on the network performance on each of those scenarios. This makes the general characterisation of the fading channel a challenging task, as measurements across various propagation scenarios show that the strength of multi-path effects varies with the type of environment (office, car park, hallway, street), frequency (higher frequencies suffer more from shadowing), deployment (e.g. small-cells or device-to-device), or blockage conditions [1, 2, 48].

Another feature that has received much research attention are blockages, due to the fact that mmWave signals are highly attenuated by materials obstructing the direct path between the transmitter and receiver, causing significant disparity in the power received via the line-of-sight (LOS) and NLOS paths. A simple way to model this is to assume that the LOS probability function is a step function, i.e. the LOS probability of the link is taken to be one within a certain fixed radius and zero outside the radius. Yet, this simple random blockage model can provide us with a reasonable level of accuracy [26]. In [26], Bai and Heath have shown that there is a finite optimal AP density for coverage, with fixed AP and UE beamwidth configurations, which is given by the transition from a noise-limited regime to an interference-limited regime when increasing AP density. Blockage models for outdoor scenarios have been studied in [10, 26, 49, 50] and much of the modelling and their results are used for studying indoor scenarios as well. More accurate blockage models are highly dependable on the geometry of the environment, which is why ray-tracing tools with the scenario 3D model are widely adopted to assess the impact of blockages in site-specific scenarios [51, 52].

Moreover, the blockage caused by human bodies, both by the target user and by other pedestrians, is highly important to be considered in the mmWave network performance. Humans can be a ubiquitous element under the network deployment, and the obstruction

caused by their bodies is random and potentially frequent depending on the crowd density and movement. Because of that, there is a significant effort to properly characterise the human body blockage events [8, 10, 13, 14, 31, 53–57].

2.4.1 Human Blockage

The behaviour of human activity varies with the type of environment. For example, the mobility behaviour of pedestrians in an outdoor scenario such as in a urban street may differ from the behaviour in an indoor office. Modelling this activity is important in order to understand how the human body will obstruct the LOS and how it will affect the link performance. The modelling of human blockage can be affected by:

- **Blockage mobility.** The speed of the pedestrian influences the frequency and duration of obstructions [55].
- **Pedestrian density and dimensions.** Crowd scenarios and large body sizes may increase the chances of a blockage event [12].
- **Deployment configuration.** A ceiling-mounted transmitter may have more chances to be in LOS compared to a on-body transmitter in a device-to-device communication [11].
- **User equipment usage.** A mobile phone being used to operate an app may experience a different blockage condition from a phone held in a pocket [2].

A blockage model that correctly represents the intended scenario needs to define a set of assumptions according to the aspects above, but not necessarily limited to them. This set of assumptions will give a characterisation of the blockage probability, frequency or duration, allowing us to mathematically analyse the variation of the channel quality and its impact on the system performance. Since human body blockage attenuation can severely reduce the link channel quality, decreasing the data rate and eventually causing disconnection, it is highly critical to take into account the most suitable blockage model for the intended scenario. Therefore, a representative set of assumptions allows us to properly evaluate the mmWave system performance of a given scenario/environment under human body blockage effects.

In [10], Bai and Heath have proposed a cone blocking model to characterise the blockage by the user's body, and they have shown that self-body blocking effects can reduce the average throughput of dense outdoor mmWave networks by about 10%. Furthermore, coverage performance in dense indoor mmWave networks has been studied in [11, 13]. They have analysed the blockage probability of multiple bodies besides the user body, modelling human body blockages as circles randomly placed in a finite-area. In [11], Venugopal et al. have shown that, in device-to-device communication, interference in dense networks is significantly affected by blockage. This has also been shown by Niknam et al. in [13], where their results for a point process AP deployment have demonstrated that increasing blockage density improves coverage as the number of blocked interferers increases.

When considering the AP height, the geometry of the blocking objects becomes significant for the blockage analysis. As demonstrated by Gapeyenko et al. in [12], the received signal strength can be maximised when an optimal AP antenna height is deployed. This antenna height depends on the height and diameter distribution of the blockers. Also, considering both blocker and AP antenna height, there is an area around the AP where the blocker does not obstruct the link as the LOS goes over the obstruction, as observed in [14, 31, 56, 57]. These works use their analytical framework to study the optimal AP height or AP density that minimise the blockage probability.

2.5 Blockage Mitigation

Once we understand how the blockage is characterised, we can develop and evaluate mechanisms that mitigate the negative effects of blockage. The literature on blockage mitigation in mmWave communication is mostly focused on techniques that rely on spatial macrodiversity. Such techniques allow the transmitter to find an alternative physical path for the mmWave signal when the primary LOS path fails due to a blockage event. The main techniques considered are: (i) *reflectors*: usage of surfaces made of materials that reflect the mmWave signal to cover an obstructed spot through a NLOS path [17, 18]; (ii) *relays*: forwarding the transmission to a relay node that has an LOS path with the user equipment (UE) [19, 20]; (iii) *movable APs*: moving the AP location during the transmission to a position where there is an LOS path [21]; (iv) *multi-connectivity*: associating the UE with multiple APs, so the UE can have an LOS path to a backup AP [22, 23].

It is the responsibility of the medium access control (MAC) layer to coordinate the extra communication nodes (e.g., relay nodes, neighbour APs), and allow for a smooth handover between the APs, relays, or reflectors when the mmWave signal power fades due to blockage [58–61]. However, blockage intermittency may affect the utilisation of transmission resources (e.g., time, frequency, space), as a pre-allocated transmission can be interrupted by a blockage before being successfully received, and thus leading to resource under-utilisation. Therefore, to avoid that and improve capacity, the transmission resources should be properly allocated according to the blockage condition.

2.6 Blockage Prediction

Proper resource allocation can benefit from blockage prediction mechanisms to anticipate transmission before a blockage event. This allocation approach can be performed by predictive scheduling algorithms in the MAC layer. Prediction-based schedulers have been studied in the context of previous generations of wireless systems [62–65]. These schedulers rely on predicted and measured information that includes fading channel gains, mobility pattern (predicted route of a user through a region) and radio coverage map (mapping of measured

signal strengths to geographical locations). The prediction of the fading channel in the upcoming transmission intervals has allowed schedulers to estimate the achievable rates with increased precision, improving the network performance under the effects of rapid fluctuations of the received signal strength due to fast-fading at sub-6 GHz frequencies. However, as the accuracy of fading prediction can degrade rapidly with the prediction horizon (few milliseconds, depending on the mobility scenario) [64], the schedulers proposed in [62–64, 66] have to update their prediction and re-optimise scheduling every millisecond. When considering mobility, the scheduler in [65] uses the prediction of the mobility pattern together with the radio coverage map to estimate the achievable rate and allocate resources accordingly. It was shown in [65] that this approach can significantly improve network performance for slow-fading channels (caused by mobility).

There is a significant body of work on channel prediction, e.g., [62–65], which does not however include the effect of body blockage. At present, with the utilisation of mmWave spectrum, body blockage effects will become a significant design issue for 5G systems. Thus, new prediction methods have been recently studied in [67–70]. All of these works employ the capabilities of machine learning tools to predict blockages in mmWave links. The prediction is used to trigger anticipated antenna beam search or cell hand-off and reduce the latency of these processes. Still, these prediction methods do not provide the system with sufficient time to perform those processes before a significant change of the mmWave signal occurs [71]. Therefore, the authors in [71] proposed the utilisation of sub-6 GHz signal to provide an early warning of blockage in the mmWave signal. The method works within a hybrid communication system, where the sub-6 GHz and mmWave bands are employed simultaneously. The approach relies on diffracted sub-6 GHz signals that reach a specified received signal strength threshold much earlier than corresponding mmWave signals when an obstruction is crossing the LOS. For example, when the sub-6 GHz signal power falls by 30 %, it is estimated that the mmWave signal power will also fall by 30 %, but after some delay. Using this method, blockages can be forecasted up to tens of milliseconds ahead, giving the system sufficient time to adapt.

3 Capacity Analysis of Indoor mmWave Networks

Capacity Analysis of Indoor Millimetre-Wave Networks

In this chapter, we introduce our simulation framework that allows us to study dense deployments of millimetre-wave access points mounted on the ceiling, and illuminating selected spots on the ground with the use of fixed directional antennas. In this setup, the main factor limiting signal propagation is the blockage by the user body. We evaluate our system under a number of scenarios that take into account beamwidth of the main-lobe, access point density, and positioning of the mobile device with respect to the user's body. We find that both coverage and area spectral efficiency curves exhibit non-trivial behaviour which can be classified into four regions related to the selection of access point density, beamwidth, and antenna height values. Furthermore, we notice a non-trivial behaviour of the optimal beamwidth configuration with respect to the access point density when considering a ceiling-mounted deployment. These results can give a starting guideline for network designers to optimise the system parameters of an indoor deployment.

3.1 Indoor Millimetre-Wave Networks

The propagating mmWave signals suffer from high path attenuation and low penetration through materials such as building walls. It means that mmWave signals transmitted from outdoor base stations will be confined to streets and other outdoor areas [7]. This creates a situation where an independent tier of mmWave access points (APs) should be deployed to ensure coverage to user equipments (UEs) in indoor areas, as we illustrate in Fig. 3.1. Yet, coverage can still be deteriorated by human bodies, as they introduce as much as 40 dB of attenuation [8–10], which may be enough to lose the connection between AP and UE.

In order to combat the detrimental effects of blockages, one would be tempted to increase the AP density to maintain connectivity [10]. However, here comes another challenge — inter-cell interference. Although the increase in network density (densification) may improve the network capacity by allowing for an increase in spatial reuse [72], if not implemented carefully, it may lead to excessive interference causing a deterioration of the system's performance. In state-of-the-art literature, the interference mitigation can be achieved by inter-cell interference coordination (ICIC) techniques, which demand high signalling over-

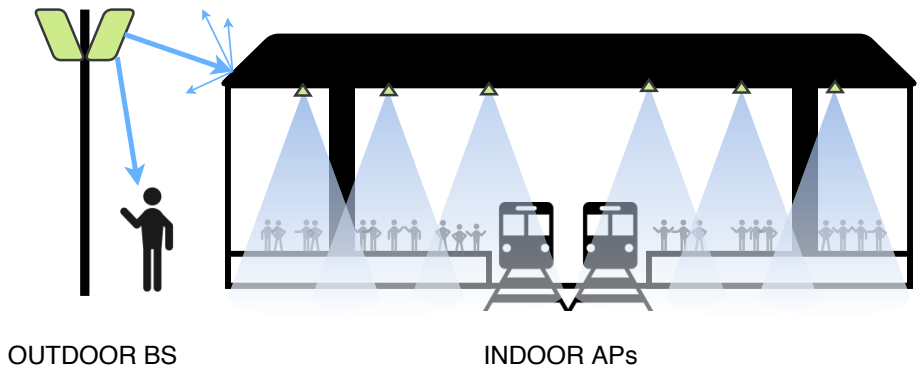

Figure 3.1: Independent tier of indoor millimetre-wave (mmWave) ceiling-mounted AP deployment providing coverage in a transportation hub with directional transmission pointing downward. The mmWave signal from outdoor base station (BS) does not propagate through building walls.

head [27]. One simpler way to reduce the interference is to restrict the signal propagation through the use of directional antennas mounted on the ceiling. Thus, the main-lobe of the directional antenna beam is pointed downwards to confine the signal's power to a limited space.

Ceiling installations of mmWave access points have been considered in the literature, e.g., [30–32], yet proposed analysis was restricted to single link performance. While, in state-of-the-art literature, we can find coverage and throughput analysis of such deployments operating in microwave frequencies, e.g., [29], the same analysis for deployments operating in mmWaves becomes more complicated due to the susceptibility to blockages. To address this, in this chapter we consider a large indoor scenario where APs operating in mmWave frequencies (mmWave APs) are mounted on the ceiling to form a grid-like pattern, and fixed directional transmissions are set to illuminate selected spots on the ground. We consider a confined venue, where we assume that there is no outdoor-to-indoor interference. Then, we analyse the effects of basic design parameters (such as the AP density and antenna beamwidth) on the network performance through our simulation framework. Based on an extensive simulation campaign, we find that coverage and area spectral efficiency (ASE) achieve peak performance when there is a joint optimal beamwidth configuration of the ceiling-mounted AP antennas facing downwards and the directional UE antennas facing the AP, for a given AP density.

In what follows, we provide a description of our system model, and in-depth analysis of the numerical results obtained, with lessons learnt on the design of dense indoor mmWave networks.

3.2 System Model

In this section, we introduce our model of a mmWave indoor network. The considered environment is an indoor confined area where there is no interference from outdoor signals.

The APs are deployed on a hexagonal grid, and they are installed on the ceiling at some height above the UE level, with fixed directional antennas illuminating the floor below. We consider a UE randomly located in the square-shaped indoor venue. The AP that provides the desired signal to the UE is referred to as the serving AP, while the other APs are referred to as interfering APs. In our notation, we use the subscript $_{\mathrm{A}}$ to denote the parameters related to the AP, the subscript $_{\mathrm{U}}$ to denote the parameters related to the UE, and the subscript $_{\mathrm{B}}$ to denote the body parameters. We assume human bodies are the main source of blockages for the mmWave signals and change the link state between line-of-sight (LOS) and non-line-of-sight (NLOS). Thus, we assume that both path loss and channel gain have different characteristics in each state. These characteristics are modelled according to empirical channel measurements described in [1].

3.2.1 Directivity Gain

We assume the APs utilise fixed directional transmission due to its advantage of simplicity. It does not require phase shifters, which usually require complex processing for precise adjustments [28]. We assume the UEs can steer the directional reception, which is perfectly aligned to the direction of the serving AP, since there are efficient beam search techniques for static devices within short distances in mmWave systems [73].

We assume the antenna pattern follows the "cone-bulb" model, which allocates the most significant part of the signal's energy to the main-lobe, as illustrated in Fig. 3.2a, while conserving the total energy of the propagating signal [74]. The "cone" represents the main-lobe attached to a single "bulb" representing the side-lobe. The main-lobe directivity gain is given by m, s is the side-lobe gain, ω_{A} is the beamwidth of the main-lobe, cap is the area of the spherical cap, and sph is the surface area of the sphere of radius r. The directivity gain is then a function of the beamwidth, normalised over a given spherical surface as in:

$$m \cdot \frac{\mathrm{cap}}{\mathrm{sph}} + s \cdot \frac{\mathrm{sph} - \mathrm{cap}}{\mathrm{sph}} = 1, \tag{3.1}$$

where $\mathrm{cap} = 2\pi r^2 \left(1 - \cos \frac{\omega_{\mathrm{A}}}{2}\right)$, and $\mathrm{sph} = 4\pi r^2$. Thus, fixing the side-lobe gain s, we can calculate the main-lobe gain as a function of the beamwidth, as illustrated in Fig. 3.2b:

$$m = \frac{2 - s\left(1 + \cos \frac{\omega_{\mathrm{A}}}{2}\right)}{1 - \cos \frac{\omega_{\mathrm{A}}}{2}}. \tag{3.2}$$

AP Directivity Gain

The signal has the maximum transmit directivity gain m when the UE is positioned under the area illuminated by the AP's main-lobe, i.e., the UE is inside the projected circle of radius:

$$r_m^{\mathrm{A}} = h_{\mathrm{A}} \cdot \tan \frac{\omega_{\mathrm{A}}}{2}, \tag{3.3}$$

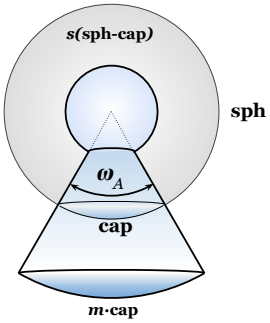

(a) Cone-bulb model approximation of antenna directivity gain patterns. The cone represents the main-lobe and the bulb (inner sphere) represents the side-lobe. The cap area cap is scaled up by a factor of m, while the resulting bulb area sph − cap is scaled down by a factor of s.

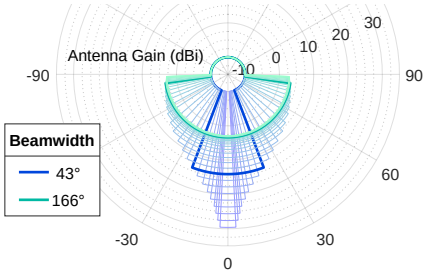

(b) Antenna directivity gain pattern for different beamwidths, according to (3.2).

Figure 3.2: Directional antenna model.

as illustrated in Fig. 3.3. Otherwise, the transmit directivity gain is the side-lobe gain s. Therefore, we can express the transmit directivity gain as:

$$G^{\mathrm{A}} = \begin{cases} m, & d_{\mathrm{A}} \leq r_m^{\mathrm{A}}; \\ s, & \text{otherwise}; \end{cases} \tag{3.4}$$

where d_{A} is the projection of the distance from the AP to the UE onto the horizontal plane.

UE Directivity Gain

The signal has the maximum receive gain m when the UE's main-lobe illuminates the transmit AP. We consider the UE's main-lobe is pointed towards the serving AP. Thus, an AP is illuminated by the UE's main-lobe cone when the AP is located in the conic[1] shape projected around the serving AP on the ceiling surface, as illustrated in Fig. 3.4. As the UE gets further apart from the serving AP, the UE's main-lobe elevation lowers, and eventually, the lateral surface of the cone becomes parallel to the UE level, making the illuminated area in the ceiling to transit from bounded to unbounded. This event happens at a distance of

[1]In mathematics, a conic section (or simply conic) is a curve obtained as the intersection of the surface of a cone with a plane.

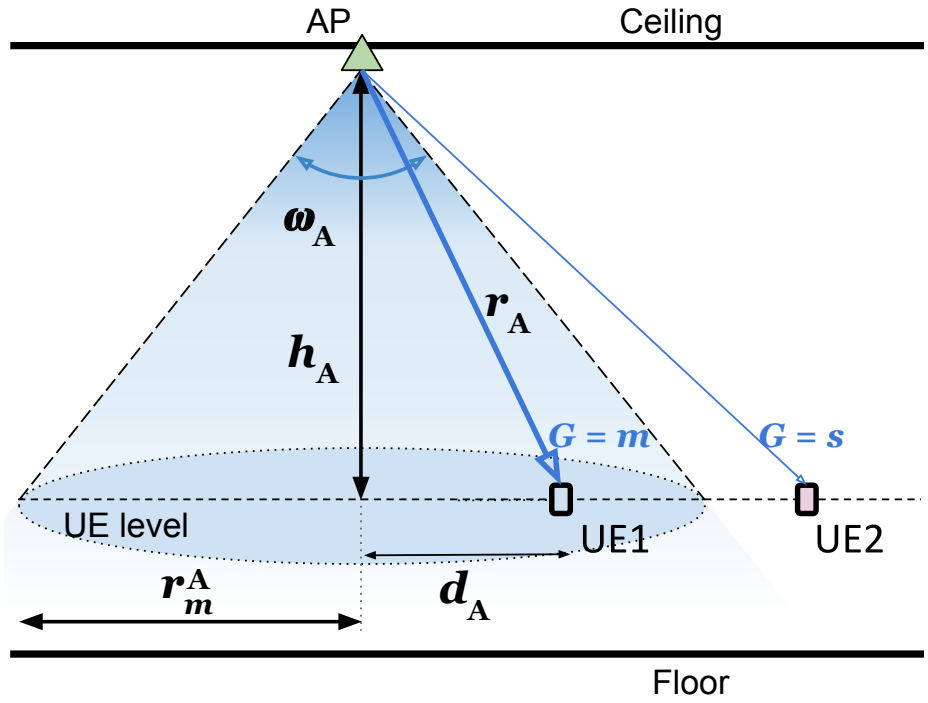

Figure 3.3: AP directional transmission with beamwidth ω_A illuminating a circle with radius r_m. The received signal power of UE1 inside the circle has a directivity gain m from the AP at an Euclidean distance r_A, while the received signal power of UE2 outside the circle is scaled by s.

d_U:

$$d_U = \frac{h_A}{\tan \frac{\omega_U}{2}}. \tag{3.5}$$

Hence, we assume that, if the UE is close to the serving AP, i.e., $d_A < d_U$, the illuminated area is bounded and the conic shape is approximated by a circle of radius r_m^U:

$$r_m^U = h_A \cdot \tan \frac{\omega_U}{2}, \tag{3.6}$$

If the UE is far enough from the serving AP, i.e., $d_A \geq d_U$, the conic projected in the ceiling becomes unbounded, thus we assume that the illuminated area is approximated by a circular sector[2] with central angle equal to the UE beamwidth, as illustrated in Fig. 3.4b. Thus, since the UE's directionality is aligned with the serving AP orientation, an AP is illuminated by the UE's main-lobe when the AP orientation falls within the illuminated area around the serving AP. Therefore, we can express the receive directivity gain as:

$$G^U = \begin{cases} m, & \left(d_A < d_U \ \cap \ d_A \leq r_m^U\right) \cup \\ & \left(d_A \geq d_U \ \cap \right. \\ & \left. \theta_S - \frac{\omega_U}{2} < \theta_A < \theta_S + \frac{\omega_U}{2}\right); \\ s, & \text{otherwise;} \end{cases} \tag{3.7}$$

[2]A circular sector is the portion of a disk enclosed by two radii and an arc. The length of the radii is limited by the deployment area.

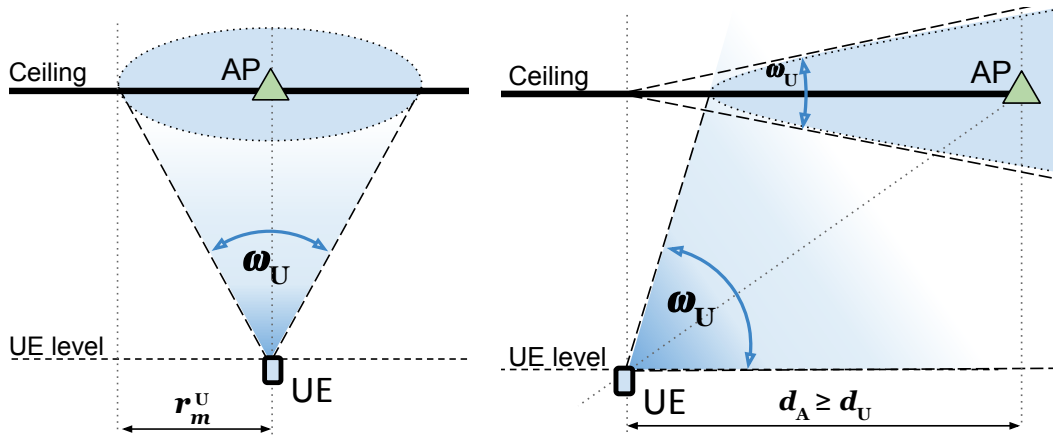

(a) Bounded illumination area is a circle.

(b) Unbounded illumination area is a circular sector.

Figure 3.4: UE directional reception with beamwidth ω_U illuminating a conic section on the ceiling surface. The received signal power from an AP inside the cone has a directivity gain m, while the received signal power from an AP outside the cone is scaled by s.

where θ_A is the orientation of the given AP and θ_S is the serving AP orientation.

3.2.2 Self-Blockage Model

In our scenario, the only source of blockage is the user body. In this model, the main factor that describes how likely it is for the user body to shadow signals to/from the UE is the UE's position with respect to the body. We assume that the user body facing the UE shadows an area given by a rectangle of height h_B and width w_B. The UE is in front of the body at a distance r_0 from the body centre as shown in Fig. 3.5. In the horizontal plane, the obstructed space can be quantified by its angle (shadowing angle) $\phi_B = 2\arctan(w_B/2r_B)$. The parameter h_B determines the space obstructed by the body in the vertical plane.

Given the body blockage and our ceiling-mounted deployments, we can construct a model of user device shadowing as depicted in Fig. 3.5. From the geometry of the model, and assuming all APs at the same height h_A, we define z_0 as the radius of the *self-blockage free zone* for a given UE-body pair (illustrated in Fig. 3.5a):

$$z_0 = h_A \cdot \frac{r_0}{h_B}, \tag{3.8}$$

where an AP inside this zone will always be in LOS with the UE, regardless of the user body orientation. The APs outside this zone will have the LOS obstructed whenever the body is in between the UE and the AP (considering their projections onto the two-dimensional plane). Therefore, assuming uniform body orientation, the probability of self-body blockage is given by

$$p_0(d_A) = \begin{cases} \dfrac{\arctan(w_B/2r_0)}{\pi}, & d_A \geq z_0; \\ 0, \quad 0 < d_A < z_0; \end{cases} \tag{3.9}$$

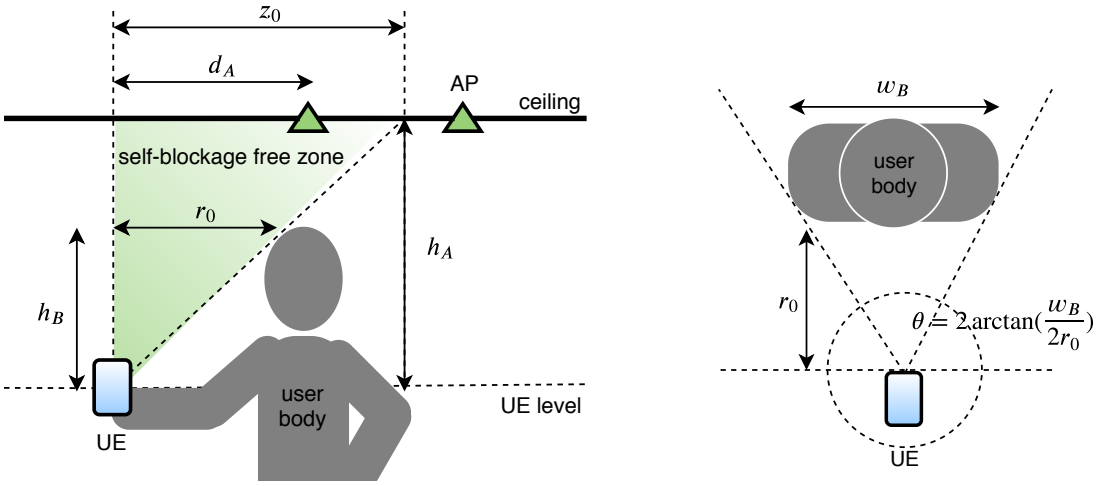

(a) Side view

(b) Top view.

Figure 3.5: Obstruction by a body may happen when the AP is beyond the radius z_0. On the other hand, an AP within this radius is not obstructed, regardless the body orientation with respect to the UE, i.e., the AP is inside the *self-blockage free zone* represented by the green area.

3.2.3 Signal-to-Interference-plus-Noise Ratio

In this chapter, we make the following assumptions to compute the SINR:

Assumption 1. *We assume that the blockage event for each AP is independent, i.e., there is no correlation in the blockage process of APs near each other, even though in reality they could be blocked by the same body [11].*

Assumption 2. *We model the mmWave signal propagation considering the experimentally-validated channel model proposed in [1]. The model is composed of the path loss, large-scale fading (shadowing) and small-scale fading, whose parameters assume one of two values according to the blockage state X. We assume the path loss conditioned on $X = x \in \{\text{LOS}, \text{NLOS}\}$ is:*

$$L_x = \ell_x \cdot r_{\text{A}}^{-\nu_x}, \tag{3.10}$$

where ℓ_x is the path loss at 1 metre distance under free space propagation, ν_x is the attenuation exponent, $r_{\text{A}} = \sqrt{d_{\text{A}}^2 + h_{\text{A}}^2}$ is the Euclidean distance from the AP to the UE, and d_{A} is the projection of the distance from the cell centre to the UE onto the horizontal plane (we refer to this as 2D-distance, as shown in Fig. 3.3). We assume the shadowing is modelled as Gamma distribution and the small-scale fading as Nakagami-m.

We express the received power at the UE from an AP with blockage state $X = x$ as:

$$P_{\text{r},x} = p_{\text{t}} \cdot G_x^{\text{A}} \cdot G_x^{\text{U}} \cdot L_x \cdot B_x \cdot H_x, \tag{3.11}$$

where p_{t} is the transmit power, G_x^{A} is the AP directivity gain given in (3.4), G_x^{U} is the UE

directivity gain given in (3.7), L_x is the path loss given in (3.10), B_x is the shadowing gain, and H_x is the small-scale fading gain.

Based on the assumptions made above, we can express the SINR at a UE as follows :

$$\mathrm{SINR} = \frac{G^{\mathrm{A}}_{x_i} \cdot G^{\mathrm{U}}_{x_i} \cdot L_{x_i} \cdot B_{x_i} \cdot H_{x_i}}{\frac{\sigma}{p_{\mathrm{t}}} + \sum_{j \in \mathcal{A} \setminus \{i\}} G^{\mathrm{A}}_{x_j} \cdot G^{\mathrm{U}}_{x_j} \cdot L_{x_j} \cdot B_{x_j} \cdot H_{x_j}}, \tag{3.12}$$

where $i \in \mathcal{A}$ is the serving AP, with $\mathcal{A}$ denoting the set of APs, and σ is the thermal noise power. Note that, because X is a random event, G^{A}_x, G^{U}_x, L_x are random variables whose distributions are functions of the system parameters (ω_{A}, ω_{U}, h_{A}, r_B, h_B, w_B). A summary of all the system deterministic parameters and random variables is provided in Table 3.1 and in Table 3.2, respectively.

3.3 Numerical Results

3.3.1 Simulation Setup

We model our scenario by placing the APs in the centres of a hexagonal cell pattern laid over a $400 \times 400\,\mathrm{m}^2$ area, as exemplified in Fig. 3.6.

This specific choice of the area size allows us to explore the system behaviour for large inter-site distances (up to 200 m). The side-lobe gain is fixed at $-10\,\mathrm{dB}$, and the main-

Table 3.1: Summary of the System Deterministic Parameters

Body Parameters		**Deployment Parameters**	
Body width	w_{B}	AP height	h_{A}
Body height	h_{B}	AP beamwidth	ω_{A}
Distance from UE to user body (UB)	r_0	Inter-site distance	δ
		UE beamwidth	ω_{U}
Signal Power Parameters		**Directivity Gain Parameters**	
Noise power	σ	Main-lobe gain	m
Transmit power	p_{t}	Side-lobe gain	s
		Illumination radius	r_m

Table 3.2: Summary of the System Random Variables

Deployment Variables		**Signal Power Variables**	
Distance from UE to AP	r_{A}	Directivity gain	G
2D projection of r_{A}	d_{A}	Path gain	L
		Shadowing gain	B
		Small-scale fading gain	H
		Received power	P_{r}

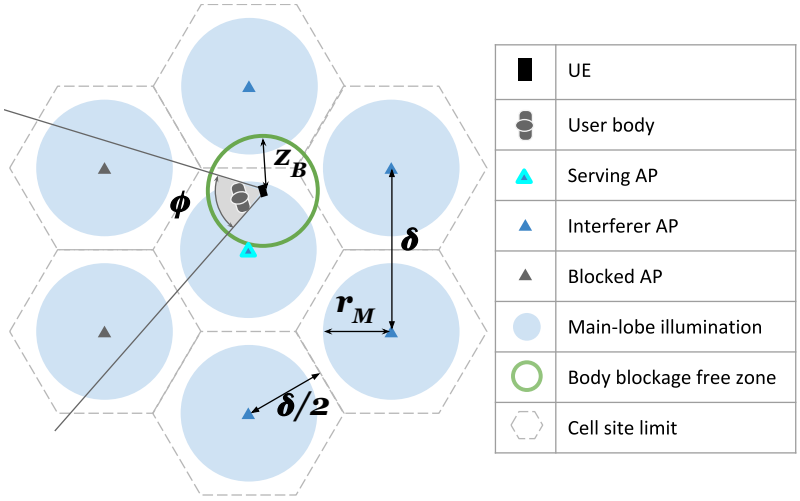

Figure 3.6: Snapshot from simulations illustrating the system model. The APs are distributed according to a hexagonal cell pattern with an inter-site distance δ. The user body is blocking the signal from the grey-coloured APs inside the angle ϕ. The UE is illuminated (light-blue area) by the serving AP, which is outside the blockage free zone (green circle). Note that in a very dense topology, where δ could be as small as z_{B}, there will always be an AP (serving or interfering) in LOS.

Table 3.3: Channel Parameters (based on [1, Table I])

Channel	Path Loss		Shadowing		Small-Scale Fading
	ν	ℓ (dB)	α	β	m
LOS	1.72	63.4	4.48	0.27	3.02
NLOS	1.94	65.3	1.18	1.52	4.68

lobe gain varies with the beamwidth according to (3.2). We evaluate the system for a fixed AP height $h_{\mathrm{A}} = 10\,\mathrm{m}$. Note that, changing h_{A} has essentially the same impact on the performance as changing the AP beamwidth, since both h_{A} and ω_{A} determine the main-lobe illumination area; as a matter of fact, when testing our system for other height values of interest (e.g., heights from 1 to 10 m), we observed no significant deviations from the conclusions presented here. We set the transmit power as 20 dBm, bandwidth as 2 GHz, carrier frequency as 60 GHz, as recommended by ITU-R [75]. We assume perfect equalisation in the frequency domain as the impact of frequency selectivity can be significantly reduced using effective modulation and equalisation techniques for 60 GHz frequencies [76]. We set noise figure as 9 dB, and the body parameters w_B as 40 cm and h_B as 40 cm. We consider the UE is associated with an AP corresponding to the strongest long-term received signal power, i.e., without considering small-scale fading gain. We set $r_0 = 30\,\mathrm{cm}$ as to represent a scenario of a user operating the UE with the *hand*. We set the channel parameters as measured for a car park environment according to Table 3.3 (based on [1, Table I]). To evaluate the network performance, we consider the following metrics: SINR coverage and ASE. We define the SINR coverage as the probability that the SINR at the UE is larger than the threshold ζ=5 dB, i.e., $\mathsf{P}[\mathrm{SINR} > \zeta]$, as to ensure high data rate reception with

low bit error rate using advanced modulation and coding schemes. The ASE is the average spectral efficiency, $\mathsf{E}[\log(1+\mathrm{SINR})]$, divided by the cell area.

3.3.2 Coverage and ASE Profile

In this subsection, we evaluate the effect of the inter-site distance δ (network density) on coverage and ASE of a mmWave indoor network with ceiling-mounted APs. Our investigation reveals that in the ceiling-mounted AP setup, the SINR coverage and ASE present a non-trivial behaviour which can be classified into four regions of operation, as illustrated in Fig. 3.7.

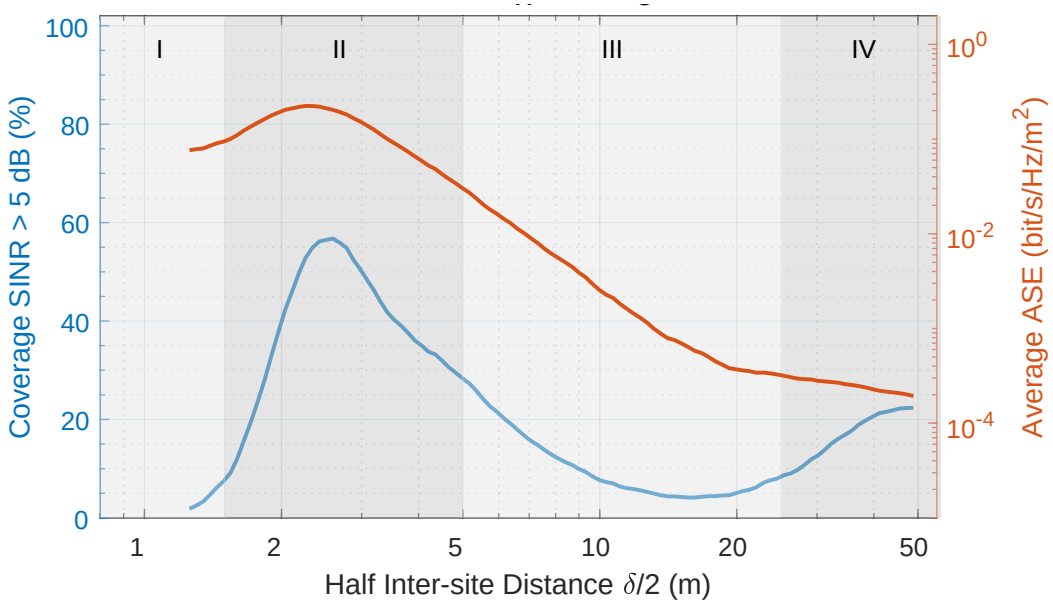

Figure 3.7: Coverage (left y-axis, blue curve) and ASE (right y-axis, red curve) profile versus inter-site distance when AP beamwidth is 28 ° and UE beamwidth is 45 °. Regions delimited by grey rectangles represent the non-trivial behaviour of coverage with respect to AP density.

These regions appear as we change the inter-site distance while keeping the AP and UE beamwidths fixed:

(I) **High main-lobe interference**: at high AP density (short δ), the beam is too large and causes substantial overlaps among adjacent cells, which results in high interference and, thus, low coverage. However, since the cell area is very small, the ASE is high.

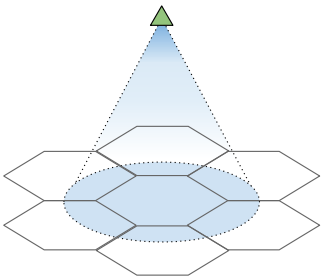

Region I

(II) **Minimum main-lobe interference**: the main-lobe illuminates the entire cell with minimum interference to neighbouring cells. Although it yields high coverage, the coverage can be limited by the UE's main-lobe beamwidth when large UE beamwidths illuminate more neighbouring APs and increase interference power. Thus, strong serving signal and minimised interference lead to increased SINR and to high ASE.

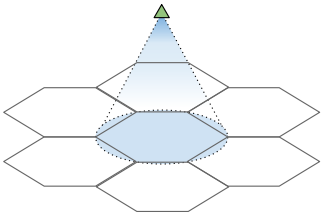

Region II

(III) **Low main-lobe illumination**: at intermediate AP densities, the coverage is very low due to the lack of main-lobe illumination by the serving AP and due to the presence of neighbouring side-lobe interference; however, this interference decreases as the deployment gets sparser and fewer APs are illuminated by the UE main-lobe, increasing coverage again. At the same time when we move towards a sparser deployment, as the cell size becomes larger, the ASE is reduced.

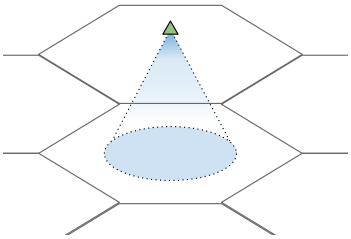

Region III

(IV) **High path loss**: in low AP density (large δ), the illuminated area by the AP's beam is so small, compared to the cell area, that it becomes negligible. Hence, the only signal that can be picked up by the majority of users comes from the side-lobes. Therefore, the UE receive antenna gain plays a major role in mitigating the high path loss and the AP side-lobe attenuation. The large cell area contributes to an ASE even lower than for the other regions.

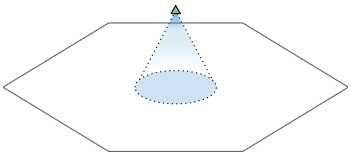

Region IV

Based on these results, it is clear that a network operating in Region II reaches peak coverage performances. We explore the coverage behaviour for a range of AP and UE

beamwidths to identify the configurations that maximise coverage for each inter-site distance δ. In Fig. 3.8, we indicate the peak coverage with a solid black line. The AP and UE beamwidth configurations that lead to that coverage, for a given δ, are indicated by the colours above and below the line, respectively. With such configurations, we observe that the peak coverage is high for any inter-site distance.

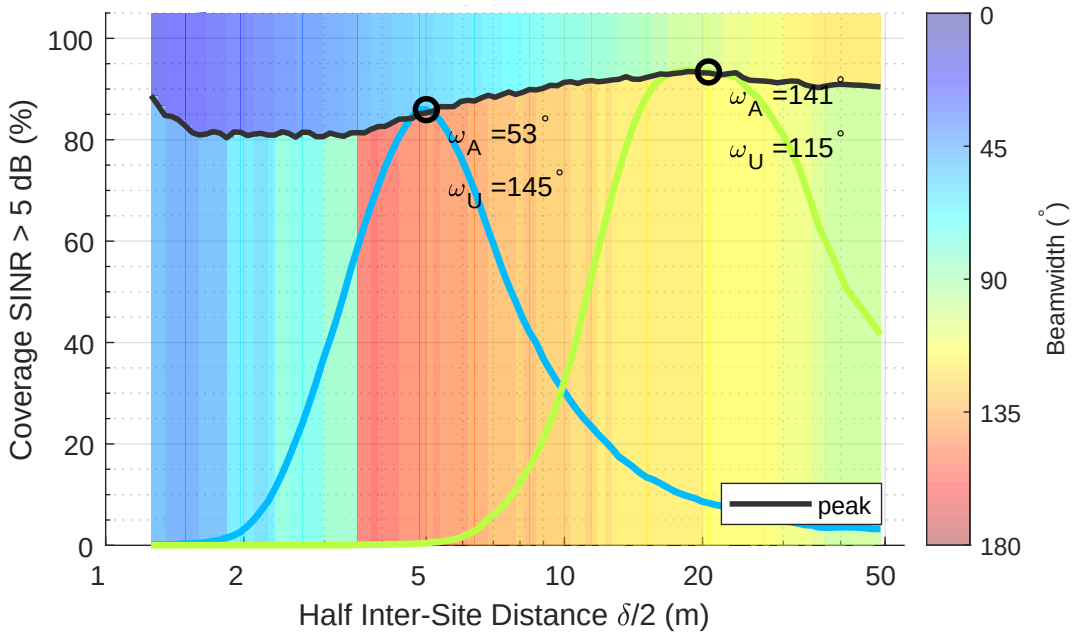

Figure 3.8: Peak coverage as a function of the AP density. The solid black line denotes the maximum performance achieved for a given inter-site distance with the AP and UE beamwidths optimised for coverage. The coloured bars above the line indicate the optimal AP beamwidth for a given inter-site distance, and the coloured bars below the line indicate the optimal UE beamwidth.

One can see the colour variation on the bars above and below the black line, where cold colours represent small beamwidths and warm colours large beamwidths. *This indicates that, for each AP density, there is a specific optimal AP and UE configuration that maximises coverage.* We observe that, when increasing the cell size, larger AP beamwidths (warmer colours) are needed to achieve the peak coverage, as there is the need to illuminate the entire cell. However, UE beamwidth does not have the same monotonic behaviour: With very small cell sizes ($\delta < 2\,\text{m}$), the UE beamwidth is small (cold colours), so it does not illuminate many neighbouring APs, and thus, avoids increased interference. As the cell size increases, the average distance between the UE and the serving AP also increases. Hence, the UE's main-lobe tends to illuminate an increased area, as the main-lobe elevation lowers with the distance to the serving AP. Thus, the UE antenna should have large beamwidths (with low directivity gain, warm colours) that do not enhance the signal power from the illuminated APs (especially the closer ones) as much as small beamwidths do. Then, as the cell size becomes large ($\delta > 5\,\text{m}$), the serving AP moves further and further away, and

high directivity gain is needed to compensate for the increased path loss, decreasing the UE beamwidth.

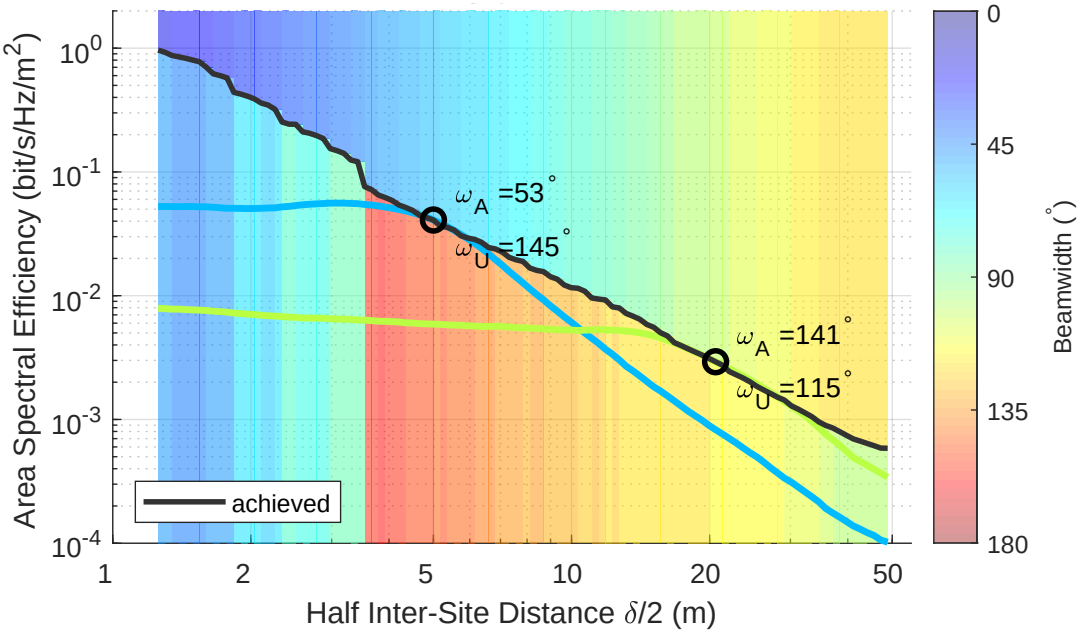

Figure 3.9: Average ASE as a function of the AP density. The black solid line denotes the performance achieved for a given inter-site distance with the AP and UE beamwidths optimised for coverage. The coloured bars above the line indicate the optimal AP beamwidth for a given inter-site distance, and the coloured bars below the line indicate the optimal UE beamwidth.

In Fig. 3.9, we draw a solid black line that represents the ASE achieved when using the optimal configuration for coverage. We see that the achieved ASE decreases due to both the increased cell area and increased path loss on the serving AP signal power. Therefore, as peak coverage and achieved ASE have opposite trends with respect to the cell size, there is a trade-off between these two performance metrics.

3.4 Conclusion

In this chapter, we studied the network design aspects of ceiling-mounted mmWave AP deployments with directional antennas over a confined area. We showed that, each densification level will require individual AP and UE main-lobe beamwidths configurations to achieve maximum coverage operation. The AP beamwidth increases with the cell size, as it needs to illuminate the entire cell with minimum interference to neighbouring cells. Small UE beamwidths can boost the signal from far APs in sparse deployments, while in dense deployments large UE beamwidths are more beneficial. Furthermore, we demonstrated the necessity for network designers to carefully consider their intended application as there is a fundamental trade-off where same AP/UE beamwidth and density configurations that

optimise coverage do not optimise ASE.

Building on top of the framework introduced in this chapter, we will analyse the impact of body blockages on the performance of ceiling-mounted mmWave AP deployments, since the trade-off presented in this chapter can be more significant when other blockage scenarios are evaluated. In the following chapter, we will also analyse how the blockage will impact on the network deployment design. For that, we extend the blockage model to comprehend not only the self-blockage but also the blockage of other random bodies, and analyse the blockage probability in indoor ceiling-mounted deployments.

4 Performance Analysis of Indoor mmWave Networks under Human Blockage

Performance Analysis of Indoor mmWave Networks under Human Blockage

In this chapter, we study the impact of human body blockage on dense deployments of millimetre-wave access points mounted on the ceiling, with directional antennas pointing downwards to illuminate selected spots on the ground. Here, we develop a body blockage model and derive an expression for the probability of blockage. Using the developed expressions and the simulation framework introduced in Chapter 3, we assess the impact of body blockage on the achievable performance and the system design. We find that the trade-off between coverage and spectral efficiency becomes more significant as coverage degrades with more severe blockage scenarios and that there is an optimal beamwidth-density configuration that only maximises either coverage or area spectral efficiency. Such optimal configuration changes depending on the body blockage probability, leading to a necessity for network designers to carefully consider their intended application and scenario.

4.1 Human Body Blockage

The electromagnetic waves of a millimetre-wave (mmWave) signal cannot "travel around" the objects whose size is larger than their wavelengths. This makes human bodies, both user and the crowd around the user, blocking obstacles, since as demonstrated in [8–10], body blockage can attenuate the line-of-sight (LOS) signal by up to 40 dB. Moreover, human bodies are a ubiquitous obstruction in any mmWave cellular network, which can make the network operation quite challenging. Therefore, to understand the performance bounds of mmWave systems, it is essential to predict the probability of having the LOS blocked at a particular instant of time in a crowded environment [57].

The probability of blockage highly depends on the considered deployment. Each deployment (i.e., indoor ceiling-mounted, outdoor streets, device-to-device) has its own peculiar geometry, which makes the modelling of a general blockage probability untractable. Furthermore, the probability varies with the scenario. In a ceiling-mounted access point (AP) deployment, a receiver very near the transmitter (e.g. a user right under the AP) is very unlikely to be blocked. When the receiver gets further away from the AP, there are more chances for a body to obstruct the LOS. These chances may increase when considering a

dense crowd around the user or when the user equipment (UE) is held closer to the user body, as the body shields a greater area. Therefore, we focus our analysis on the ceiling-mounted AP deployment taking the above mentioned situations into account in the modelling of the probability of human blockage. Hence, we study the effects of different blockage scenarios on the optimal system design parameters (such as AP density and antenna main-lobe beamwidth) and on the network performance. For this purpose:

- We develop a model of body blockage that matches the geometry of the ceiling-mounted AP deployment, and we derive an analytical expression for the probability of blockage to reduce the system-level modelling complexity.
- We analyse the impact of body blockage on the performance and system design through our simulation framework.

Based on an extensive simulation campaign:

1. We find that there exists a trade-off in beamwidth-density configuration, in which the same configuration optimises either coverage or ASE, but not both.
2. We find that the optimal beamwidth-density configuration for coverage depends on the body blockage probability, as the configuration needs to compensate for increased interference, shadowing or path loss.

In what follows, we provide an overview of the related literature, description of our system model, analysis of the blockage probability, and in-depth analysis of the numerical results obtained, and explaining the lessons learnt on the design of dense indoor mmWave networks under human body blockage.

4.2 System Model

The system modelled in this section considers the indoor mmWave network described in Chapter 3, i.e., the APs are deployed on a hexagonal grid, and they are installed on the ceiling at some height above the UE level, with fixed directional antennas illuminating the floor below. Therefore, we consider the same directivity model and channel model described in Sections 3.2.1 and 3.2.3. In this chapter, we extend the self-blockage model to consider multiple bodies that can potentially block the UE. As a reminder, we use the subscript $_{\mathrm{A}}$ to denote the parameters related to the AP, the subscript $_{\mathrm{U}}$ to denote the parameters related to the UE, and the subscript $_{\mathrm{B}}$ to denote the body parameters. A summary of all the system deterministic parameters and random variables is given in Table 4.1 and in Table 4.2, respectively.

4.2.1 Body Blockage Model

In this extended scenario, the sources of blockage are, besides the user body, bodies randomly placed around the UE. In this model, we generalise the description of the self-blockage by

describing the model parameters for a generic body. We assume that a body facing[1] the UE shadows an area given by a rectangle of height h_{B} and width w_{B}. The UE is in front of the body at a distance r_{B} from the body centre, as shown in Fig. 4.1. In the horizontal plane, the obstructed space can be quantified by its angle (shadowing angle) $\phi_{\mathrm{B}} = 2\arctan(w_{\mathrm{B}}/2r_{\mathrm{B}})$. The parameter h_{B} determines the space obstructed by the body in the vertical plane.

We assume that the signal from an AP can be obstructed by the user body (UB) (the body holding the UE) or by other random bodies (RBs). We define these events as *self-body blockage* and *random-body blockage*, respectively. We assume that all bodies (UB and RBs) have the same size (w_{B} and h_{B} are constant). The UB is fixed at distance r_0 from the UE, while the RBs are uniformly placed, thus the distance r_{B} from the UE to an RB is random. We define the orientation θ with respect to the body as the angle between two lines: the line joining the UE to the body's right shoulder and the line joining the UE to the AP. Then, we assume that the UB and RB orientations, θ_0 and θ_{B} angles respectively, are uniformly distributed in $[0, 2\pi)$.

Given the body blockage and our ceiling-mounted deployments, we can construct a model of user device shadowing as depicted in Fig. 4.1. From the geometry of the model,

[1]Without loss of generality, we assume that all bodies, not only the user's body, are facing the UE. The effect of having a body not perpendicular to the UE, i.e. smaller w_{B}, is to have a smaller blocking angle, which is equivalent to the body being at a longer distance r_{B}.

Table 4.1: Summary of the System Deterministic Parameters

Body Parameters		**Deployment Parameters**	
Body width	w_{B}	AP height	h_{A}
Body height	h_{B}	AP beamwidth	ω_{A}
Distance from UE to user body (UB)	r_0	Inter-site distance	δ
		UE beamwidth	ω_{U}
Signal Power Parameters		**Directivity Gain Parameters**	
Noise power	σ	Main-lobe gain	m
Transmit power	p_{t}	Side-lobe gain	s
		Illumination radius	r_m

Table 4.2: Summary of the System Random Variables

Body Blockage Variables		**Signal Power Variables**	
Body shadowing angle	ϕ_{B}	Directivity gain	G
Body orientation angle	θ_{B}	Path gain	L
Distance from UE to random body (RB)	r_{B}	Shadowing gain	B
Blockage free zone radius	z_{B}	Small-scale fading gain	H
		Received power	P_{r}
Deployment Variables			
Distance from UE to AP	r_{A}	2D projection of r_{A}	d_{A}

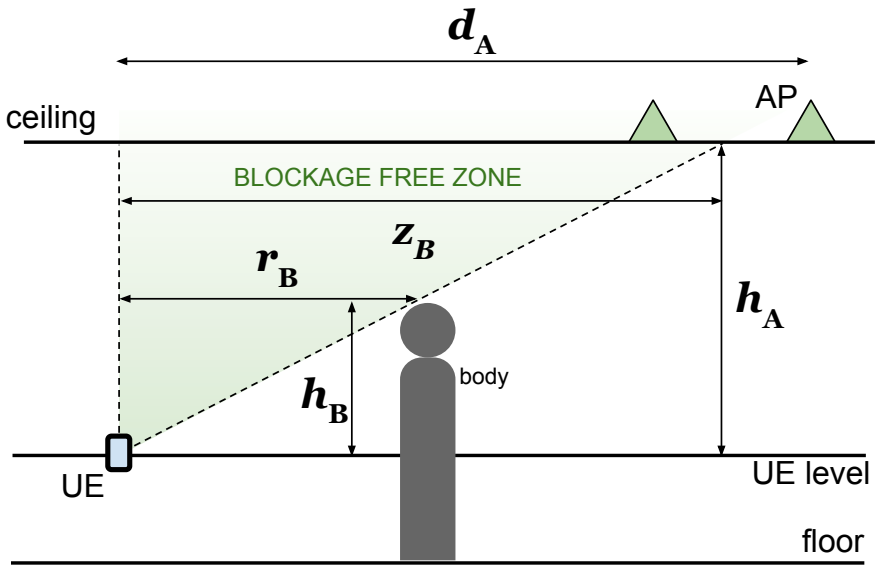

(a) Side view. Obstruction by a body may happen when the AP is beyond the radius z_B. On the other hand, an AP within this radius is not obstructed, regardless the body orientation with respect to the UE, i.e., the AP is inside the *blockage free zone* represented by the green area.

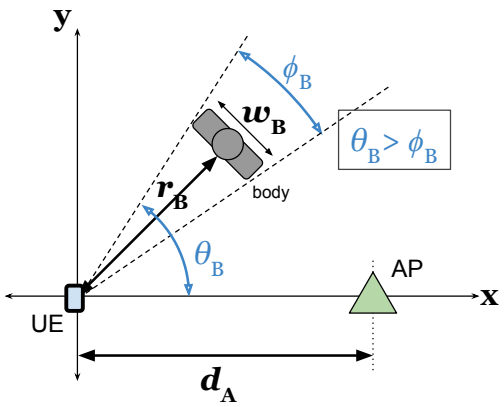

(b) Top view. The body is not between the AP and the UE when the shadowed angle ϕ_B is less than the angle θ_B.

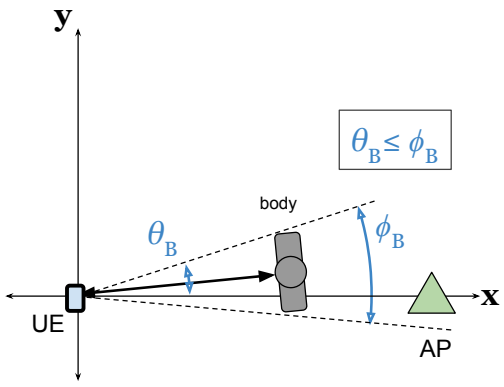

(c) Top view. The body is between the AP and the UE, and possibly blocking the AP, when the shadowed angle ϕ_B is greater than the angle θ_B.

Figure 4.1: Body blockage model. The body is at a distance of r_B from UE, and height h_B from UE level, and has a width w_B.

and assuming all APs at the same height h_A, we define z_B as the radius of the *blockage free zone* for a given UE-body pair (illustrated in Fig. 4.1a):

$$z_B = h_A \cdot \frac{r_B}{h_B}, \tag{4.1}$$

where an AP inside this zone will always be in LOS with the UE, regardless of the body orientation. The APs outside this zone will be obstructed whenever the body is in between the UE and the AP (considering their projections onto the two-dimensional plane). For a given distance between UE and AP, and a given distance between UE and body blockage,

and $\mathbb{1}(.)$ denoting the indicator function, we define the following events:

Definition 1. *The event 'AP outside' = [the AP is outside the blockage free zone], as illustrated in Fig. 4.1a, occurs when the distance d_{A} from the AP to the UE is greater than the blockage free zone radius z_{B}, i.e.:*

$$\mathsf{P}(AP\ outside) = \mathbb{1}(d_{\mathrm{A}} > z_{\mathrm{B}}). \tag{4.2}$$

Definition 2. *The event 'body between' = [the body is in between the AP and the UE], as illustrated in Fig. 4.1c, occurs when the body orientation angle $\theta_{\mathrm{B}} \in [0, 2\pi)$ is smaller than the body shadowing angle $\phi_{\mathrm{B}} \in [0, \pi)$, i.e.:*

$$\mathsf{P}(body\ between) = \mathbb{1}(\theta_{\mathrm{B}} < \phi_{\mathrm{B}}). \tag{4.3}$$

Note that the UB shadowing angle is constant since the UB is at a fixed distance from the UE. The RB shadowing angle is a random variable since the distance from the UE is random, and its distribution is derived in Appendix A.

Definition 3. *The event 'AP blocked' = [the AP is blocked by the body] is the intersection of the events [the AP is outside the blockage free zone]* ***and*** *[the body is in between the AP and the UE], i.e.:*

$$\begin{aligned} \mathsf{P}(AP\ blocked) &= \mathsf{P}(AP\ outside \cap\ body\ between) \\ &= \mathbb{1}(d_{\mathrm{A}} > z_{\mathrm{B}} \cap \theta_{\mathrm{B}} < \phi_{\mathrm{B}}). \end{aligned} \tag{4.4}$$

Then, averaging over all the random locations of the body blockages, including the user body, and the distance between the UE and an AP, we define the following for a given pair UE-AP:

Definition 4. *Assuming that one body is enough to cause signal blockage, the event [AP being blocked by a body (UB or RB)] can be expressed as [at least one RB is blocking]* ***or*** *[UB is blocking]. We define the probability p_{A} of this event as:*

$$\begin{aligned} p_{\mathrm{A}} = \mathsf{P}(&at\ least\ one\ random\ body\ is\ blocking \\ &\cup\ user\ body\ is\ blocking). \end{aligned} \tag{4.5}$$

Definition 5. *We define the blockage state as X which can take values from the set $\chi = \{\mathrm{LOS}, \mathrm{NLOS}\}$, where the* NLOS *is given by the event [AP being blocked by a body (UB or RB)], with the* LOS *being the complementary event. Thus, we express X as:*

$$X = \begin{cases} \mathrm{LOS}, & with\ probability \quad 1 - p_{\mathrm{A}}; \\ \mathrm{NLOS}, & with\ probability \quad p_{\mathrm{A}}; \end{cases} \tag{4.6}$$

4.3 Analytical Results

In this section, we provide an analytical expression for the probability of an AP being blocked. We use this expression to reduce the complexity of system-level simulation.[2] In addition, we validate the assumption that blockage events are independent for each AP (no spatial correlation) by showing that the proposed analytical expressions yield results closely trailing numerically evaluated blockage probabilities obtained from our simulation environment.

We compute the blockage of a signal from an AP at a given distance d_{A} from the UE. For that, we need to find the expression that gives the probability p_{A} as a function of the distance. This function depends on two events — the *self-body blockage* and the *random-body blockage* — and on the number of random bodies in the venue. Assuming that the RBs are randomly placed in a square-shaped venue, and the blockage orientation is distributed uniformly, we state the following propositions:

Proposition 1. *The probability of self-body blockage is given by*

$$p_0(d_{\mathrm{A}}) = \begin{cases} \dfrac{\arctan(w_{\mathrm{B}}/_{2r_0})}{\pi}, & d_{\mathrm{A}} \geq r_0 \dfrac{h_{\mathrm{A}}}{h_{\mathrm{B}}}; \\ 0, & 0 < d_{\mathrm{A}} < r_0 \dfrac{h_{\mathrm{A}}}{h_{\mathrm{B}}}; \end{cases} \tag{4.7}$$

Proof: See the proof in Appendix B. ■

Proposition 2. *The probability of blockage by a random body is given by*

$$p_1(d_{\mathrm{A}}) = \int_{\varphi\left(d_{\mathrm{A}}\frac{h_{\mathrm{B}}}{h_{\mathrm{A}}}\right)}^{\pi} \frac{-w_{\mathrm{B}}\ \phi}{2\pi(\cos\phi - 1)} \left(\frac{\pi\rho}{s^2} - \frac{4\rho^2}{s^3} + \frac{\rho^3}{s^4}\right)\ \mathrm{d}\phi, \tag{4.8}$$

where $\varphi(x)$ is the angle of obstruction by the body as a function of a distance x, $\rho = w_{\mathrm{B}}/(2\tan\frac{\phi}{2})$ and s is the square side length.

Proof: See the proof in Appendix C. ■

Proposition 3. *Considering the probabilities in (4.7) and (4.8), and a finite number N_{B} of RBs in the venue, we express the probability of an AP at a distance d_{A} from the UE being blocked by a body (UB or a RB) as*

$$p_{\mathrm{A}}(d_{\mathrm{A}}) = 1 - \big(1 - p_1(d_{\mathrm{A}})\big)^{N_{\mathrm{B}}} \times \big(1 - p_0(d_{\mathrm{A}})\big). \tag{4.9}$$

[2]The simulator would need to compute the inequalities in Definitions 1 and 2 for each AP-body pair, i.e., $n_{\mathrm{A}} \times n_{\mathrm{B}}$ times (number of APs and number of RBs, respectively). With the analytical expression, the simulator only needs to calculate the function in (4.5) for each AP, i.e., n_A times.

Proof: Applying the Definition 4, we can express the probability as:

$$\begin{aligned} p_{\mathrm{A}}(d_{\mathrm{A}}) &= \mathsf{P}(\text{at least one random body is blocking} \\ &\quad \textbf{or } \text{user body is blocking}) \\ &= 1 - \mathsf{P}(\text{no random body is blocking} \\ &\quad \textbf{and } \text{user body is not blocking}) \\ &= 1 - \mathsf{P}(\text{no random body is blocking}) \\ &\quad \times \mathsf{P}(\text{user body is not blocking}) \\ &= 1 - \big(1 - p_1(d_{\mathrm{A}})\big)^{N_{\mathrm{B}}} \times \big(1 - p_0(d_{\mathrm{A}})\big). \end{aligned} \tag{4.10}$$

■

To validate the AP blockage event independence assumption, we compare (4.9) to the outcome of Monte-Carlo simulations for the same setup, where the AP blockage events can be correlated (see Fig. 4.2). We show the results by varying the distance r_0 between UE and UB and the number N_{B} of RBs. We consider a square-shaped venue area of $400 \times 400\,\mathrm{m}^2$ and inter-site distance of 20 m. For the Monte-Carlo simulation, we fix the UE at the origin[3] and we vary the AP position (distance and orientation with respect to the UE). The UB is at a fixed distance from the UE, and its orientation is uniformly distributed. The RBs coordinates are distributed uniformly in both x-axis and y-axis. We observe that the

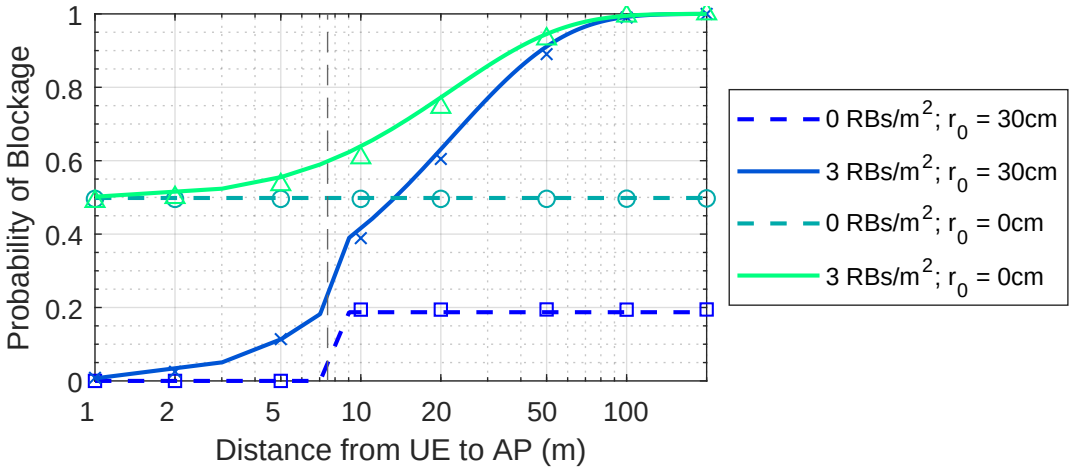

Figure 4.2: Analytical probability of Body Blockage $p_{\mathrm{A}}(d)$ (lines) and relative frequency of blockages in Monte-Carlo simulations (markers). Comparison between different blockage scenarios. The grey vertical dashed line is the radius of the self-body blockage free zone.

expression in (4.9) is a good approximation compared to the relative frequency of blockages computed by simulation. One should note that when the AP is close enough to the UE ($d_{\mathrm{A}} < 5\,\mathrm{m}$) and $r_0 = 30\,\mathrm{cm}$, the probability of blockage is virtually zero, since the AP is inside the self-blockage free zone.

[3]When simulating the UE in other positions (e.g., in a corner and an edge of the square-shaped venue), we found no significant deviation from the results reported for the centre position.

Table 4.3: Simulation Parameters

Area	$400 \times 400\,\mathrm{m}^2$	Side lobe gain s	-10 dB
AP height h_A	10 m	Body width w_B	40 cm
Transmit power p_t	20 dBm	Body height h_B	40 cm
Noise figure	9 dB	Carrier frequency	60 GHz
Bandwidth	2 GHz		

Table 4.4: Channel Parameters (based on [1, Table I])

UE	Path Loss				Shadowing				Small-Scale Fading	
	LOS		NLOS		LOS		NLOS		LOS	NLOS
	ν	ℓ (dB)	ν	ℓ (dB)	α	β	α	β	m	m
Hand	1.72	63.4	1.94	65.3	4.48	0.27	1.18	1.52	3.02	4.68
Pocket	1.70	59.1	0.61	88.5	1.96	0.75	2.80	0.47	4.21	2.46

4.4 Numerical Results

4.4.1 Simulation Setup

We consider the same simulation setup as in 3.3.1, except for the blockage model. The simulation parameters are summarised in Table 4.3. We define two self-body blockage scenarios according to the parameter r_0: $r_0 = 30\,\mathrm{cm}$ represents a scenario of a user operating the UE with the *hand*, e.g. operating an app, and $r_0 = 0\,\mathrm{cm}$ represents a scenario where the UE is held in a *pocket* or as a wearable device. These scenarios are in line with the empirical measurements made in [1]. In addition, we define two random blockage scenarios according to the RB density: $0\,\mathrm{RBs/m}^2$ represents a scenario where there is no other blockage besides the user body (*empty* scenario), and $3\,\mathrm{RBs/m}^2$ represents a *crowded* scenario (such as in a busy transportation hub or a protest march [77]). The combination of these blockage scenarios give us four different scenarios: *empty-hand*, *empty-pocket*, *crowded-hand*, and *crowded-pocket*. We set the channel parameters as measured for a car park environment according to Table 4.4 (based on [1, Table I]). To evaluate the network performance, we consider the following metrics: SINR coverage and area spectral efficiency (ASE). We define the SINR coverage as the probability that the SINR at the UE is larger than the threshold ζ=5 dB, i.e., $\mathsf{P}[\mathrm{SINR} > \zeta]$. While the ASE is the average spectral efficiency, $\mathsf{E}[\log(1 + \mathrm{SINR})]$, divided by the cell area.

4.4.2 Body Blockage Impact

In Chapter 3, we found that there exists a trade-off between ASE and coverage as the same optimal configuration that maximises one metric does not maximise the other. Here, we investigate the impact of body blockage on this trade-off. To that end, we compare the four different blockage scenarios of interest: *empty-hand*, *crowded-hand*, *empty-pocket*, and

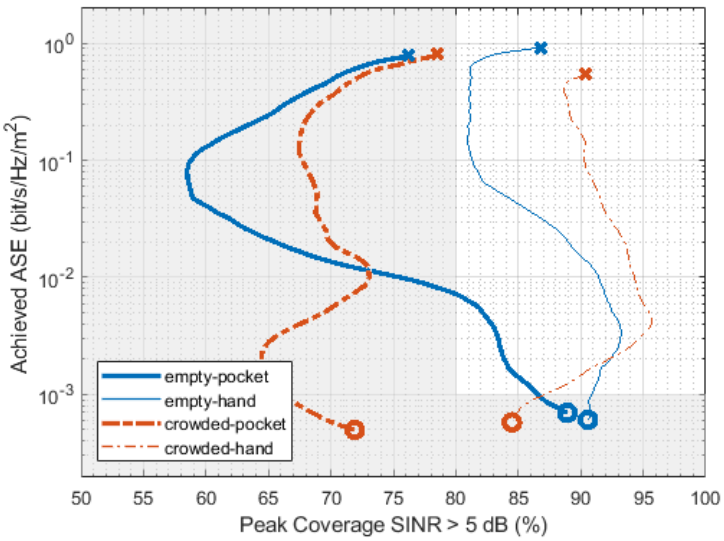

Figure 4.3: Body blockage impact on the ASE-coverage trade-off in the car park environment. Comparison between empty venue (blue solid lines), crowded venue (red dashed lines), UE in pocket (thick lines), and UE in hand (thin lines) scenarios.

crowded-pocket. We depict the trade-off in Fig. 4.3, where the control variable is the inter-site distance δ, and each point of a curve corresponds to the optimal AP/UE beamwidths and AP density configurations that maximise coverage. The circle "$\circ$" marks the achievable ASE-coverage for the lowest AP density (largest δ), while the "$\times$" marks the achievable ASE-coverage for the highest AP density (smallest δ).

In all scenarios, maximum ASE is achieved with the highest AP density, while maximum coverage can be achieved with a lower AP density. Still, we see that coverage in *hand* scenarios (thin lines) are satisfactory in highly-dense AP deployments, but in *pocket* scenarios (thick lines), coverage is deeply degraded. For instance, if considering a coverage of 80 %, deploying high AP density for *pocket* scenario is insufficient. To overcome this threshold, low AP density should be deployed at the expense of two orders of magnitude decrease in ASE.

The optimal AP and UE beamwidths that lead to peak coverage for a given δ are shown in Fig. 4.4. We showed in Section 3.3.2 that minimum AP's main-lobe overlap is necessary to achieve peak coverage, but now, considering a more severe body blockage, a large overlap is needed to allow the UE to be handed-off to a neighbouring AP. *It means that, for the same cell size, a larger AP beamwidth is necessary to achieve peak coverage in pocket scenario (thick lines), than in hand scenario (thin lines), as we observe in Fig. 4.4a.* Yet, the larger an AP beam overlap is needed, the more interference is added, which is why the peak coverage in *pocket* scenarios diminishes (see thick lines in the left side of Fig. 4.4a). *In addition, the UE beamwidth in pocket scenarios are smaller than in hand scenarios as the UE needs to use higher directivity gains to compensate for the increased interference, as*

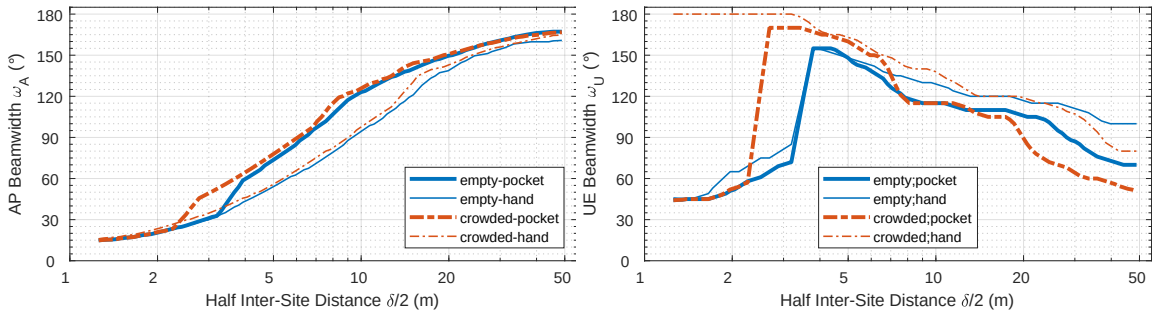

(a) Optimal AP beamwidth.

(b) Optimal UE beamwidth.

Figure 4.4: Body blockage impact on the optimal AP and UE beamwidth in the car park environment. Comparison between empty venue (blue solid lines), crowded venue (red dashed lines), UE in pocket (thick lines), and UE in hand (thin lines) scenarios.

depicted in Fig. 4.4b.

Introducing other randomly distributed bodies, i.e., in *crowded* scenarios (red lines), we observe from Fig. 4.3 that coverage is better than in *empty* scenarios when deploying high AP densities as the random bodies help to block interference. On the other hand, with low AP densities, the random bodies create additional blockages to the serving AP, decreasing SINR.

Comparing the AP beamwidths, we do not observe significant variation between the *crowded* and the *empty* scenarios, as the AP beamwidth is mainly affected by the self-body blockage. Yet, comparing the UE beamwidths, we see that the UE beamwidth in *empty* scenarios (blue lines) are smaller than in *crowded* scenarios (red lines), when high AP density is deployed ($\delta/2 < 10\,\text{m}$ in *pocket* scenarios and $\delta/2 < 20\,\text{m}$ in *hand* scenarios). This is because, differently from the *crowded* scenario, there is no additional blockage to shield from the interference. Thus, the UE needs to have small beamwidths to limit a number of illuminated interfering APs. Furthermore, we see that the optimal UE beamwidth in any scenario is not smaller than $45\,°$. *It means that large beamwidths are, in general, more beneficial than very small beamwidths (i.e., "pencil-beams") in indoor ceiling-mounted AP deployments. This is because small UE beamwidths may still illuminate many APs and increase the interference power with high directivity gains.*

To sum up this section, the ASE-coverage trade-off becomes more significant as coverage degrades with more severe blockage scenarios. It is more difficult in a scenario with high blockage probability (*pocket* scenarios) to achieve a certain level of coverage without significantly degrading the ASE, compared to a scenario with low blockage probability (*hand* scenarios). For instance, for a requirement of ASE $> 10^{-3}\,\text{bit/s/Hz/m}^2$ and coverage $> 80\,\%$, the system configuration for *pocket* scenarios is restricted to a range of half inter-site distances

between 20 and 30 m if the venue is *empty*[4]. For *hand* scenarios, the goal can be achieved with any half inter-site distance $\delta/2 < 30\,\mathrm{m}$. Moreover, the optimal system configuration should be set depending on the blockage scenario, as the same configuration for one scenario may not be optimal for the others. For instance, to achieve ASE $> 10^{-1}\,\mathrm{bit/s/Hz/m^2}$, cell size and AP beamwidth should be set small (e.g., $\delta/2 < 3\,\mathrm{m}$, $\omega_\mathrm{A} = 30\,^\circ$) for all scenarios, but the optimal UE beamwidth should be large for *hand* scenarios (e.g., $\omega_\mathrm{U} = 180\,^\circ$) and small for *pocket* scenarios (e.g., $\omega_\mathrm{U} = 45\,^\circ$).

4.5 Conclusion

On top of the study conducted in Chapter 3, we investigated the impact of body blockage on the network design aspects of ceiling-mounted mmWave AP deployments with directional antennas over a confined area. We showed that the optimal AP/UE main-lobe beamwidths configuration takes different values depending on the severity of the blockage scenario. In the main, large AP beamwidths create enough overlap to allow for hand-offs that will mitigate the blockage effects while keeping interference at an acceptable level. Moreover, the optimal UE beamwidth is adjusted to compensate for the variation on interference, shadowing or path loss.

Finally, we demonstrated the need for considering the blockage scenario to design the network deployment, as the same configuration for one scenario may not be optimal for the others. This implies that fixed system configurations in a dynamic blockage environment may lead to inefficiency of the usage of network resources if they are not allocated carefully. In the following chapters, we investigate the use of flexible resource allocation by the system and how the network can benefit from it.

[4]When the venue is *crowded*, it is impossible to meet these design criteria.

5 Application of Flexible Frame Structure to Blockage Mitigation

Application of Flexible Frame Structure to Blockage Mitigation

The 5G new radio (NR) standard for wireless communications supports the millimetre-wave (mmWave) spectrum to yield unprecedented improvement of the access network capacity. However, intermittent blockages in the mmWave signal may degrade the system performance and lead to the under-utilisation of the allocated resources. To circumvent this problem, the transmission time shall be adjusted according to the blockage condition, avoiding the resource under-utilisation. In this chapter, we propose that the 5G NR flexible numerology and slot aggregation should be applied to adapt the transmission time in order to mitigate the blockage effects. We validate this claim by analysing the expected data rate of a mmWave system, under a range of blockage scenarios. We show that different blockage scenarios may require different numerologies to produce best performance, and that the correct choice of numerology and aggregation may improve this performance by as much as hundreds of Mbps. Our results carry important insights for the design of blockage-aware scheduling mechanisms for 5G.

5.1 Blockage Mitigation

Blockages in mmWave signal propagation are related to severe attenuation of the signal power (in certain cases, the blockage may add as much as 40 dB of attenuation [78]), which can lead to radio link failures and consequent disconnection in the communication. In the literature to date, this issue has been addressed mostly by proposing deployment strategies that allow the network to exploit spatial macro-diversity, i.e., increasing the communication robustness by enabling the user to receive the signal from distinct points in space. These deployment strategies include: reflective surfaces [79], relay nodes [80], dense networks [26], ceiling-mounted access points (APs) [81], and movable APs [82] that can position themselves in a way that increases the likelihood of having an AP operating in line-of-sight (LOS). Then, in order to unlock the benefits of spatial macro-diversity, dedicated medium access control (MAC) layer mechanisms should coordinate network nodes and allocate time-frequency transmission resources accordingly. Yet – as we show in our numerical results – if a fixed transmission time interval (TTI) is considered for this allocation, the intermittency

of blockage events may cause system performance degradation and, effectively, resource under-utilisation.

5.2 Application of Flexible Frame Structure

In this chapter, we consider adaptable transmission times for blockage mitigation, using the flexible TTI (slot duration) and slot aggregation proposed for the 5G NR. The ability of the TTI adjustment is enabled by the 5G NR access technology. It works with a flexible orthogonal frequency-division multiplexing (OFDM) transmission frame system, in which the configuration of the TTI, i.e., sub-carrier spacing (SCS) and cyclic prefix (CP), is flexible, as illustrated in Figure 5.1. According to the 5G terminology [83], such configuration is referred to as the *flexible numerology* and the supported numerologies are listed in Table 5.1. In addition, 5G NR frame structure supports slot aggregation. Slot aggregation refers to the case when a transmission can span two or more slots in order to achieve improved coverage and/or reduced overhead.

Originally, flexible numerology was introduced to enable service-level differentiation, i.e., network slicing, for 5G use cases [5]. In the state of the art, flexible numerology has been applied to improve the network latency where the TTI is optimised according to a latency deadline and overhead restrictions [15]. In [16], it has been shown that the choice of numerology to improve latency highly depends on the traffic pattern and processing/decoding delays. The reason is that increasing numerology may also increase the overhead associated to the traffic arrival rate. Also, flexible numerology has been applied to improve the frame spectral efficiency when multiplexing different types of services, e.g., enhanced mobile broadband (eMBB) and ultra-reliable low-latency communication (URLLC) [84, 85]. Our work is the first to apply flexible numerology to mitigate the negative effects of blockages in mmWaves.

In this chapter, we propose an alternative application of the flexible numerology. We

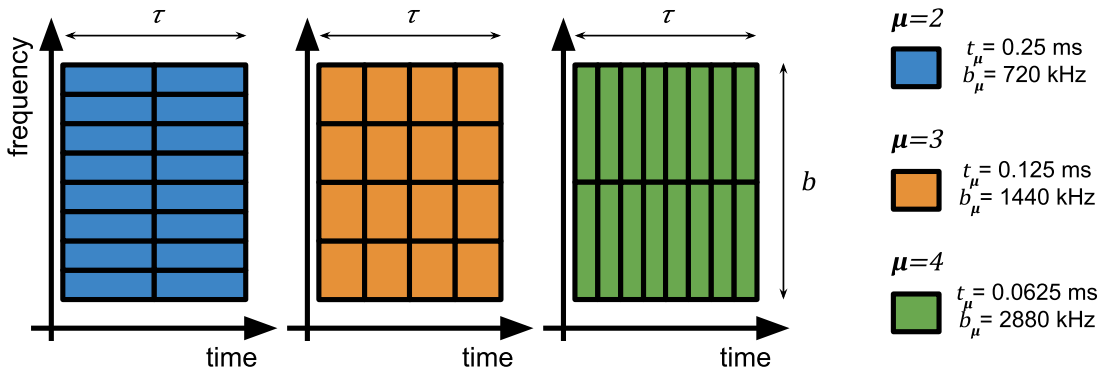

Figure 5.1: Demonstrative application of different numerologies in a 5G frame. The resource blocks are allocated for τ ms and within a bandwidth b kHz. Each numerology gives a resource block with slot duration t_μ ms and block bandwidth b_μ kHz.

Table 5.1: Resource Block Numerology Configuration

μ	TTI [ms] $2^{-\mu}$	CP length [us] $4.69/2^{\mu}$	Bandwidth [kHz] $2^{\mu} \cdot 15 \cdot 12$
0	1	4.690	180
1	0.5	2.345	360
2*	0.25	1.172	720
2**	0.25	4.167	720
3*	0.125	0.586	1440
4*	0.0625	0.293	2880

* 5G NR Rel-15 in sub-6 GHz bands can only use $\mu \leq 2$ numerology, while in mmWave bands, only $\mu > 2$ [86].

** Extended CP

propose that flexible numerologies be used according to the blockage conditions, to improve the mmWave user performance. We verify our claim by analysing the mmWave link performance using numerologies available for 5G mmWave systems, under a range of blockage scenarios, defined and empirically-validated in [2]. Our results show that there is a trade-off between the high transmission efficiency, achieved with longer TTIs, and the high probability of LOS transmission, achieved using shorter TTIs. In consequence, the same numerology used for two different blockage scenarios (office and car-park) leads to opposing conclusions about the system performance. In fact, the correct choice of numerology may improve performance by as much as hundreds of Mbps. Effectively, we identify conditions under which it may be favourable to use a given numerology, providing important insights for the design of blockage-aware scheduling mechanisms for 5G.

The rest of the chapter is organised as follows. In Section 5.3, we describe our system model. In Section 5.4, we describe our performance metric. In Section 5.5 we analyse the link performance, comparing the numerologies and the blockage conditions. We draw our conclusions in Section 5.6.

5.3 System Model

We consider a single cell, with an AP installed on the ceiling or a lamppost, transmitting a 5G OFDM frame to a user equipment (UE) at a distance d_{A} in the horizontal plane. The AP is installed at a height h_{A} above the UE level, as illustrated in Figure 4.1a. This setup emulates the two deployment scenarios considered in [2]: indoor office with ceiling-mounted access points and outdoor car-park with lamppost mounted access points. Yet, it is also in line with the 3GPP-defined scenarios for 5G mmWave system evaluation [87].

We assume the resource allocation decision in the AP is made every τ ms, which we refer to as the *scheduling interval (SI)*. For ease of exposure, we consider the link performance as experienced by a single user, attached to a single cell. The cell's bandwidth is b, where

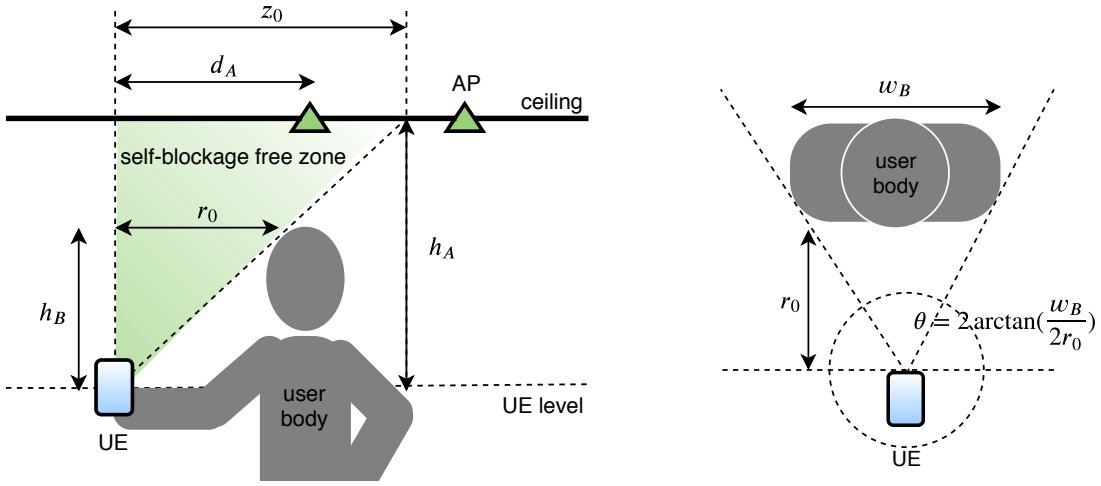

(a) Side view

(b) Top view.

Figure 5.2: Obstruction by a body may happen when the AP is beyond the radius z_0. On the other hand, an AP within this radius is not obstructed, regardless the body orientation with respect to the UE, i.e., the AP is inside the *self-blockage free zone* represented by the green area

flexible numerology μ is associated with resource blocks of bandwidth b_μ and TTI t_μ, as illustrated in Figure 5.1.

5.3.1 Blockage Probability Model

Whether the LOS path to the UE is blocked during a slot within the SI depends on the blockage probability. We define the blockage probability as the probability of a slot being blocked during a given interval. This probability is given by the probability of self-body blockage as in Section 3.2.2:

$$p = \begin{cases} \frac{1}{\pi} \arctan\left(\frac{w_\mathrm{B}}{2r_\mathrm{B}}\right), \; d_\mathrm{A} \geq z_\mathrm{B}; \\ 0, \; \text{otherwise}; \end{cases} \tag{5.1}$$

where w_B is the body width, r_B is the distance between the body and the UE, and h_B is the distance between the UE level and the top of the body, and $z_\mathrm{B} = r_\mathrm{B}\frac{h_\mathrm{A}}{h_\mathrm{B}}$ is the self-body blockage free zone radius, as illustrated in Figure 5.2.

5.3.2 Signal-to-Noise Ratio

To model the mmWave signal propagation, we consider the experimentally-validated channel model proposed in [2]. The model consists of the path loss, large-scale Gamma fading, and multipath Nakagami-m fading, whose parameters take one of two values depending on whether the user body blocks the LOS path or not, meaning that the model parameters change with the random blockage state. The fading and path-loss coefficients for that model

were estimated from the experimental data collected for a mmWave AP operating at 60 GHz in [2].

We define the set of the two possible blockage states as $\chi = \{\text{LOS}, \text{NLOS}\}$. Hence, given the blockage state $X = x \in \chi$, we can define the path loss as $l_x = \ell_x \cdot \left(\sqrt{d_{\text{A}}^2 + h_{\text{A}}^2}\right)^{-\nu_x}$, where $\sqrt{d_{\text{A}}^2 + h_{\text{A}}^2}$ is the Euclidean distance from the AP to the UE, ℓ_x is the path loss at one metre distance under free space propagation, and ν_x is the attenuation exponent. Thus, we define the signal-to-noise ratio (SNR) Y, conditioned on $X = x$, as:

$$Y_x = \frac{\rho}{\sigma} l_x H_x, \tag{5.2}$$

where ρ is the transmit power, σ is the noise power, and H_x is the fading gain.

We consider the fading gain as a single random variable H_x, instead of treating each fading component individually, with a composite fading distribution, as obtained in [88]. This approach allows us to define the complementary cumulative distribution function (ccdf) of the SNR Y in (5.2) based on the formula in [88, (15)] as follows:

$$F_{Y|X}^{c}(y;\, \bar{y}_x, m_x, \alpha_x, \beta_x) = \mathsf{A}\Gamma(m_x) \sum_{i=0}^{m_x} \frac{2^i y^{m_x - i}}{(\mathsf{BD})^i (m_x - i)!} \frac{\mathcal{K}_{m_x - i + \frac{1}{2}}(\mathsf{B}\sqrt{\mathsf{C} + \mathsf{D}y})}{(\mathsf{B}\sqrt{\mathsf{C} + \mathsf{D}y})^{m_x - i + \frac{1}{2}}} \tag{5.3}$$

where $\bar{y}_x = \frac{\rho}{\sigma} l_x$ is the SNR without the fading component, the variable m_x is the Nakagami-m fading parameter, (α_x, β_x) are the Gamma shadowing parameters, $\mathcal{K}_o(\cdot)$ is the modified Bessel function of the second kind of order o, and the used constants are:

$$\begin{aligned}
\mathsf{A} &= \frac{(\alpha_x \bar{y}_x)^{\frac{1+2m_x}{4}}}{\Gamma(m_x)} \sqrt{\frac{2\alpha_x \beta_x}{\pi}} \exp(\alpha_x \beta_x) \left(\frac{m_x}{\bar{y}_x}\right)^{m_x}, \\
\mathsf{B} &= \beta_x \sqrt{\frac{\alpha_x}{\bar{y}_x}}, \\
\mathsf{C} &= \alpha_x \bar{y}_x, \\
\mathsf{D} &= 2m_x / \beta_x,
\end{aligned} \tag{5.4}$$

where $\Gamma(\cdot)$ is the Gamma function.

5.3.3 Transmission Efficiency and Slot Aggregation Efficiency

We define the transmission efficiency $\eta_\mu \in [0, 1]$ of a resource block of type μ. It represents a loss factor in spectral efficiency for shorter TTIs due to inter-symbol interference caused by shorter CP [89]. Thus, the longer the TTI (longer CP), the greater the transmission efficiency, i.e., $\eta_i > \eta_j$ for all $i > j$.

We also define the slot aggregation efficiency $\zeta_\mu \in [0, 1]$ as the ratio between the number of symbols that are used for data transmission and the total number of symbols.

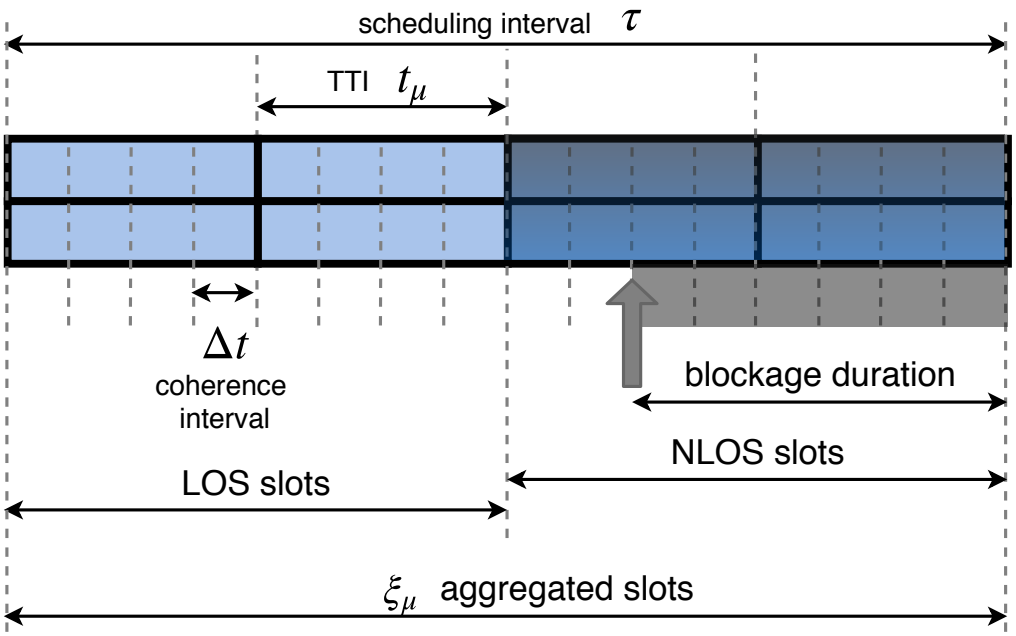

Figure 5.3: The SI τ contains a sequence of slots with duration t_μ. The TTI is a multiple of the blockage "coherence" interval Δt. When a blockage occurs during one Δt interval within a slot, the entire slot and the following ones are considered non-line-of-sight (NLOS), as the blockage duration is expected to be significantly longer than the SI.

5.4 Performance Analysis

We evaluate the performance of our system in terms of the expected data rate. To calculate it, we consider the probability of blockage, the spectral efficiency of the channel, the transmission efficiency of each resource block, and the slot aggregation efficiency. We consider that the TTI t_μ is a multiple of Δt (see Figure 5.3), which is the blockage "coherence" interval. Within this interval, the blockage event has probability p as described in (5.1) and is independent of the previous interval, but once the first blockage event happens, we assume that all the following slots within the SI τ are also blocked[1]. Consequently, a slot, that contains k coherence intervals ($t_\mu = k \cdot \Delta t$), is transmitted in LOS if no blockage has occurred in previous slots and in each of its own coherence intervals. Thus, the probability of the i-th slot being in LOS is:

$$\mathbb{P}[X_i = \text{LOS}] = (1-p)^{k \cdot i} = (1-p)^{i \frac{t_\mu}{\Delta t}}. \tag{5.5}$$

The spectral efficiency S can be expressed as $S = \log(1+Y)$, and has only non-negative values. Hence, the expected value conditioned to the blockage state of the i-th slot can be

[1]For 5G NR it has been shown in [55] that the body blockage duration can be in the order of 100 ms (due to low mobility of pedestrians) versus the 10 ms duration of a frame.

represented by this integral which can be efficiently computed numerically:

$$\mathbb{E}[S_{x_i}|X_i = x_i] = \int_0^\infty F^c_{Y|X}(2^s - 1;\ \bar{y}_x, m_x, \alpha_x, \beta_x)\,\mathrm{d}s, \tag{5.6}$$

where $F^c_{Y|X}(\cdot)$ is ccdf of the SNR defined in (5.3). Thus, the expected spectral efficiency with respect to the blockage state of the i-th slot is:

$$\begin{aligned}\mathbb{E}_{X_i,S}\left[S_{X_i}\right] &= \sum_{x_i \in \chi} \mathbb{P}[X_i = x_i]\mathbb{E}[S_{x_i}|X_i = x_i] \\ &\overset{(a)}{=} (1-p)^{i\frac{t_\mu}{\Delta t}} \cdot \mathbb{E}[S_{\mathrm{LOS}}|X = \textsc{los}] \\ &\quad + \left(1 - (1-p)^{i\frac{t_\mu}{\Delta t}}\right) \cdot \mathbb{E}[S_{\mathrm{NLOS}}|X = \textsc{nlos}],\end{aligned} \tag{5.7}$$

where (a) comes from using (5.1) and from the fact that the channel is constant under the same blockage state.

Finally, the expected data rate $\bar{R}_\mu$, using the numerology μ, of a slot aggregation across ξ_μ slots is given as the expectation over the sum of the spectral efficiencies for each slot, multiplied by the frame bandwidth and the transmission and slot aggregation efficiencies:

$$\bar{R}_\mu = b \cdot \zeta_\mu \cdot \eta_\mu \cdot \mathbb{E}_{X,S}\left[\sum_{i=1}^{\xi_\mu} S_{X_i}\right]. \tag{5.8}$$

Then, using (5.5) and (5.7), $\bar{R}_\mu$ can be expressed as in (5.9).

$$\begin{aligned}\bar{R}_\mu &= b\,\zeta_\mu\,\eta_\mu \sum_{i=1}^{\xi_\mu} \mathbb{E}_{X,S}\left[S_{X_i}\right] \\ &= b\,\zeta_\mu\,\eta_\mu \sum_{i=1}^{\xi_\mu} \left(\mathbb{P}[X_i = \textsc{los}]\,\mathbb{E}[S_{\mathrm{LOS}}|X = \textsc{los}] + \mathbb{P}[X_i = \textsc{nlos}]\,\mathbb{E}[S_{\mathrm{NLOS}}|X = \textsc{nlos}]\right) \\ &= b\,\zeta_\mu\,\eta_\mu \Big(\xi_\mu\,\mathbb{E}[S_{\mathrm{NLOS}}|X = \textsc{nlos}] \\ &\quad + \frac{(1-p)^{\frac{t_\mu}{\Delta t}}\left((1-p)^{\xi_\mu\frac{t_\mu}{\Delta t}} - 1\right)}{(1-p)^{\frac{t_\mu}{\Delta t}} - 1}\left(\mathbb{E}[S_{\mathrm{LOS}}|X = \textsc{los}] - \mathbb{E}[S_{\mathrm{NLOS}}|X = \textsc{nlos}]\right)\Big)\end{aligned} \tag{5.9}$$

We observe that, in the final expression in (5.9), the expected data rate is proportional to the transmission and slot aggregation efficiencies, and the blockage probability p limits the contribution of the expected spectral efficiency in LOS on the data rate.

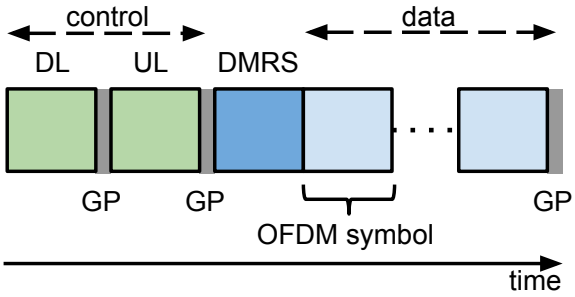

Figure 5.4: The slot structure. The first and second symbols are reserved for downlink and uplink control, third symbol is used for demodulation of the reference signal. Guard periods are placed between downlink/uplink control symbols and between uplink control and DMRS symbols.

5.5 Numerical Results

In this section, we show the benefits of the application of flexible numerology to blockage mitigation in 5G NR mmWave systems. We compare the results for three types of resource blocks supported by mmWave NR (i.e., $\mu = 2, 3, 4$ according to 5G NR Rel-15 [83]), under different blockage scenarios. Here, we only consider numerologies with normal CP.

We consider two blockage scenarios: a UE held in the pocket ($r_{\mathrm{B}} = 0\,\mathrm{cm}$, *UE in pocket*), and a UE operated with the hand ($r_{\mathrm{B}} = 30\,\mathrm{cm}$, *UE in hand*). The *UE in pocket* scenario is a severe blockage condition where the body is obstructing half of the "angle-of-view", thus the probability of blockage is $p = 0.5$. The *UE in hand* scenario is a common blockage condition where the user is, for example, operating an app and the body obstructs a smaller angle than in the *UE in pocket* scenario. We consider two environments: an indoor open *office* and an outdoor *car park*. This setup reflects the scenarios and environments empirically characterised in [2]. Corresponding channel coefficients are listed on Tables 5.2 and 5.3.

We assume that the transmission efficiency η_μ decreases by 5% with each increment in the numerology μ (i.e., $\eta_2 = 1.00$, $\eta_3 = 0.95$ and $\eta_4 = 0.90$), as observed in [90] that the difference in spectral efficiency is about 5-6 % from one numerology to the other. Accurate values for the numerology-dependent transmission efficiency can be obtained following the calculations presented in [89]. We assume that the slot structure is as described in [91], where each slot consists of 14 symbols as illustrated in Figure 5.4. In a slot aggregation of $\xi_\mu = \tau/t_\mu$ slots, the two first symbols are used for downlink and uplink control, the third is used for demodulation of the reference signal, and the rest of the symbols is for data. Hence, this slot structure gives an control overhead of 3 symbols out of an aggregation of $14\tau/t_\mu$ symbols. Thus, the slot aggregation efficiency is $\zeta_\mu = 1 - \frac{3t_\mu}{14\tau}$, decreasing with the numerology μ and increasing with the SI τ. We set the frame bandwidth as 100 MHz [83] and we evaluate the performance with the SI $\tau = 1\,\mathrm{ms}$ (unless specified otherwise), as in the legacy LTE scheduling. For our analysis, we set $\Delta t = 0.0625\,\mathrm{ms}$ as the shortest TTI among the numerologies considered. All other fixed system parameters are shown in Table 5.4.

Table 5.2: Path Loss Model Parameters (based on [2, Table I])

Environment	Path Loss			
	LOS		NLOS	
	ν	ℓ (dB)	ν	ℓ (dB)
Office	1.18	45.1	1.07	57.4
Car Park	1.53	48.7	1.98	88.8

Table 5.3: Fading Model Parameters (based on [2, Table I])

Environment	Shadowing				Small-Scale Fading	
	LOS		NLOS		LOS	NLOS
	α	β	α	β	m	m
Office	7.01	0.15	5.77	0.20	2.64	2.35
Car Park	10.30	0.11	5.11	0.23	8.50	2.74

Table 5.4: System Model Parameters

Transmit Power	ρ	20 dBm
Noise Density	σ/b	-174 dBm/Hz
Body Width	w_{B}	40 cm
Body Height*	h_{B}	40 cm
AP Height*	h_{A}	5 m

* with respect to the UE level

5.5.1 Environment and Blockage Impact

In this subsection, we evaluate the impact of two environments (an *office* and a *car park*), with distinct channel characteristics, and two blockage scenarios (*UE in hand* and *UE in pocket*) on the expected data rate of mmWave communication. We also compare the scenarios where the UE is close to the AP ($d_{\mathrm{A}} = 1\,\mathrm{m}$) and where the UE is far from the AP ($d_{\mathrm{A}} = 10\,\mathrm{m}$). The results are shown in Figure 5.5.

From the left side of Figure 5.5a, we see that the expected data rate is higher when using a TTI of $t_2 = 0.25\,\mathrm{ms}$ (blue bar), compared to other TTIs, for a user close to the AP and operating the UE with the hand. In this case, the blockage probability is very low, allowing for high transmission efficiency of the resource block with long slot duration to have a more significant impact on the data rate than the blockage. On the right-hand side of that same figure, we observe a decrease in the expected data rate because of the dual-effect of increased path loss and blockage probability for a user further away from the AP. The *car park* environment suffers more from blockages compared to the *office* environment as there is less power in the NLOS signal, likely due to lack of reflecting/scattering environment. Thus, short TTI ($t_4 = 0.0625\,\mathrm{ms}$, green bar) mitigates the blockage effects by increasing the expected number of slots in LOS and yields better performance in the *car park* environment.

From Figure 5.5b, we note that the expected data rate has similar trends when we vary

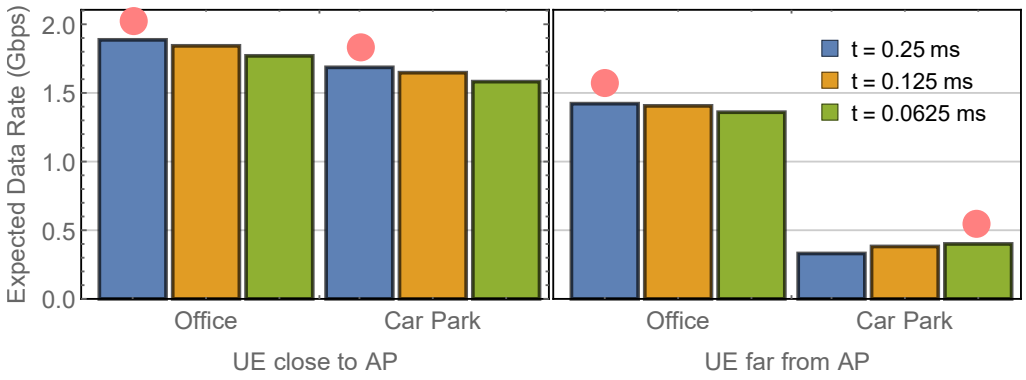

(a) *UE in hand* scenario.

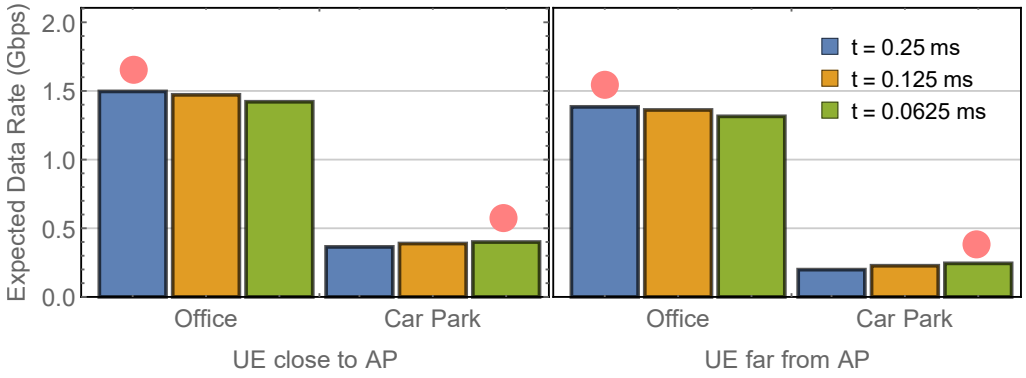

(b) *UE in pocket* scenario.

Figure 5.5: Expected data rate using different TTIs with SI $\tau = 1$ ms, in two environments (*office* and *car park*), at two distances between the UE and AP (1 m and 10 m), and in two blockage scenarios (*UE in hand* and *UE in pocket*). The pink disks indicate the recommended numerology for scheduling in the given scenario.

the distance between the UE and the AP, as the considered range of distances have little effect on the blockage probability for the UE in the pocket. We see that the user in the *office* environment achieves highest expected data rate using TTI $t_2 = 0.25$ ms, and in the *car park* environment, the user achieves highest expected data rate using TTI $t_4 = 0.0625$ ms in both cases (UE close to AP and far from AP) of the *UE in pocket* scenario.

5.5.2 Scheduling Interval Impact

In LTE networks, the scheduler makes the allocation decision every TTI, which has a fixed duration of 1 ms, and the decision is valid until the next TTI [92]. The 5G NR allows for slot aggregation, in which the aggregation duration can span two or more slots to reduce the control overhead. Hence, the scheduling decision interval is no longer fixed and can vary with the slot aggregation size. Here, we evaluate the impact of the aggregation overhead reduction by comparing the SIs: $\tau = 0.25$ ms (short SI)[2] and $\tau = 5$ ms (long SI)[3]. The results considering the *car park* environment are shown in Figure 5.6.

[2] An SI of $\tau = 0.25$ ms allows us to allocate at least one longest TTI ($t_4 = 0.25$ ms).
[3] We observed that the usage of any SI between 5 and 10 ms leads to negligible differences in results.

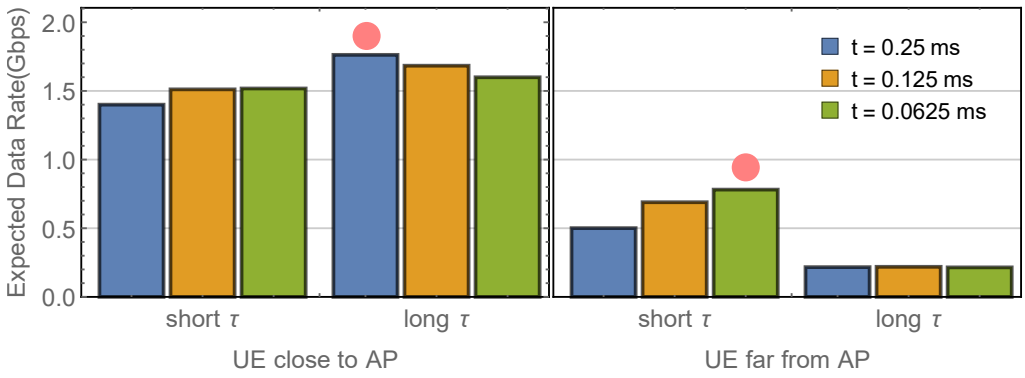

(a) *UE in hand* scenario.

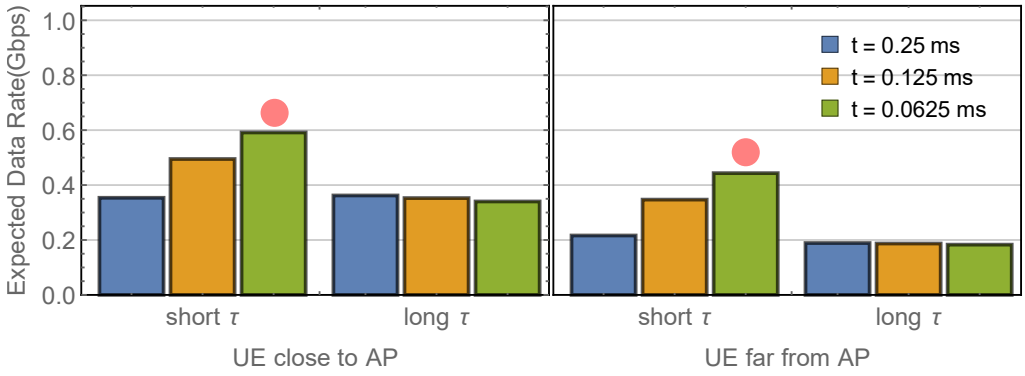

(b) *UE in pocket* scenario.

Figure 5.6: Expected data rate using different TTIs, with two SIs ($\tau = 0.25$ ms, $\tau = 5$ ms), in the *car park* environment, at two distances between the UE and AP (1 m and 10 m), and in two blockage scenarios (*UE in hand* and *UE in pocket*). The pink disks indicates the recommended numerology for scheduling in the given scenario.

From Figure 5.6, we observe that, in most cases, a short SI achieves better performance with short TTI (green bar) compared to long TTI (blue bar). The only exception, as we see from the left side of Figure 5.6a, is the scenario of a user close to the AP operating the UE with the hand. In this scenario, the best performance is achieved by long SI with long TTI. This is because the effects of increased transmission efficiency (long TTI) and reduced overhead (long SI) have a higher impact on the expected data rate than the blockage probability. In other cases, i.e., UE far from AP in *UE in hand* scenario and both UE far and close to AP in *UE in pocket* scenario (see Figure 5.6b), the blockage probability is high and has more impact on the expected data rate than the overhead reduction. Thus, there is no benefit in increasing the SI in those cases.

To sum up, the appropriate combination of numerology and scheduling interval is essential to achieve the best performance. For example, in the cases where the blockage has more significant impact on the expected data rate (e.g., UE far from AP or UE in pocket), the use of short SI with short TTI is recommended to avoid prolonged exposure to blockage interruptions. On the other hand, in the cases where the blockage has less impact (e.g., UE close to AP), the use of long SI with long TTI is recommended to take advantage of the

Table 5.5: Recommended Numerology μ and Scheduling Interval τ (in ms)

Environment	Office		Car Park	
	UE close to AP	UE far from AP	UE close to AP	UE far from AP
UE in hand	$\mu = 2$ $\tau = 5$	$\mu = 2$ $\tau = 5$	$\mu = 2$ $\tau = 5$	$\mu = 4$ $\tau = 0.25$
UE in pocket	$\mu = 2$ $\tau = 5$	$\mu = 2$ $\tau = 5$	$\mu = 4$ $\tau = 0.25$	$\mu = 4$ $\tau = 0.25$

reduced overhead and the high transmission efficiency.

5.6 Conclusion

In this chapter, we proposed that 5G NR flexible frame structure be used to mitigate the negative effects of body blockage in 5G mmWave systems. We presented an analytical framework that allowed us to show and understand the benefits of our proposed application of flexible frame structure. We showed that different blockage conditions require different combinations of numerology and slot aggregation to achieve the best performance, as presented in Table 5.5. The effectiveness of flexible frame structure in mmWave blockage scenarios is a consequence of the trade-off between the high transmission efficiency, achieved with long TTIs and long SIs, and the high probability of LOS transmission, achieved using short TTIs and short SIs.

The gains on data rate due to varying the TTIs are not as significant as the gains due to changing the SIs. This suggests that the mmWave link performance under blockage scenarios is more sensitive to longer time resolutions (in the order of milliseconds) than to shorter time resolutions (microseconds), as the blockage state does not change as fast as one slot duration. Therefore, we decided to continue exploring the aspects of the SI duration in the following chapter. We will investigate what the implications of the body blockage attenuation on the scheduling algorithms are. We shall see that to allow for shorter or longer SIs, the scheduler requires prior information about the channel to allocate the slots efficiently in a frame shared with multiple users.

6 Performance Evaluation of Scheduling in 5G-mmWave Networks under Human Blockage

Performance Evaluation of Scheduling in 5G-mmWave Networks under Human Blockage

The millimetre-wave spectrum provisions enormous enhancement to the achievable data rate of 5G networks. However, human blockages in the millimetre-wave signal can severely degrade the performance if proper resource allocation is not considered. In this chapter, we assess how conventional schedulers, such as the Proportional Fair scheduler, react to the presence of blockage. Our results show that the resource allocation may disfavour users suffering from blockage, leading to low data rate for those users. To circumvent this problem, we show that the data rate of those users can be improved by using a scheduler adapted to be aware of upcoming blockage events. The adapted scheduler aims at proactively allocating the resources before a blockage happens, mitigating losses. Such adaptation is motivated by recent progress in blockage prediction for millimetre-wave signals with a dynamic human blockage scenario. Our extensive simulations indicate that our modified scheduler improves the data rate of users affected by blockages by up to 65 % compared to traditional schedulers.

6.1 Resource Allocation under Human Blockage

Human blockages in millimetre-wave (mmWave) signal can be frequent in crowded places such as transportation hubs and sport arenas. This frequent, and potentially abrupt, disruption to the signal quality requires quick reaction by the system to maintain high data rates of communication. One significant way to cope with disruptions towards these dynamic blockages is to use spatial macro-diversity [93]. Spatial macro-diversity allows a user equipment (UE) to be connected with access points (APs) installed in different locations. When the UE is disconnected (for example, due to blockage), it can re-connect to another AP. However, the process of re-connecting requires extra time during which the blocked UE may be unable to be allocated transmission resources. Thus, a UE suffering from frequent blockage can have its transmission rate severely reduced, increasing the discrepancy with respect to other UEs in favourable channel conditions, as we will also show in our numerical evaluation.

In this chapter, we evaluate the performance of resource allocation algorithms, based on the conventional Proportional Fair (PF) scheduler, in the presence of mmWave signal blockages. We consider that the resource allocation is performed to multiple users each of which may experience abrupt disruptions to signal quality caused by the human body blockage. Since the PF scheduler prioritises the allocation based on the achievable transmission rate, UEs suffering from blockage may have the achievable rate degraded and thus have progressively less priority, disfavouring the allocation to those UEs. To circumvent this, the scheduler can be adapted by considering blockage prediction to effectively mitigate the blockage effects, as we will show in this work.

6.1.1 Scheduling with Blockage Prediction

Blockage prediction in mmWave communications can be performed by: (i) inferring the mmWave channel from the sub-6 GHz channel observation [68, 71], (ii) observing the past mmWave beamforming vectors [67, 94] or (iii) using camera images to track the movement of potential obstructions [69, 95]. Those methods can produce blockage indicators that will help the system to predict the channel status in the future. The blockage indicator allows the scheduler to have sufficient time to allocate resources in order to mitigate the losses in performance caused by the transition from line-of-sight (LOS) to blocked state. Moreover, such scheduling design may provide the system with an alternative way to mitigate blockage effects when there is no other cell to hand-off. Hence, we assume there exists a prediction mechanism, such as in [71], that allows the system to predict the blockage state in a given time window and to estimate the channel gain and data rates based on that prediction. With this system, we can implement a scheduler that allocates resources in future transmission intervals according to the estimated data rates and test its performance against the conventional schedulers. To the best of our knowledge, we are the first to evaluate the performance of schedulers under blockage scenario in mmWave networks.

In our analysis, we show that users suffering from blockage are disfavoured in the resource allocation because conventional schedulers do not react quickly enough to the event of an abrupt signal disruption. This result shows that conventional schedulers, to be applied in 5G networks, should be adapted to cope with the impairments of the mmWave propagation. We show that an adaptation of the PF scheduler can be made by changing the priority metric to consider the blockage prediction. We refer to this adapted scheduler as the Blockage-Aware Predictive Proportional Fair (BA-PF) scheduler. We also show that using BA-PF it is possible to increase bandwidth allocation before the channel quality drops and reduce it thereafter, as illustrated in Figure 6.1. Our results show that the BA-PF scheduler outperforms all tested schedulers in blockage loss reduction, improving the data rate of a UE suffering from blockage by up to 65 %.

In what follows, we describe our system model in Section 6.2. We evaluate the user data rate performance, comparing the BA-PF scheduler to conventional schedulers in Section 6.3.

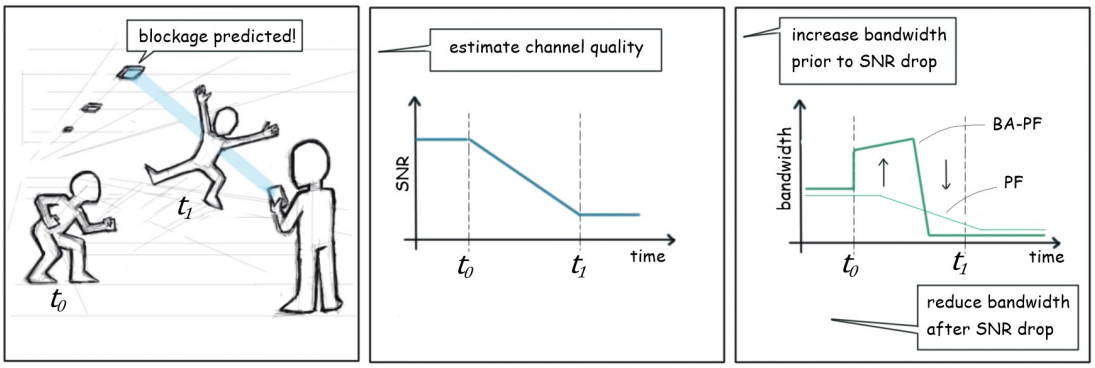

Figure 6.1: At time t_0, a blockage is predicted to occur at time t_1. The system estimates the channel quality between times t_0 and t_1. Based on this estimation, the BA-PF scheduler proactively allocates resources before the blockage event, while the conventional Proportional Fair scheduler can only react to blockage.

Then, we summarise our findings in Section 6.4.

6.2 System Model

6.2.1 Frame Structure

We study the downlink transmission of a single ceiling-mounted indoor mmWave AP concurrently transmitting to multiple UEs using orthogonal frequency-division multiple access (OFDMA). According to the 5G new radio (NR) standard [83], in the time-domain data transmission occurs in time-slots with duration Δ_t, while in the frequency domain, the total bandwidth b is divided into orthogonal sub-carriers of width b_{SC}. These are grouped into n_{C} sub-channels of width $\Delta_b = 12\, b_{\mathrm{SC}}$, providing a total of $n_{\mathrm{C}} = \lfloor b/(12\, b_{\mathrm{SC}}) \rfloor$ different sub-channels. We consider the random body (RB) as the basic time-frequency allocation unit corresponding to the single sub-channel $k \in \{1, \ldots, n_{\mathrm{C}}\}$ in the time-slot t. The set of n_U UEs shares the total bandwidth b and, at the medium access control (MAC) layer, a scheduler assigns an RB in time-slot t and sub-channel k to a UE $u \in \{1, \ldots, n_U\}$. This assignment is represented by a matrix $\mathbf{X}$ for each UE. When the RB (k, t) is assigned to UE u, the scheduler sets $x_u(k, t) = 1$. Otherwise, the scheduler sets $x_u(k, t) = 0$. Since only one user is scheduled per RB, $\mathbf{X}$ is constrained by $\sum_{u=1}^{n_U} x_u(k, t) = 1,\ \forall\ (k, t)$.

6.2.2 Channel Model

The LOS path between AP and UE can be obstructed by blockage, such as a moving pedestrian, which can decrease the received signal power. We assume the blockage event is independent among UEs, affects the channel equally in all considered sub-channels and the attenuation can increase from slot to slot as the blocker moves across the LOS path

as reported in [37]. We denote as $s \in \{\text{LOS}, \text{NLOS}\}$ the state of the link between AP and UE, where LOS denotes the link having LOS propagation conditions, and NLOS the link being obstructed by blockage. We assume the state s can be periodically predicted by a blockage prediction mechanism, such as the one in [71]. At the beginning of a prediction time window, this mechanism gives a prediction $\widehat{s} \in \{\text{LOS}, \text{NLOS}\}$ to be used for the next prediction window. We assume that this prediction window has a duration of n_T time-slots.

We assume the UEs are in LOS at the beginning of the prediction window and are blocked at the end of it with probability $\mathbb{P}_\text{b}$. During the blockage, the channel gain decrease 1 dB per slot for the whole duration of the prediction window. This decay model represents the gradual attenuation caused by a blocker moving across the LOS path, as proposed in [37]. We define the amount of decay as the blockage attenuation g. Therefore, an AP-UE link going to a blocked state experiences an increasing attenuation varying between $g = 0\,\text{dB}$, when the UE is still on LOS and $g = G_\text{max}\,\text{dB}$, at the end of the prediction window. We assume the value of G_max is uniformly distributed in $[20, 40]$ as the measured values of the pedestrian blockage attenuation in [37]. We assume a frequency-selective small-scale fading gain, which has a coherence time of one time-slot and is independent between different time-slots. We model the small-scale fading gain as a Nakagami-m random variable h.

We compute the ground-truth received power at the UE u for each RB (k, t) as:

$$p_{\text{rx,u,k,t}} = p_\text{tx} \cdot a_\text{tx} \cdot \ell_0 \cdot d_u^{-\nu} \cdot g_t \cdot h_{k,t}, \tag{6.1}$$

and we define the signal-to-noise ratio (SNR) of a user as:

$$z_{u,k,t} = \frac{p_{\text{rx,u,k,t}}}{p_\text{n}}, \tag{6.2}$$

where p_tx is the transmit power, a_tx is the transmit antenna gain, ℓ_0 is the path loss at one metre distance under free space propagation, ν is the attenuation exponent, and p_n is the noise power.

6.2.3 Channel Estimation

To compute the estimated received power by the system, we assume that the system knows the transmit power, antenna gains, distance and channel propagation parameters. Thus, it only needs to estimate the blockage attenuation and small-scale fading gains. In general, we assume that the estimated values are computed by adding a Gaussian random variable ϵ to the ground-truth values such that the estimation error is $\sigma = 10^{-3}$, as in [63, 96].

To compute the estimated blockage attenuation $\widehat{g}$, the system assumes the same decay model as described in Section 6.2.2. When the blockage prediction output is $\widehat{s} = \text{NLOS}$, the estimated attenuation $\widehat{G}_\text{max}$ at the end of the prediction window is computed as $\widehat{G}_\text{max} = G_\text{max} + \epsilon$. Hence, the estimated attenuation is $\widehat{g} = 0\,\text{dB}$ in the first time-slot and increases 1 dB slot by slot up to $\widehat{g} = \widehat{G}_\text{max}$. Similarly, we compute the estimated small-scale fading

gain, as $\widehat{h} = h + \epsilon$. Therefore, the estimated received power is computed as:

$$\widehat{p}_{\mathrm{rx;g;h}} = p_{\mathrm{tx}} \cdot a_{\mathrm{tx}} \cdot \ell_0 \cdot d_u^{-\nu} \cdot \widehat{g} \cdot \widehat{h}. \tag{6.3}$$

Considering that small-scale fading estimation for long periods is not feasible [96], we assume that the small-scale fading estimation is only done for the current time-slot. Hence, we assume that the estimated received power at future time-slots within the prediction window does not consider the small-scale fading, i.e.:

$$\widehat{p}_{\mathrm{rx;g}} = p_{\mathrm{tx}} \cdot a_{\mathrm{tx}} \cdot \ell_0 \cdot d_u^{-\nu} \cdot \widehat{g}. \tag{6.4}$$

Then, the system estimates the signal-to-noise ratio (SNR) $\widehat{z}_{u,k,t}$ for every user u, sub-channel k and time-slot $t \in \{1, \ldots, n_T\}$, and compute the feasible user rate at time-slot t as:

$$r_u(t) = \sum_{k=1}^{n_{\mathrm{C}}} \Delta_b \cdot \log_2(1 + \widehat{z}_{u,k,t}) \cdot x_u(k,t) \cdot \mathbb{1}(\widehat{z}_{u,k,t} > \zeta). \tag{6.5}$$

When $\widehat{z}_{u,k,t}$ falls below a threshold $\zeta = 0\,\mathrm{dB}$, we assume that the UE u is in outage and the scheduler cannot assign an RB for that UE in (k,t). In this case, we set $\widehat{z}_{u,k,t} = 0$.

6.2.4 Scheduling Algorithms

The scheduling algorithm performs the allocation of the UE to an RB at the MAC layer. This algorithm (i.e., the scheduler) is responsible for populating the assignment matrix $\mathbf{X}$ by assigning an RB to a UE, element by element, based on a priority metric.

In the OFDMA frame, the conventional PF scheduler distributes the RBs among UEs aiming to balance between allocating UEs in favourable channel conditions and allocating UEs in worst conditions often enough to provide fair distribution. The PF scheduler performs this by giving priority to the UE that has the highest ratio of the feasible rate at the current time-slot and the average rate [97, 98]. That is, at the time-slot t, each sub-channel k is individually assigned to a user u^* such that

$$u^* = \arg\max_u \frac{r_u(t)}{\bar{r}_u(t-1)}, \tag{6.6}$$

where $\bar{r}_u(t)$ is the average rate of user u in the time slot t, and is calculated based on an exponential moving average:

$$\bar{r}_u(t) = (1-w)\,\bar{r}_u(t-1) + w\,r_u(t), \tag{6.7}$$

where $w \in [0,1]$ weights the significance of the current feasible rate. Another conventional scheduler, the Max-Min. (MM) scheduler, aims to maximise the minimum rate of a UE. This is done by prioritising the UE with the lowest average rate, assigning the RB (k,t) to

a user u^* such that

$$u^* = \arg\max_u \frac{1}{\bar{r}_u(t-1)}. \tag{6.8}$$

The priority functions in Equations (6.6) and (6.8) have the following behaviour under the effect of blockage. When blockage attenuation increases, channel quality worsens, decreasing the feasible rate, and thus decreasing the average rate as well. The PF priority function in (6.6) is directly proportional to the current feasible rate. Thus, as the feasible rate decreases with blockage attenuation, the priority of UEs suffering from blockage decreases, giving more priority to UEs in favourable conditions. This decrease in the priority is not immediate since the priority is also inversely proportional to the average rate that decreases slower than the feasible rate, depending on the weight of the moving average. Eventually, the feasible rate is so small that the priority of a UE will most likely not be the highest, and no bandwidth will be allocated. The MM priority function in (6.8) is only inversely proportional to the average rate. It means that, even when the UE is in outage, the priority keeps increasing from slot to slot as the average rate decreases. Thus, more bandwidth is allocated to the UE suffering from blockage and less bandwidth to UEs in favourable conditions. Hence, both allocations are inefficient as little bandwidth is allocated by the PF scheduler when it is needed the most and too much bandwidth is allocated by the MM scheduler when it is wasted.

To circumvent this scheduling inefficiency caused by blockages, we can use a predictive scheduler that can take advantage of the estimated channel status in future slots such as the ones in [62–64, 66], but adapted to the mmWave blockage context. A predictive scheduler can allow for the anticipation of bandwidth allocation to UEs predicted to suffer from blockage, giving more priority to these UEs at the beginning of the prediction window when the estimated channel is still favourable. This is achieved by having the denominator of the priority function as a sum of the estimated feasible rates at future time-slots. At those time-slots, the rate is expected to be low due to blockage attenuation, and thus contributing to a lower denominator, and consequently, to higher priority compared to other UEs. Moreover, other UEs will have more bandwidth available at the end of the prediction window since their feasible data rate (the priority function numerator) at future slots should be higher than the rates of users suffering from blockage, and consequently having more priority. Therefore, we adapt the priority function in (6.6) to make the PF scheduler blockage-aware, by assigning the RB (k,t) to a UE u^* such that

$$u^* = \arg\max_u \frac{r_u(t)}{S_u}, \tag{6.9}$$

where S_u is the predicted sum rate of all n_{T} slots and can be expressed as:

$$S_u = \sum_{j=1}^{n_{\mathrm{T}}} r_u\big(j \,|\, x_u(k,t) = 0\big). \tag{6.10}$$

The condition $x_u(k,t) = 0$ means that the sum does not consider that UE u to be already allocated in RB (k,t), and the comparison among the priority functions is not biased by the channel condition of a particular UE on that RB. We name the scheduler using this adapted priority function as BA-PF.

At each time-slot, the scheduler iteratively assigns an RB to a UE, from sub-channel $k = 1$ to $k = n_C$, and updates the priority function at the end of every iteration. Differently from the conventional schedulers, where the assignment is done only for the RBs of the current time-slot, the BA-PF assigns the RBs of all time-slots within the prediction window. To consider the estimated rates at future slots in the priority function, the RB assignment starts from the end of the prediction window at time-slot $t = n_{\mathrm{T}}$ and works backwards to time-slot $t = 1$, as demonstrated in Algorithm 1. Note that, as the initial value of S_u is zero,

Algorithm 1: BA-PF scheduling algorithm

Result: Allocation assignment x
$x_u(k,t) = 0, \quad \forall\, u,k,t;$
$S_u = 0, \quad \forall\, u;$
for $t = n_T$ *down to 1* **do**
  for $k = 1$ *to* n_C **do**
    $u^* = \arg\max_u \frac{r_u(t)}{S_u}$;
    $x_{u*}(k,t) = 1$;
    for $u = 1$ *to* n_U **do**
      $S_u = \sum_{j=1}^{n_{\mathrm{T}}} r_u\big(j \,|\, x_u(k,t) = 0\big)$;
    end
  end
end

the priority function is equal to "infinity" for all UEs and they have same priority in the first iteration $(t = n_T, k = 1)$. Then, the UE with smaller index u is automatically chosen, S_u is updated, and for the next iteration the priority function is a real number. This process follows until all UEs have $S_u > 0$. For the rest of the iterations, S_u increases as more RBs are assigned to UE u.

6.3 Numerical Results

6.3.1 Simulation Setup

We conducted extensive MATLAB simulations to evaluate and compare the performance of different scheduling algorithms. We simulate the transmission of n_T time-slots of an OFDMA frame according to the 5G-NR standard [99] with carrier frequency of 60 GHz from a ceiling-mounted AP to four UEs in the cell. The system parameters are given in Table 6.1. Based on the work in [71], in which the predictor can give an early warning of

blockage with up to tens of milliseconds in advance, we set the prediction window of 40 ms. For simplicity, we assume perfect blockage prediction.

Table 6.1: System parameters

Sub-channels	n_{C}	694	Time-slots	n_T	640
Sub-carrier spacing	b_{SC}	240 KHz	Slot duration	Δt	62.5 μs
Sub-channel bandwidth	Δ_b	2880 KHz	Prediction window	T	40 ms
Frame bandwidth	b	2 GHz	Moving average weight	w	0.5

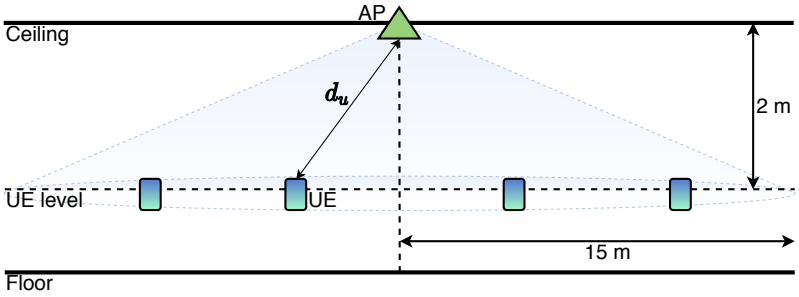

Figure 6.2: Ceiling-mounted AP setup with downward facing beam illuminating 4 UEs.

We consider that four static UEs are uniformly distributed in a cell with radius ρ =15 m and they are at the same height. The AP is positioned in the centre of the considered area at a height of 2 m above the UEs' level, as depicted in Figure 6.2. The UE-AP distance of a UE is given by d_u. The AP transmits with a power of $p_{\mathrm{tx}} = 100$ mW, and the reception at the UE has a noise figure of 9 dB, giving a noise power of $p_n = -71.99$ dBm. The transmit antenna beam is facing downward, illuminating the entire cell with a beamwidth of 170 °, giving a gain of 3.16 dBi, according to the directivity model in [100]. The channel model parameters are in line with empirically-tested channel characterisation in [1] of a LOS channel state: $\ell_0 = 63.4$ dB, $\nu = 1.72$, $m = 3.025$.

6.3.2 User Data Rate

To analyse the impact of the blockage effects on scheduling, we evaluate the user data rate distribution varying the blockage probability $\mathbb{P}_{\mathrm{b}}$. We compute the user rate at the end of the window as:

$$R_u = \frac{1}{n_T} \sum_{t=1}^{n_T} r_u(t). \tag{6.11}$$

We compare the rate of the four UEs with PF, MM, and BA-PF schedulers considering different blockage probabilities. We show the results of the empirical cumulative distribution function (ECDF) over all simulation instances in Figure 6.3.

In Figure 6.3a, we observe that when there is no blockage ($\mathbb{P}_{\mathrm{b}} = 0\%$), every UE is in LOS, and the signal attenuation produces the only discrepancy among the rates of each UE due to the distance-dependent path loss model. In this case, the BA-PF scheduler performance

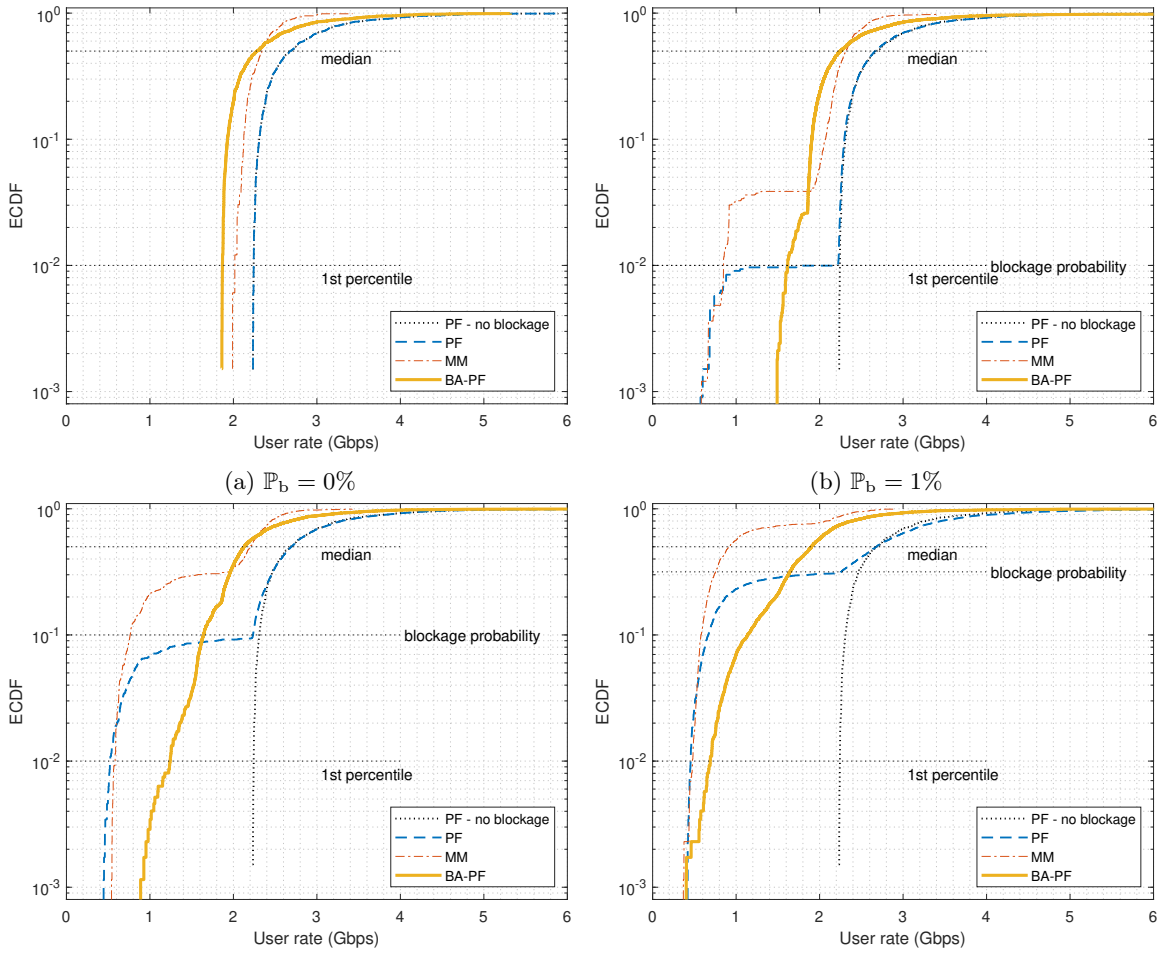

(a) $\mathbb{P}_b = 0\%$ (b) $\mathbb{P}_b = 1\%$

(c) $\mathbb{P}_b = 10\%$ (d) $\mathbb{P}_b = 31\%$

Figure 6.3: Empirical cumulative distribution function of the user rate. Comparison between the case of PF scheduler with no blockage (black line) and other schedulers with different blockage probabilities.

presents a loss in rate with respect to the PF scheduler due to imprecise channel estimation as we assumed that it does not estimate the small-scale fading gain, as we see in Figure 6.3a the yellow curve is on the left of the others. Besides, the loss in the MM scheduler performance is a result of its attempt to equalise the rate of all UEs.

Increasing the blockage probability, we see from Figures 6.3b to 6.3d that the user rate decreases which is evident from the ECDF curves shift to the left below the blockage probability threshold (depicted with a dashed line). In fact, the UEs that are affected by blockage have their data rate severely degraded when using the conventional schedulers. Specifically, concerning the MM scheduler, there is also a portion of UEs that is indirectly affected by the UEs suffering from blockage. This is because the UE affected by blockage will have higher priority on the RB assignment as the channel quality drops, hence decreasing the bandwidth available to other UEs. That is why we observe a larger portion of UEs with degraded data rate compared to the blocked UEs, as it is depicted by the red curves shifting to the left above the blockage probability line. On the other hand, with the BA-PF

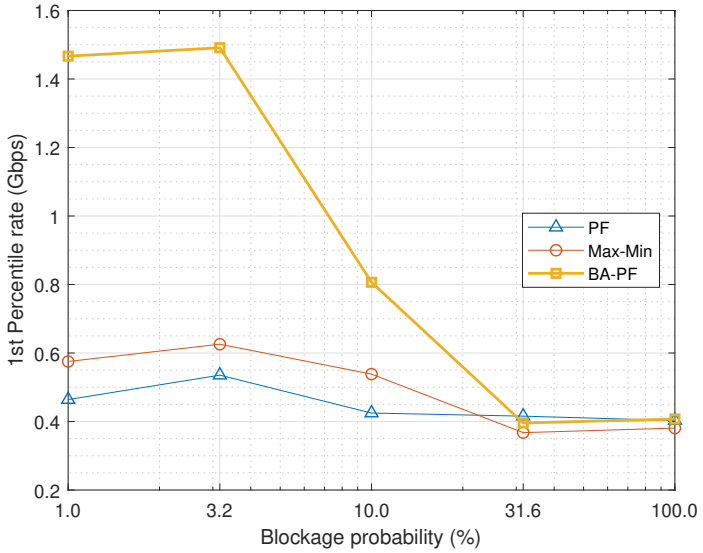

Figure 6.4: 1st percentile as a function of the blockage probability.

scheduler, the drop to the user rate due to blockage is much less severe than with other schedulers. This is because the scheduler allocates resources differently. It allocates more bandwidth to UEs suffering from blockage when the channel quality is still favourable. In fact, as we can observe from Figures 6.3b to 6.3d, the yellow curve is on the right of the other curves when the ECDF is lower than the blockage probability.

Now we focus our analysis on the 1st percentile of UEs only, as this portion of UEs is most affected by blockages. We illustrate the 1st percentile user rate as a function of the blockage probability in Figure 6.4. The 1st percentile rate for all schedulers decreases with the blockage probability as more UEs have their channel degraded by the blockage attenuation. The BA-PF scheduler shows equal or better performance than others for all blockage probabilities, meaning that the performance loss with respect to the $\mathbb{P}_b = 0\%$ scenario was best mitigated by the BA-PF scheduler. The difference in performance is bigger for low blockage probabilities, i.e., when the number of UEs suffering from blockage is small, and there is more flexibility for the BA-PF scheduler to preemptively allocate the resources for those UEs affected by blockage. On the other hand, when the blockage probability increases, the number of resources for the preemptive allocation becomes smaller for each UE, and there are limited gains from anticipating the allocation of the few resources left for each UE. Thus, it makes the BA-PF scheduler approach more similar to the conventional ones.

The improvement in the 1st percentile rate comes at the cost of a decrease in the mean rate, as shown in Figure 6.5. We observe that, when the 1st percentile rate has the highest improvement (about 0.8 Gbps when $\mathbb{P}_b < 10\%$), the costs in the mean rate are about 0.4 Gbps of loss with respect the PF scheduler. This is because preemptive allocation for those UEs suffering from blockage drains significant amount of resources taken from the pool of all the available resources.

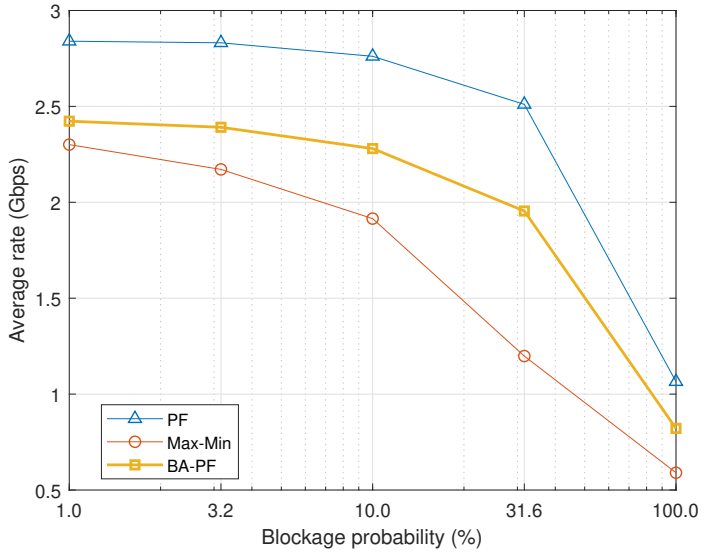

Figure 6.5: Mean rate as a function of the blockage probability.

6.4 Conclusion

In this chapter, we assessed the behaviour of schedulers in the event of a blockage affecting the LOS signal path. We showed that conventional schedulers react by allocating more bandwidth to compensate the loss in the data rate (as the MM scheduler does), or by allocating less bandwidth to prioritise other UEs with better channel conditions (as the PF scheduler does). However, when the UE is entirely in outage, a successful transmission might be impossible to achieve, and any amount of bandwidth allocated may be unused, reducing efficiency of the allocation.

This reduction in efficiency suggests that conventional schedulers should be adapted to mitigate the blockage effects in the context of 5G-mmWave networks. We therefore considered an adapted scheduling metric BA-PF which relies on blockage prediction to compute the estimated user rates, many slots ahead before a blockage event. The effectiveness of this adaptation is demonstrated by increasing the rate of the UEs affected by blockages. We showed that the difference in performance between the BA-PF scheduler and the conventional ones is more significant when the blockage probability is low, i.e., when there are fewer UEs experiencing blockage. In this case, there are enough bandwidth and time slots to allocate the anticipated transmissions to UEs suffering from blockage. This improvement on the blocked UEs' rate, comes at the expense of performance experienced by other UEs.

7 Conclusion

In this final chapter, we answer the Research Questions introduced in Chapter 1 and we discuss the overall outcomes and significance of our research. We suggest some topics for future work that can extend the work and results of this thesis. Finally, we discuss new research directions.

7.1 Summary of Contributions

In this thesis, we studied the performance of mmWave networks with ceiling-mounted AP, which is a critical use case for 5G indoor access and next-generation WiFi systems. We combined this study with the analysis of the impact of human body blockage on the performance and design of the network, which is an essential problem for 5G mmWave networks. The two topics have been individually studied before, but the combination of the two in a single study allowed us to have a new and insightful vision of the network design. The problem studied in this thesis is also important for future network generations. Hence, this work is not only valid for mmWave systems, but for any higher frequency communication systems as well, e.g. terahertz and visible light communications, because human bodies also act as obstructions in those frequencies [101, 102].

7.1.1 Research Question 1

What is the effect of blockage on the performance and the design of indoor mmWave ceiling-mounted AP networks?

We evaluated the network performance through our simulation and analytical frameworks, in which we computed the SNR/signal-to-interference-plus-noise ratio (SINR) of the signal received at the UE considering path loss, antenna gain, small-scale fading, and blockage models. In Chapter 4, we modelled the human blockage in an indoor deployment according to the ceiling-mounted setup geometry, and we characterised the blockage probability as a function of the distance between the AP and the UE. With these frameworks, we analysed the achievable network performance (coverage, spectral efficiency and user rate), testing network design aspects such as the AP density, AP and UE beamwidths (in Chapter 4), and transmission frame structure (in Chapter 5) under a number of blockage scenarios.

Table 7.1: Network design recommendation for blockage scenarios.

Blockage scenario	AP density	AP beamwidth	UE beamwidth	Slot duration	Slot aggregation
hand; empty	high	small	small	long	long
hand; crowded	high	small	large	long	long
pocket; empty	low	large	medium	short	short
pocket; crowded	low	large	small	short	short

Our results demonstrated the necessity of carefully considering the intended scenario when designing the network. This is because there are fundamental trade-offs where one configuration may not achieve both peak coverage and peak spectral efficiency at the same time. Moreover, even when we prioritise peak coverage, the most suitable configuration may not be the same for all blockage scenarios. Hence, based on the results from Chapters 3, 4 and 5, we identified in Table 7.1 the recommended design configurations for the blockage scenarios considered in this thesis, where we show how different blockage scenarios affect the design of indoor mmWave ceiling-mounted AP networks.

7.1.2 Research Question 2

How can resource allocation in MAC layer help mitigate the body blockage effects?

We focused on the study of the resource allocation in the 5G OFDMA transmission frame. First, in Chapter 5, we analysed the application of different numerologies and slot aggregations allowed by the 5G NR flexible frame under the blockage scenarios of a ceiling-mounted AP setup. Our results suggested that, given the flexibility on allocating resources in the 5G NR frame, the allocation should be adaptive according to the blockage scenario, as shown in the recommendation in Table 7.1. We found that less severe scenarios require longer slot duration and scheduling interval to reach the best performance, and more severe scenarios require the opposite. We concluded that the effect of the slot duration on mitigating the blockage effect on data rate was not as significant as the effect of the scheduling interval duration (given by the size of the slot aggregation). This is because the mmWave link performance under blockage scenarios is more sensitive to longer time resolutions (in the order of milliseconds) than to shorter time resolutions (microseconds), as the blockage state does not change as fast as one slot duration. This suggests that the scheduling of resources for blockage mitigation is more effective considering time resolutions with the same order of magnitude as a blockage event.

Taking this lesson into account, in Chapter 6, we analysed the performance of traditional scheduling algorithms. We showed the importance of an adaptive scheduling interval to mitigate the blockage effects in a scenario with multiple users sharing the frame bandwidth. We demonstrated that aided by a blockage prediction mechanism, a user suffering from blockage benefits from anticipating the transmission, i.e., shortening its scheduling interval

as similarly concluded in Chapter 5 for a single user scenario. Therefore, the MAC resource allocation can help mitigate blockage by allowing for adaptive scheduling intervals. The adaptive scheduling has to consider the specific blockage scenario and the predicted blockage events to be effective.

7.2 Future Work

7.2.1 The Impact of Multiple Users on the Design of Ceiling-Mounted AP Networks

The scenarios envisioned for 5G indoor mmWave networks (such as transportation hubs, sports arenas or other venues that attract crowds) are expected to provide satisfactory user experience for a large number of users. Thus, proper network design and resource allocation still need to be studied to address high user density.

We analysed the capacity and design of dense networks, considering inter-cell interference, but without considering whether this capacity was enough to provide satisfactory user experience for a large number of users in the venue. On the other hand, we studied the resource scheduling for multiple users considering only one cell and assuming no neighbouring interference. This makes the combination of both studies an immediate extension to this work. The combined framework may allow us to explore direct trade-offs between the network design configurations and resource scheduling mechanisms. For instance, how network density and AP/UE beamwidths are affected by the scheduling interval duration of a user suffering from blockage, or how the bandwidth available for the users changes the network design configuration. The framework may also allow us to find approaches that provide satisfactory user experience even in severe blockage scenarios (a large number of users in the venue also means a large number of human obstructions). Then, we may analyse the impact of user density on the network performance, which will allow network designers to understand the capacity limitations of mmWave networks and which configurations are needed to support a large number of users.

Multi-Connectivity

Multi-connectivity is a technique that has been proposed to provide robustness against blockage in mmWave networks [58, 60, 103]. It consists in providing association to multiple APs, enabling the UE to have alternative links for continuous connectivity in case one link is disrupted due to blockage. The robustness can be achieved, for example, using a coordinated multi-point (CoMP) method called Joint Transmission, where multiple coordinated APs simultaneously transmit data in the same frequency blocks and time-slots to a single UE, improving the received signal quality and achieving spatial diversity.

Exploring multi-connectivity within the framework suggested above leads to additional questions, as the behaviour of capacity, design and resource allocation of ceiling-mounted deployments may be different when multi-connectivity is enabled. The illumination overlap area (given by the AP beamwidth) in a cell will not anymore only depend on interference and blockage levels, but also on the resource capacity of the cell. Cells with large overlap areas may provide better robustness against blockage than those with small overlap areas, but they will cover more users sharing the same bandwidth. On the other hand, cells with small overlap areas may provide more band per user, but with fewer opportunities for the user to associate with multiple APs. Thus, there exists a trade-off to be investigated and it is open to investigation how the design of the beamwidth-density configuration will affect the network and user performance, and how the scheduler should behave when allocating resources from different APs to users suffering from blockage.

7.2.2 Application of Flexible Frame Structure to Mitigate High-Speed Mobility Effects

In terms of data rate performance, the gains we showed in Chapter 5 with flexible transmission time interval (TTI) may not be significant for blockage mitigation, but flexible TTI can indeed be very important if we want to mitigate the effects of Doppler effect and delay spread, as a fixed cyclic prefix (CP) may not be optimal for every transmission. In fact, in applications where there is a higher diversity of Doppler effect and delay spread, such as in vehicular networks where there might be users experiencing very different velocities, the users might require different lengths of CP to avoid inter-symbol interference.

7.2.3 Optimal Blockage-Aware Scheduler

Beyond the initial assessment presented in Chapter 6, there are still many challenges to be studied in blockage-aware scheduling. Our PF scheduling adaptation is based on a sub-optimal algorithm. Thus, further analysis of optimal solutions for blockage-aware schedulers is needed. The impact of blockage prediction accuracy still needs to be evaluated since inaccurate prediction will affect channel estimation and, consequently, the scheduling metric. Furthermore, more evaluation is needed during longer time intervals, spanning a sequence of prediction windows, to assess the robustness of the considered metric. Finally, consideration should be given to the impact of the blockage duration/frequency on the resource allocation performance.

7.3 Research Trends

7.3.1 Global Mobile Connectivity

To provide global mobile connectivity, 5G and beyond-5G networks are expected to integrate satellite communication networks with terrestrial cellular networks [104]. A key role envisioned for satellite communications in 5G and beyond-5G is to provide backhauling for a vast number of small cells for wide coverage areas, and for moving access points such as in ships and aircrafts [105]. Companies such as Amazon, SpaceX, OneWeb and Telesat are already launching massive satellite constellations to provide global coverage for Internet access to their customers via fixed satellite links [106]. These satellite applications are likely to use Ka-band, which is already used for conventional satellite links and partially overlaps with the mmWave band that can be allocated for terrestrial 5G user access. Because of that, research on smart spectrum sharing between satellite and terrestrial networks has started to emerge as it is a critical problem for global network integration.

7.3.2 Terahertz Communications

Future network generations will require even higher data rates than those envisioned for 5G networks according to the trends of increasing data generation and transmission. One straightforward approach is to increase data rate by increasing bandwidth. This can be done by using the very wide bandwidths in Terahertz frequencies (between 0.1 THz and 10 THz) [107]. Hence, new research on channel modelling and its implications on the network will be performed as new scenarios and use cases, different from the ones in 5G networks, will emerge.

7.3.3 Artificial Intelligence

Ubiquitous wireless coverage with satisfactory service is one of the most imperative objectives for wireless communication research. This objective is continuously challenged by the ever-increasing complexity of wireless systems, as the density of wireless devices and the diversity of wireless services continue to increase. While nowadays networks, including 5G networks, are designed based on a reactive paradigm which passively responds to incoming events, such system complexity can make the reaction time to common communication problems (e.g. link blockages, delays, traffic congestion) unsuitable for the services and applications of the next-generation networks. Hence, those networks will highly depend on prediction capabilities to enable them to anticipate the problems and proactively allocate the network resources, as suggested in Chapter 6. This paradigm-shift from reactive to proactive network design is necessary and can be made possible with the aid of artificial intelligence (AI) and machine learning (ML) techniques [108].

There are clear potential benefits of including AI into wireless communication systems, and it can thus be considered a crucial technology for beyond-5G cellular networks. Channel and interference models are extremely complicated in reality due to the highly dynamic nature of mmWave and higher frequency channels. ML techniques can automatically extract the channel information by learning from the real-time data and prior training [109–111]. They can also adaptively configure the networks by identifying received signal strength patterns and timely responding to events such as hand-off, interference and blockage [67, 68]. However, the research of AI applied to wireless communications is still in its early stages, and there is much more to be explored for networks operating in higher bands.

Appendix

A Distribution of Random Body Shadowing Angle Φ

In order to compute the probability of AP being blocked by a random body in Appendix C, we need to calculate the distribution of the random body shadowing angle. Here, since both UE and the body are uniformly positioned, the distance between them is random, which means that the body shadowing angle is also random. Thus we define the body shadowing angle Φ as a function $\varphi(R)$ of the random distance R to the body (i.e., the closer the body is to the UE, the larger the shadowing angle) and the fixed parameter — width of the body w_{B}. Then, the distribution of Φ can be obtained from the distribution of R using the following change of variable:

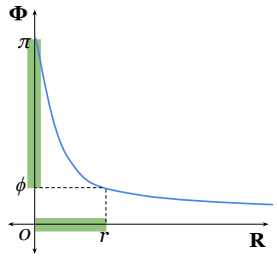

Figure 7.1: Body shadowing angle Φ as function φ of the body distance R.

$$\Phi = \varphi(R) = 2\arctan\frac{w_{\mathrm{B}}}{2R},\ R > 0. \tag{7.1}$$

$$R = \varphi^{-1}(\Phi) = \frac{w_{\mathrm{B}}}{2\tan\frac{\Phi}{2}},\ 0 < \Phi \leq \pi. \tag{7.2}$$

$$\begin{aligned}
\mathsf{F}_{\Phi}(\phi) &= \mathsf{P}[\Phi \leq \phi] \\
&= 1 - \mathsf{P}[\phi < \Phi < \pi] \\
&\overset{(a)}{=} 1 - \mathsf{P}[\varphi^{-1}(\phi) > \varphi^{-1}(\varphi(R)) > \varphi^{-1}(\pi)] \\
&= 1 - \mathsf{P}[\varphi^{-1}(\phi) > R > 0] \\
&\overset{(b)}{=} 1 - \mathsf{F}_R(\varphi^{-1}(\phi)).
\end{aligned} \tag{7.3}$$

where (a) follows from the change of variable in (7.2). It should be noted that the inversion of the inequality follows from the fact that $\varphi(R)$ is a strictly decreasing function. The cdf $\mathsf{F}_R(r)$ in step (b) is the distribution of distance R between two random points thrown on a square with side s given by Equation (53) in [112]. That equation is defined for two intervals: $r \in (0, s]$ and $r \in (s, s\sqrt{2})$. Here, we consider only the first interval $r \in (0, s]$, as we assume that blockages from very far bodies (with distance $r \in (s, s\sqrt{2})$) are negligible.

Then, the pdf is the derivative of the cdf in (7.3):

$$\begin{aligned}
\mathsf{f}_{\Phi}(\phi) &= \frac{\mathrm{d}\mathsf{F}_{\Phi}(\phi)}{\mathrm{d}\phi} = -\frac{\mathrm{d}\mathsf{F}_{R}(\varphi^{-1}(\phi))}{\mathrm{d}\phi} \\
&\overset{(a)}{=} -\frac{\mathrm{d}\mathsf{F}_{R}(r)}{\mathrm{d}\phi} = -\frac{\mathrm{d}\mathsf{F}_{R}(r)}{\mathrm{d}r}\frac{\mathrm{d}r}{\mathrm{d}\phi} \\
&= -\left(\frac{2\pi r}{s^2} - \frac{8r^2}{s^3} + \frac{2r^3}{s^4}\right)\frac{w_{\mathrm{B}}}{2(\cos\phi - 1)} \\
&\overset{(b)}{=} -\left(\frac{\pi\rho}{s^2} - \frac{4\rho^2}{s^3} + \frac{\rho^3}{s^4}\right)\frac{w_{\mathrm{B}}}{(\cos\phi - 1)},
\end{aligned} \tag{7.4}$$

where (a) follows from the change of variable in (7.2), and (b) follows from the change of variable in (7.1), with ρ as a short notation of the function $\varphi^{-1}(\phi) = w_{\mathrm{B}}/(2\tan\frac{\phi}{2})$.

B Probability of Self-body Blockage

The event [*the AP is blocked by user body*] is a specific case of the event given by Definition 3, where we know that the user body is at a fixed distance r_0 from the UE and its orientation is a random variable Θ uniformly distributed in $[0, 2\pi)$. Then, the event [*the AP is blocked by user body*] is given by:

$$[\Theta < \phi_0] \cap [d_{\mathrm{A}} \geq z_0], \tag{7.5}$$

where $z_0 = r_0 \cdot \frac{h_{\mathrm{A}}}{h_{\mathrm{B}}}$ is self-body blockage free zone and $\phi_0 = \varphi(r_0)$ is the self-body shadowing angle. Therefore, since the body orientation Θ is independent of the distance r_0, the probability of self-body blockage is:

$$\begin{aligned}
p_0 &= \mathsf{P}[\Theta \leq \varphi(r_0) \ \cap \ r_0 \leq d_{\mathrm{A}} \cdot h_{\mathrm{B}}/h_{\mathrm{A}}] \\
&= \mathsf{P}[\Theta \leq \varphi(r_0)] \ \mathbb{1}_{(r_0 \leq d_{\mathrm{A}}\, h_{\mathrm{B}}/h_{\mathrm{A}})}
\end{aligned} \tag{7.6}$$

It means that if the UE is at a distance $d_{\mathrm{A}} \leq r_0 \cdot h_{\mathrm{A}}/h_{\mathrm{B}}$, the probability of self-body blockage is zero (UE inside the self-blocking free zone). Otherwise, the probability is $\mathsf{F}_{\Theta}(\varphi(r_0))$. Thus, we can express p_0 as:

$$\begin{aligned}
p_0(d_{\mathrm{A}}) &= \mathsf{F}_{\Theta}(\varphi(r_0)) \cdot \mathbb{1}_{(r_0 \leq d_{\mathrm{A}}\, h_{\mathrm{B}}/h_{\mathrm{A}})} \\
&= \frac{\varphi(r_0)}{2\pi} \cdot \mathbb{1}_{(r_0 \leq d_{\mathrm{A}}\, h_{\mathrm{B}}/h_{\mathrm{A}})} \\
&= \begin{cases} \dfrac{\arctan(w_{\mathrm{B}}/2r_0)}{\pi}, & d_{\mathrm{A}} > r_0 \cdot h_{\mathrm{A}}/h_{\mathrm{B}}; \\ 0, & 0 < d_{\mathrm{A}} \leq r_0 \cdot h_{\mathrm{A}}/h_{\mathrm{B}}. \end{cases}
\end{aligned} \tag{7.7}$$

C Probability of AP Being Blocked by a Random Body

Assuming both user equipment (UE) and an random body (RB) (not the user) positions are uniformly distributed, the event [*the body is in between the AP and UE*] depends on the distance R from the RB to the UE, on the body shadowing angle Φ (these random variables are discussed in Appendix A), and on the body orientation Θ, which we also assume to be uniformly distributed in $[0, 2\pi)$ for an RB. Then, applying the Definition 3 to a random body, the event [*the AP is blocked by a random body*] is given by:

$$[\Theta < \Phi] \cap [d_{\mathrm{A}} \geq Z], \tag{7.8}$$

where $Z = R \cdot \frac{h_{\mathrm{A}}}{h_{\mathrm{B}}}$ is the blockage free zone and $\Phi = \varphi(R)$ is the body shadowing angle. Therefore, the probability of blockage by a random body is:

$$\begin{aligned}
p_1(d_{\mathrm{A}}) &= \mathsf{P}[\Phi > \Theta \ \cap \ 0 < R \leq d_{\mathrm{A}} \cdot h_{\mathrm{B}}/h_{\mathrm{A}}] \\
&\overset{(a)}{=} \mathsf{P}[\Phi > \Theta \ \cap \ \varphi(d_{\mathrm{A}} \cdot h_{\mathrm{B}}/h_{\mathrm{A}}) < \Phi < \varphi(0)] \\
&= \mathsf{P}[\Phi > \Theta \ \cap \ \varphi(d_{\mathrm{A}} \cdot h_{\mathrm{B}}/h_{\mathrm{A}}) < \Phi < \pi] \\
&= \int_{\varphi(d_{\mathrm{A}} \cdot h_{\mathrm{B}}/h_{\mathrm{A}})}^{\pi} \int_{0}^{\phi} \mathsf{f}_{\Theta,\Phi}(\theta, \phi) \, \mathrm{d}\theta \mathrm{d}\phi \\
&\overset{(b)}{=} \int_{\varphi(d_{\mathrm{A}} \cdot h_{\mathrm{B}}/h_{\mathrm{A}})}^{\pi} \int_{0}^{\phi} \mathsf{f}_{\Theta}(\theta) \mathrm{d}\theta \, \mathsf{f}_{\Phi}(\phi) \mathrm{d}\phi \\
&= \int_{\varphi(d_{\mathrm{A}} \cdot h_{\mathrm{B}}/h_{\mathrm{A}})}^{\pi} \mathsf{F}_{\Theta}(\phi) \mathsf{f}_{\Phi}(\phi) \, \mathrm{d}\phi \\
&\overset{(c)}{=} \int_{\varphi(d_{\mathrm{A}} \cdot h_{\mathrm{B}}/h_{\mathrm{A}})}^{\pi} \frac{\phi}{2\pi} \frac{-w_{\mathrm{B}}}{(\cos\phi - 1)} \left(\frac{\pi\rho}{s^2} - \frac{4\rho^2}{s^3} + \frac{\rho^3}{s^4} \right) \, \mathrm{d}\phi,
\end{aligned} \tag{7.9}$$

where (a) follows from making a change of variables, (b) follows from the independence of Θ and R, and consequently, of Θ and Φ, and (c) follows from substituting the cdf of Θ and the pdf of Φ with (7.4) given in Appendix A.

Acronyms

mmWave millimetre-wave

ASE area spectral efficiency

AP access point

UE user equipment

UB user body

RB random body

TTI transmission time interval

LOS line-of-sight

NLOS non-line-of-sight

SCS sub-carrier spacing

OFDM orthogonal frequency-division multiplexing

URLLC ultra-reliable low-latency communication

eMBB enhanced mobile broadband

mMTC massive machine type communications

CP cyclic prefix

MAC medium access control

CoMP coordinated multi-point

NR new radio

SI scheduling interval

PF Proportional Fair

MM Max-Min.

SNR signal-to-noise ratio

SINR signal-to-interference-plus-noise ratio

AI artificial intelligence

ML machine learning

OFDMA orthogonal frequency-division multiple access

BA-PF Blockage-Aware Predictive Proportional Fair

Bibliography

[1] S. K. Yoo, S. L. Cotton, R. W. Heath, and Y. J. Chun, "Measurements of the 60 GHz UE to eNB Channel for Small Cell Deployments," *IEEE Wireless Communications Letters*, vol. 6, no. 2, pp. 178–181, Apr. 2017.

[2] S. K. Yoo *et al.*, "Channel Characteristics of Dynamic Off-Body Communications at 60 GHz Under Line-of-Sight (LOS) and Non-LOS Conditions," *IEEE Antennas and Wireless Propagation Letters*, vol. 16, pp. 1553–1556, Feb. 2017.

[3] GSMA Intelligence. (2020, Mar.) The Mobile Economy 2020. Accessed 20th Mar. 2020. [Online]. Available: https://www.gsmaintelligence.com/research/2020/03/the-mobile-economy-2020/1866/

[4] "IMT Vision–Framework and Overall Objectives of the Future Development of IMT for 2020 and Beyond," *Recommendation ITU*, vol. M Series, pp. 2083–0, Sep. 2015.

[5] M. Shafi *et al.*, "5G: A Tutorial Overview of Standards, Trials, Challenges, Deployment, and Practice," *IEEE Journal on Selected Areas in Communications*, vol. 35, no. 6, pp. 1201–1221, June 2017.

[6] M. Shafi *et al.*, "Microwave vs. Millimeter-Wave Propagation Channels: Key Differences and Impact on 5G Cellular Systems," *IEEE Communications Magazine*, vol. 56, no. 12, pp. 14–20, Dec. 2018.

[7] Z. Pi and F. Khan, "An Introduction to Millimeter-Wave Mobile Broadband Systems," *IEEE Communications Magazine*, vol. 49, no. 6, pp. 101–107, June 2011.

[8] S. Collonge, G. Zaharia, and G. E. Zein, "Influence of the Human Activity on Wide-Band Characteristics of the 60 GHz Indoor Radio Channel," *IEEE Trans. Wireless Communications*, vol. 3, no. 6, pp. 2396–2406, Nov. 2004.

[9] J. S. Lu, D. Steinbach, P. Cabrol, and P. Pietraski, "Modeling Human Blockers in Millimeter Wave Radio Links," *ZTE Communications*, vol. 10, no. 4, pp. 23–28, 2012.

[10] T. Bai and R. W. Heath, "Analysis of Self-Body Blocking Effects in Millimeter Wave Cellular Networks," in *2014 48th Asilomar Conf. Signals, Systems and Computers*. IEEE, Nov. 2014, pp. 1921–1925.

[11] K. Venugopal, M. C. Valenti, and R. W. Heath, "Device-to-Device Millimeter Wave Communications: Interference, Coverage, Rate, and Finite Topologies," *IEEE Trans. Wireless Communications*, vol. 15, no. 9, pp. 6175–6188, Sep. 2016.

[12] M. Gapeyenko *et al.*, "Analysis of Human-Body Blockage in Urban Millimeter-Wave Cellular Communications," in *2016 IEEE Int'l Conf. Communications (ICC)*, May 2016, pp. 1–7.

[13] S. Niknam, B. Natarajan, and R. Barazideh, "Interference Analysis for Finite-Area 5G mmWave Networks Considering Blockage Effect," *IEEE Access*, vol. 6, pp. 23 470–23 479, Apr. 2018.

[14] I. K. Jain, R. Kumar, and S. S. Panwar, "The Impact of Mobile Blockers on Millimeter Wave Cellular Systems," *IEEE Journal on Selected Areas in Communications*, vol. 37, no. 4, pp. 854–868, Apr. 2019.

[15] M. Ibrahim and W. Xu, "On Numerology and Capacity of the Self-Contained Frame Structure," in *2016 IEEE Global Communications Workshops (GLOBECOM)*, Dec. 2016, pp. 1–6.

[16] N. Patriciello, S. Lagen, L. Giupponi, and B. Bojovic, "5G New Radio Numerologies and their Impact on the End-To-End Latency," in *2018 IEEE 23rd International Workshop on Computer Aided Modeling and Design of Communication Links and Networks (CAMAD)*, Sep. 2018, pp. 1–6.

[17] S. Kwon and J. Widmer, "Multi-Beam Power Allocation for mmWave Communications under Random Blockage," in *2018 IEEE Vehicular Technology Conference (VTC)*, June 2018, pp. 1–5.

[18] M. Feng, S. Mao, and T. Jiang, "Dealing with Link Blockage in mmWave Networks: D2D Relaying or Multi-beam Reflection?" in *2017 IEEE International Symposium on Personal, Indoor and Mobile Radio Communications (PIMRC)*, Oct. 2017, pp. 1–5.

[19] S. Wu, R. Atat, N. Mastronarde, and L. Liu, "Coverage Analysis of D2D Relay-Assisted Millimeter-wave Cellular Networks," in *2017 IEEE Wireless Communications and Networking Conference (WCNC)*, Mar. 2017, pp. 1–6.

[20] Z. Yang *et al.*, "Sense and Deploy: Blockage-aware Deployment of Reliable 60 GHz mmWave WLANs," in *2018 IEEE 15th International Conference on Mobile Ad Hoc and Sensor Systems (MASS)*, Oct. 2018, pp. 397–405.

[21] J. Bao, D. Sprinz, and H. Li, "Blockage of Millimeter Wave Communications on Rotor UAVs: Demonstration and Mitigation," in *2017 IEEE Military Communications Conference (MILCOM)*, Oct. 2017, pp. 768–774.

[22] C. Tatino, I. Malanchini, N. Pappas, and D. Yuan, "Maximum Throughput Scheduling for Multi-Connectivity in Millimeter-Wave Networks," in *2018 16th International Symposium on Modeling and Optimization in Mobile, Ad Hoc, and Wireless Networks (WiOpt)*, May 2018, pp. 1–6.

[23] V. Petrov *et al.*, "Achieving End-to-End Reliability of Mission-Critical Traffic in Softwarized 5G Networks," *IEEE Journal on Selected Areas in Communications*, pp. 485–501, Mar. 2018.

[24] T. Bai and R. W. Heath, "Coverage Analysis for Millimeter Wave Cellular Networks with Blockage Effects," in *2013 IEEE Global Conf. Signal and Information Processing (GlobalSIP)*, Dec. 2013, pp. 727–730.

[25] ——, "Coverage in Dense Millimeter Wave Cellular Networks," in *2013 47th Asilomar Conf. Signals, Systems and Computers*. IEEE, Nov. 2013, pp. 2062–2066.

[26] ——, "Coverage and Rate Analysis for Millimeter-Wave Cellular Networks," *IEEE Trans. Wireless Communications*, vol. 14, no. 2, pp. 1100–1114, Feb. 2015.

[27] J. Yoon and G. Hwang, "Distance-Based Inter-Cell Interference Coordination in Small Cell Networks: Stochastic Geometry Modeling and Analysis," *IEEE Trans. Wireless Communications*, vol. 17, no. 6, pp. 4089–4103, June 2018.

[28] "Technical Feasibility of IMT in Bands Above 6 GHz," International Telecommunication Union, Tech. Rep. ITU-R M.2376-0, Jul. 2015. [Online]. Available: https://www.itu.int/pub/R-REP-M.2376

[29] L. Ho, D. Lopez-Perez, and H. Claussen, "Downward Facing Directional Antennas for Ultra-High Density Indoor Small Cells," *Journal of Signal Processing Systems*, vol. 83, no. 2, pp. 255–263, May 2016.

[30] C. Yiu and S. Singh, "Empirical Capacity of mmWave WLANs," *IEEE Journal on Selected Areas in Communications*, vol. 27, no. 8, pp. 1479–1487, Sep. 2009.

[31] K. Dong, X. Liao, and S. Zhu, "Link Blockage Analysis for Indoor 60ghz Radio Systems," *Electronics Letters*, vol. 48, no. 23, pp. 1506–1508, Nov. 2012.

[32] C. S. Leong, B.-S. Lee, A. R. Nix, and P. Strauch, "A Robust 60 GHz Wireless Network with Parallel Relaying," in *2004 IEEE Int'l Conf. Communications (ICC)*, vol. 6, June 2004, pp. 3528–3532.

[33] R. A. Krofli and R. D. Kelly, "Meteorological Research Applications of MM-Wave Radar," *Meteorology and Atmospheric Physics*, vol. 59, no. 1, pp. 105–121, Mar. 1996. [Online]. Available: https://doi.org/10.1007/BF01032003

[34] A. Luukanen, R. Appleby, M. Kemp, and N. Salmon, *Millimeter-Wave and Terahertz Imaging in Security Applications*. Berlin, Heidelberg: Springer Berlin Heidelberg, 2013, pp. 491–520. [Online]. Available: https://doi.org/10.1007/978-3-642-29564-5_19

[35] M. Rojavin and M. Ziskin, "Medical Application of Millimetre Waves," *QJM: monthly journal of the Association of Physicians*, vol. 91, no. 1, pp. 57–66, Jan. 1998.

[36] A. V. Alejos, M. G. Sanchez, and I. Cuinas, "Measurement and Analysis of Propagation Mechanisms at 40 GHz: Viability of Site Shielding Forced by Obstacles," *IEEE Transactions on Vehicular Technology*, vol. 57, no. 6, pp. 3369–3380, Nov. 2008.

[37] G. R. Maccartney, T. S. Rappaport, and S. Rangan, "Rapid Fading Due to Human Blockage in Pedestrian Crowds at 5G Millimeter-Wave Frequencies," in *2017 IEEE Global Communications Conference (GLOBECOM)*, Dec. 2017.

[38] H. Xu, V. Kukshya, and T. S. Rappaport, "Spatial and Temporal Characteristics of 60-GHZ Indoor Channels," *IEEE Journal on Selected Areas in Communications*, vol. 20, no. 3, pp. 620–630, Aug. 2002.

[39] S. Rajagopal, S. Abu-Surra, and M. Malmirchegini, "Channel Feasibility for Outdoor Non-Line-of-Sight mmWave Mobile Communication," in *2012 IEEE Vehicular Technology Conf. (VTC Fall)*, Sep. 2012, pp. 1–6.

[40] T. S. Rappaport *et al.*, "Millimeter Wave Mobile Communications for 5G Cellular: It Will Work!" *IEEE access*, vol. 1, pp. 335–349, 2013.

[41] G. R. Maccartney, T. S. Rappaport, S. Sun, and S. Deng, "Indoor Office Wideband Millimeter-Wave Propagation Measurements and Channel Models at 28 and 73 GHz for Ultra-Dense 5G Wireless Networks," *IEEE Access*, vol. 3, pp. 2388–2424, 2015.

[42] S. Deng, M. K. Samimi, and T. S. Rappaport, "28 GHz and 73 GHz millimeter-wave indoor propagation measurements and path loss models," in *2015 IEEE International Conference on Communication Workshop, ICCW 2015*, 2015, pp. 1244–1250.

[43] A. F. Molisch *et al.*, "Millimeter-wave Channels in Urban Environments," in *2016 10th European Conference on Antennas and Propagation, EuCAP 2016*, 2016, pp. 1–5.

[44] M. Wang, Y. Liu, S. Li, and Z. Chen, "60 GHz Millimeter-Wave Propagation Characteristics in Indoor Environment," in *2017 9th IEEE International Conference on Communication Software and Networks, ICCSN 2017*, May 2017, pp. 749–752.

[45] J. Ko *et al.*, "28 GHz Millimeter-Wave Measurements and Models for Signal Attenuation in Vegetated Areas," in *2017 11th European Conference on Antennas and Propagation, EUCAP 2017*, Mar. 2017, pp. 1808–1812.

[46] J. J. Park *et al.*, "Millimeter Wave Vehicular Blockage Characteristics based on 28 GHz Measurements," in *IEEE Vehicular Technology Conference*, Sep. 2017, pp. 1–5.

[47] A. M. Al-Samman, T. Abd Rahman, and M. H. Azmi, "Indoor Corridor Wideband Radio Propagation Measurements and Channel Models for 5G Millimeter Wave Wireless Communications at 19 GHz, 28 GHz, and 38 GHz Bands," *Wireless Communications and Mobile Computing*, vol. 2018, pp. 1–12, Mar. 2018.

[48] S. K. Yoo, S. L. Cotton, Y. J. Chun, and W. G. Scanlon, "Fading Characterization of UE to Ceiling-Mounted Access Point Communications at 60 GHz," in *12th European Conf. Antennas and Propagation (EuCAP) 2018: Proceedings*, Apr. 2018, pp. 1–5.

[49] J. G. Andrews *et al.*, "Modeling and Analyzing Millimeter Wave Cellular Systems," *IEEE Trans. Communications*, vol. 65, no. 1, pp. 403–430, Jan. 2017.

[50] T. Bai, R. Vaze, and R. W. Heath, "Analysis of Blockage Effects on Urban Cellular Networks," *IEEE Transactions on Wireless Communications*, vol. 13, no. 9, pp. 5070–5083, Sep. 2014.

[51] C. K. Anjinappa and I. Guvenc, "Millimeter-Wave V2X Channels: Propagation Statistics, Beamforming, and Blockage," in *2018 IEEE 88th Vehicular Technology Conference (VTC-Fall)*, Aug. 2018, pp. 1–6.

[52] M. U. Sheikh *et al.*, "Usability Benefits and Challenges in mmWave V2V Communications: A Case Study," in *2019 International Conference on Wireless and Mobile Computing, Networking and Communications (WiMob)*, Oct. 2019, pp. 1–5.

[53] E. Hriba, M. C. Valenti, K. Venugopal, and R. W. Heath, "Accurately Accounting for Random Blockage in Device-to-Device mmWave Networks," in *GLOBECOM 2017 - 2017 IEEE Global Communications Conf.*, Dec. 2017, pp. 1–6.

[54] K. Venugopal and R. W. Heath, "Millimeter Wave Networked Wearables in Dense Indoor Environments," *IEEE Access*, vol. 4, pp. 1205–1221, 2016.

[55] I. K. Jain, R. Kumar, and S. Panwar, "Driven by Capacity or Blockage? A Millimeter Wave Blockage Analysis," in *2018 IEEE International Teletraffic Congress (ITC)*, Sep. 2018, pp. 153–159.

[56] M. Gapeyenko *et al.*, "On the Temporal Effects of Mobile Blockers in Urban Millimeter-Wave Cellular Scenarios," *IEEE Transactions on Vehicular Technology*, vol. 66, no. 11, pp. 10 124–10 138, Nov 2017.

[57] D. Moltchanov and A. Ometov, "On the fraction of los blockage time in mmwave systems with mobile users and blockers," in *Wired/Wireless Internet Communications*, K. R. Chowdhury, M. Di Felice, I. Matta, and B. Sheng, Eds. Cham: Springer International Publishing, 2018, pp. 183–192.

[58] F. B. Tesema *et al.*, "Multiconnectivity for Mobility Robustness in Standalone 5G Ultra Dense Networks with Intrafrequency Cloud Radio Access," *Wireless Communications and Mobile Computing*, pp. 1–17, Jan. 2017.

[59] M. Giordani, M. Mezzavilla, S. Rangan, and M. Zorzi, "Multi-Connectivity in 5G mmWave Cellular Networks," in *2016 15th IFIP Mediterranean Ad Hoc Networking Workshop (MEDHOCNET)*, June 2016, pp. 1–7.

[60] V. Petrov *et al.*, "Dynamic Multi-Connectivity Performance in Ultra-Dense Urban mmWave Deployments," *IEEE Journal on Selected Areas in Communications*, pp. 2038–2055, Sep. 2017.

[61] M. Polese *et al.*, "Improved Handover Through Dual Connectivity in 5G mmWave Mobile Networks," *IEEE Journal on Selected Areas in Communications*, pp. 2069–2084, Sep. 2017.

[62] H. J. Bang, T. Ekman, and D. Gesbert, "Channel Predictive Proportional Fair Scheduling," *IEEE Transactions on Wireless Communications*, vol. 7, no. 2, pp. 482–487, Feb 2008.

[63] J. Hajipour and V. C. M. Leung, "Proportional Fair Scheduling in Multi-Carrier Networks Using Channel Predictions," in *2010 IEEE International Conference on Communications*, May 2010, pp. 1–5.

[64] J. F. Schmidt, J. E. Cousseau, R. Wichman, and S. Werner, "Prediction based resource allocation in ofdma," in *2011 45th Annual Conference on Information Sciences and Systems*, March 2011, pp. 1–4.

[65] R. Margolies *et al.*, "Exploiting Mobility in Proportional Fair Cellular Scheduling: Measurements and Algorithms," *IEEE/ACM Transactions on Networking*, vol. 24, no. 1, pp. 355–367, Feb. 2016.

[66] L. Shen, T. Wang, and S. Wang, "Proactive Proportional Fair: A Novel Scheduling Algorithm Based on Future Channel Information in OFDMA Systems," in *2019 IEEE/CIC International Conference on Communications in China (ICCC)*, Aug. 2019, pp. 925–930.

[67] A. Alkhateeb, I. Beltagy, and S. Alex, "Machine Learning for Reliable mmwave Systems: Blockage Prediction and Proactive Handoff," in *2018 IEEE Global Conference on Signal and Information Processing (GlobalSIP)*, Nov. 2018, pp. 1055–1059.

[68] M. Alrabeiah and A. Alkhateeb, "Deep Learning for mmWave Beam and Blockage Prediction using Sub-6GHz Channels," *arXiv preprint arXiv:1910.02900*, Oct. 2019.

[69] M. Alrabeiah, A. Hredzak, and A. Alkhateeb, "Millimeter Wave Base Stations with Cameras: Vision Aided Beam and Blockage Prediction," *arXiv preprint arXiv:1911.06255*, Nov. 2019.

[70] M. Zarifneshat, L. Xiao, and J. Tang, "Learning-based Blockage Prediction for Robust Links in Dynamic Millimeter Wave Networks," in *2019 16th Annual IEEE International Conference on Sensing, Communication, and Networking (SECON)*, June 2019, pp. 1–9.

[71] Z. Ali, A. Duel-Hallen, and H. Hallen, "Early Warning of mmWave Signal Blockage and AoA Transition Using sub-6 GHz Observations," *IEEE Communications Letters*, pp. 1–1, Nov. 2019.

[72] I. Hwang, B. Song, and S. S. Soliman, "A Holistic View on Hyper-Dense Heterogeneous and Small Cell Networks," *IEEE Communications Magazine*, vol. 51, no. 6, pp. 20–27, June 2013.

[73] B. W. Ku, D. G. Han, and Y. S. Cho, "Efficient Beam-Training Technique for Millimeter-Wave Cellular Communications," *Etri Journal*, vol. 38, no. 1, pp. 81–89, Feb. 2016.

[74] R. Ramanathan, "On the Performance of Ad Hoc Networks with Beamforming Antennas," in *Proc. the 2nd ACM Int'l Symp. Mobile Ad Hoc Networking & Computing*, Oct. 2001, pp. 95–105.

[75] "Radio-Frequency Channel Arrangements for Fixed Wireless Systems Operating in the Band 55.78-66 GHz," International Telecommunication Union, Tech. Rep. ITU-R F.1497-2, Feb. 2014. [Online]. Available: https://www.itu.int/rec/R-REC-F.1497/en

[76] R. C. Daniels, J. N. Murdock, T. S. Rappaport, and R. W. Heath, "60 GHz Wireless: Up Close and Personal," *IEEE Microwave Magazine*, vol. 11, no. 7, pp. 44–50, Dec. 2010.

[77] S. Scarr, M. Sharma, M. Hernandez, and V. Tong. Measuring the Masses, the Contentious Issue of Crowd Counting in Hong Kong. Accessed Sep. 12 2019. [Online]. Available: https://graphics.reuters.com/HONGKONG-EXTRADITION-PROTESTS/0100B01001H/index.html

[78] G. R. Maccartney, T. S. Rappaport, and S. Rangan, "Rapid Fading Due to Human Blockage in Pedestrian Crowds at 5G Millimeter-Wave Frequencies," in *2017 IEEE Global Communications Conference (GLOBECOM)*, Dec. 2017, pp. 1–7.

[79] A. Narayanan, S. T. V., and R. K. Ganti, "Coverage Analysis in Millimeter Wave Cellular Networks with Reflections," in *GLOBECOM 2017 - 2017 IEEE Global Communications Conf.*, Dec. 2017, pp. 1–6.

[80] W. I. Kim, J. S. Song, and S. K. Baek, "Relay-Assisted Handover to Overcome Blockage in Millimeter-Wave Networks," in *2017 IEEE International Symposium on Personal, Indoor and Mobile Radio Communications (PIMRC)*, Oct. 2017.

[81] F. Firyaguna, J. Kibilda, C. Galiotto, and N. Marchetti, "Coverage and Spectral Efficiency of Indoor mmWave Networks with Ceiling-Mounted Access Points," in *2017 IEEE Global Communications Conf. - GLOBECOM 2017*, Dec. 2017, pp. 1–7.

[82] M. Gapeyenko *et al.*, "Effects of Blockage in Deploying mmWave Drone Base Stations for 5G Networks and Beyond," in *2018 IEEE International Conference on Communications Workshops (ICC)*, May 2018, pp. 1–6.

[83] 3GPP 38.211, "NR; Physical Channels and Modulation," Technical Report (TR) V15.3.0, Sep. 2018.

[84] S. Lagen *et al.*, "Subband Configuration Optimization for Multiplexing of Numerologies in 5G TDD New Radio," in *2018 IEEE International Symposium on Personal, Indoor and Mobile Radio Communications (PIMRC)*, Sep. 2018, pp. 1–7.

[85] L. You, Q. Liao, N. Pappas, and D. Yuan, "Resource Optimization With Flexible Numerology and Frame Structure for Heterogeneous Services," *IEEE Communications Letters*, vol. 22, no. 12, pp. 2579–2582, Dec 2018.

[86] "5G NR; User Equipment (UE) Radio Transmission and Reception; Part 2: Range 2 Standalone," 3GPP, Tech. Rep. TS 38.101-2 V15.3.0, Oct. 2018.

[87] "5G; Study on Scenarios and Requirements for Next Generation Access Technologies," 3GPP, Tech. Rep. TR 38.913 V14.2.0, May 2017.

[88] A. Laourine, M. Alouini, S. Affes, and A. Stephenne, "On the Performance Analysis of Composite Multipath/Shadowing Channels using the G-Distribution," *IEEE Transactions on Communications*, vol. 57, no. 4, pp. 1162–1170, Apr. 2009.

[89] E. Lahetkangas *et al.*, "Achieving Low Latency and Energy Consumption by 5G TDD Mode Optimization," in *2014 IEEE International Conference on Communications Workshops (ICC)*, June 2014.

[90] E. Lahetkangas, K. Pajukoski, J. Vihriala, and E. Tiirola, "On the Flexible 5G Dense Deployment Air Interface for Mobile Broadband," in *1st International Conference on 5G for Ubiquitous Connectivity*, Nov. 2014, pp. 57–61.

[91] P. Mogensen *et al.*, "5G Small Cell Optimized Radio Design," in *2013 IEEE Global Communications Workshops (GLOBECOM)*, Dec. 2013, pp. 111–116.

[92] F. Capozzi *et al.*, "Downlink Packet Scheduling in LTE Cellular Networks: Key Design Issues and a Survey," *IEEE Communications Surveys Tutorials*, vol. 15, no. 2, pp. 678–700, Feb. 2013.

[93] A. K. Gupta, J. G. Andrews, and R. W. Heath, "Macrodiversity in Cellular Networks With Random Blockages," *IEEE Transactions on Wireless Communications*, vol. 17, no. 2, pp. 996–1010, Feb. 2018.

[94] C. Liu and L. Xiao, "Interference and Blockage Prediction in mmWave-Enabled HetNets," in *2018 IEEE 26th International Symposium on Modeling, Analysis, and Simulation of Computer and Telecommunication Systems (MASCOTS)*, Sep. 2018, pp. 201–208.

[95] T. Nishio *et al.*, "Proactive Received Power Prediction Using Machine Learning and Depth Images for mmWave Networks," *IEEE Journal on Selected Areas in Communications*, vol. 37, no. 11, pp. 2413–2427, Nov. 2019.

[96] A. Duel-Hallen, H. Hallen, and Tung-Sheng Yang, "Long Range Prediction and Reduced Feedback for Mobile Radio Adaptive OFDM Systems," *IEEE Transactions on Wireless Communications*, vol. 5, no. 10, pp. 2723–2733, Oct. 2006.

[97] Hoon Kim and Youngnam Han, "A Proportional Fair Scheduling for Multicarrier Transmission Systems," *IEEE Communications Letters*, vol. 9, no. 3, pp. 210–212, Mar. 2005.

[98] E. Liu and K. K. Leung, "Proportional Fair Scheduling: Analytical Insight under Rayleigh Fading Environment," in *2008 IEEE Wireless Communications and Networking Conference*. IEEE, Mar. 2008, pp. 1883–1888.

[99] "5G NR; Base Station (BS) Radio Transmission and Reception," 3GPP, Tech. Rep. TS 138 104 V15.3.0, Jul. 2018.

[100] F. Firyaguna, J. Kibilda, C. Galiotto, and N. Marchetti, "Performance Analysis of Indoor mmWave Networks with Ceiling-Mounted Access Points," *IEEE Transactions on Mobile Computing*, pp. 1–1, Feb. 2020.

[101] O. Erturk and T. Yilmaz, "A Hexagonal Grid Based Human Blockage Model for the 5G Low Terahertz Band Communications," in *2018 IEEE 5G World Forum (5GWF)*, Jul. 2018, pp. 395–398.

[102] V. Rodoplu *et al.*, "Characterization of Line-of-Sight Link Availability in Indoor Visible Light Communication Networks Based on the Behavior of Human Users," *IEEE Access*, vol. 8, pp. 39 336–39 348, Feb. 2020.

[103] D. Maamari, N. Devroye, and D. Tuninetti, "Coverage in mmWave Cellular Networks with Base Station Co-Operation," *IEEE Transactions on Wireless Communications*, vol. 15, no. 4, pp. 2981–2994, Jan. 2016.

[104] M. Z. Chowdhury, M. Shahjalal, S. Ahmed, and Y. M. Jang, "6G Wireless Communication Systems: Applications, Requirements, Technologies, Challenges, and Research Directions," *arXiv preprint arXiv:1909.11315*, Sep. 2019.

[105] B. G. Evans, "The Role of Satellites in 5G," in *2014 7th Advanced Satellite Multimedia Systems Conference and the 13th Signal Processing for Space Communications Workshop (ASMS/SPSC)*. IEEE, Sep. 2014, pp. 197–202.

[106] I. del Portillo, B. G. Cameron, and E. F. Crawley, "A Technical Comparison of Three Low Earth Orbit Satellite Constellation Systems to Provide Global Broadband," *Acta Astronautica*, vol. 159, pp. 123–135, Jun. 2019.

[107] "Technology trends of active services in the frequency range 275-3 000 GHz," ITU, Tech. Rep. ITU-R SM.2352-0, Jun. 2015.

[108] C.-X. Wang *et al.*, "Artificial Intelligence Enabled Wireless Networking for 5G and Beyond: Recent Advances and Future Challenges," *IEEE Wireless Communications*, vol. 27, no. 1, pp. 16–23, Mar. 2020.

[109] Z. Qin, H. Ye, G. Y. Li, and B.-H. F. Juang, "Deep Learning in Physical Layer Communications," *IEEE Wireless Communications*, vol. 26, no. 2, pp. 93–99, Mar. 2019.

[110] H. He *et al.*, "Model-Driven Deep Learning for Physical Layer Communications," *IEEE Wireless Communications*, vol. 26, no. 5, pp. 77–83, May 2019.

[111] P. Sabeti *et al.*, "Blind Channel Estimation for Massive MIMO: A Deep Learning Assisted Approach," *arXiv preprint arXiv:2002.10292*, Feb. 2020.

[112] D. Moltchanov, "Distance Distributions in Random Networks," *Ad Hoc Networks*, vol. 10, no. 6, pp. 1146–1166, Aug. 2012.